LOW TEMPERATURE IRRADIATION OF IRON, ZIRCONIUM AND COPPER BY 10 to 16 MeV PROTONS

By

ALI MOHAMED OMAR, M.Sc.M.E.

A Thesis

Submitted to the School of Graduate Studies

in Partial Fulfilment of the Requirements

for the Degree

Doctor of Philosophy

McMASTER UNIVERSITY

MAY 1978

LOW TEMPERATURE IRRADIATION OF
IRON, ZIRCONIUM AND COPPER BY
10 to 16 MeV PROTONS

DOCTOR OF PHILOSOPHY (1978)
(Materials Science)

McMASTER UNIVERSITY
Hamilton, Ontario

TITLE: Low Temperature Irradiation of Iron, Zirconium and Copper by 10 to 16 MeV Protons

AUTHOR: Ali Mohamed Omar, M.Sc.M.E., (University of Manitoba)

SUPERVISOR; Dr. J. E. Robinson

NUMBER OF PAGES: xix, 124

ABSTRACT

Scattering and radiation damage parameters are analytically evaluated for 14 MeV neutrons and 10-17 MeV protons on Fe, Ni, Cu, Zr, Nb and Au. Damage energies are computed for the interactions using both elastic and non-elastic data. The theoretical results show that proton encounters deposit a damage-energy greater by a factor of two than that calculated for mono-energetic 14-MeV neutron events

To examine the theoretical results, electrical resistivity measurements are undertaken for Fe, Zr and Cu irradiated at 12 to 17.5K with 10 to 16 MeV protons. The resistivity change is measured as a function of dose. In addition, post-irradiation isochronal annealing is carried out in-situ using a closed-cycle helium-cooled cryostat.

Values of the resistivity damage rate are determined from the experimental plots of $\Delta\rho_i$ versus ϕt, and compared with the values of $d\Delta\rho_i/d\phi t$ estimated from the theoretical damage-energy results. Also, the observed stage-I recovery is analysed in terms of the corresponding recovery reported for electron and fast-neutron irradiations. The data analysis also includes a discussion of the relation between the present 16-MeV proton data and published data estimated from a fusion-reactor spectrum.

The results presented in this thesis indicate that 16 MeV protons approximate the anticipated damage due to a fusion-reactor spectrum. It is also shown that protons create a damage structure similar to a superposition of the damage structures generated by electrons and fast-neutrons. The sample state of imperfection is shown to influence the induced damage-state in proton irradiation.

ACKNOWLEDGEMENTS

I would like to express my gratitude to Dr. J. E. Robinson for his advice and kind encouragement, without which this work would not have been possible. I am also grateful to Dr. D. A. Thompson (in Engineering Physics Department), Dr. G. R. Piercy, Dr. R. Kelly and all other staff members and fellow graduate students (in the Department of Metallurgy and Materials Science and the Institute for Materials Research) whose discussions have been helpful.

The assistance given by Dr. S. M. Grimes in gathering nuclear data for non-elastic scattering, and a number of discussions with Dr. C. M. Logan (both at Lawrence Livermore Laboratory, California) are acknowledged. Also, I wish to thank Dr. R. R. Coltman, Jr. (at Oak Ridge National Laboratory, Tennessee) for supplying the copper specimens.

I also would like to thank the staff of the Tandem Accelerator Laboratory at McMaster University for their excellent technical assistance. In addition, the help of Mr. A. Arneja during the course of the experimental part is much appreciated.

This work is supported by a contract from the Atomic Energy of Canada Limited and a grant from the National Research Council of Canada to Dr. J. E. Robinson. I thank the National

Research Council of Canada for the Post-graduate Scholarship (1974-77) and McMaster University for the Teaching Assistantship.

The excellent typing job of Mrs. Helen Kennelly is deeply acknowledged.

Finally, I would like to present this work to my wife, Mona, for her patience and constant support.

TABLE OF CONTENTS

PAGE

LIST OF FIGURES

LIST OF TABLES

LIST OF SYMBOLS

English Symbols

a	intercept value, eq. 6.1
A	effective scattering cross-section, Eq. 3.2
A_o	pre-exponential coefficient
A_2	target atomic mass number
b	slope value, Eq. 6.1
c	defect concentration
E	energy of ejected particle in a collision
E_o	incident particle energy
E_d	displacement threshold energy
E_i	ionization threshold energy
E_L	Lindhard parameter, Eq. 2.17
E_m	migration energy for a defect
E^r	recoil energy
E_D^r	recoil damage energy
E_{max}^r	maximum recoil energy
E_{min}^r	minimum recoil energy
e	electronic charge
F	pre-equilibrium emission factor
F(c)	defect-concentration function
$g(\varepsilon)$	function for the reduced energy
k	Boltzmann's constant
k_L	Lindhard parameter, Eq. 2.16

m_1	projectile mass
m_2	target-atom mass
m_e	electron mass
N_d	number of displaced atoms per incident projectile
n	experimentally-determined number, Eq.2.11
n_e	number of electrons per atom
T	absolute temperature
T_m	melting temperature
T_n	nuclear temperature
t	time
U	residual energy = E_o-E
V_c	velocity of centre-of-mass
v	velocity of the ejected particle after collision
v_o	incident particle velocity
v_c	centre-of-mass velocity
v_e	electron velocity at the top of Fermi level
v_r	vacancy recombination volume
v^r	velocity of recoil atom
v^r_{max}	maximum recoil velocity
Z	atomic number

Other Symbols

I,II,III IV,V	recovery stages
α	non-elastic equilibrium-contribution function
$\alpha(v_r)$	approximately equals to $2E_d/\kappa$, Eq. 2.20
β	non-elastic pre-equilibrium-contribution function
$\beta(v_r)$	coefficient accounts for vacancy recombination
γ	kinetic order
γ	mass factor, Eq. 2.4
Δ	infinitesimal change
ε	reduced energy = E^r/E_L
ζ	coefficient = 10 keV^{-1}, Eq. 2.21
η	E_n/T_n , Eq. 2.12
η_D	damage efficiency
ξ	E/E_o, Eq. 2.8
θ	scattering angle in LAB-system
κ	displacement efficiency
ρ_o	resistivity due to imperfection
ρ_{iT}	intrinsic resistivity
ρ_{mT}	resistivity due to magnetic disorder
ρ_{RT}	resistivity at room-temperature
σ	microscopic cross-section
$\sigma_D(E^r)$	damage cross-section, Eq. 4.2
ϕ	scattering angle in COM-system
Ω	solid [illegible]

Superscripts

r	recoil atom

Subscripts

o	incident
1	projectile
2	target
b	backward
c	corrected
D	damage
d	displacement
e	electronic
el	elastic
f	forward
FP	Frenkel pair
i	irradiation
L	Lindhard's
m	migration
max	maximum
min	minimum

n	nuclear
ne	non-elastic
R	reaction
r	recombination
r	reference
T	temperature dependent
A,B,C D,E,F	recovery substage labels

Abbreviations

COM	centre-of-mass
DSCS	differential scattering cross-section
FP	Frenkel pair
LAB	laboratory
PKA	primary knock-on atom
RR	resistivity ratio
RT	room temperature
RTNS	rotating target neutron source
SKA	secondary knock-on atom
V-I	vacancy-interstitial pair

CHAPTER 1

INTRODUCTION

The rapid development of the field of nuclear energy led to considerable interest in the study of radiation-damage effects in materials[1-4]. Of particular interest in the present study are the structural components in proposed fusion devices[5]. For example, the "first-wall" in such devices is subjected to 14.1 MeV neutrons at a flux of 10^{21}-10^{22} n cm^{-2} per year[6]. The first wall is also exposed to a spectrum of less energetic particles as well as x-rays[7]. Available laboratory sources provide neutron fluxes two orders of magnitude lower than the anticipated flux in a fusion reactor[8]. Therefore, to investigate the damage effects in fusion-reactor materials simulation techniques have been introduced.

Fission neutrons have been employed to study the displacement effects created by 14 MeV neutron irradiation. In such approaches, a parameter called "damage effectiveness" was introduced[9]. This parameter expresses the damage induced by fusion neutrons in terms of the damage created by a fission-neutron spectrum. Its value varies between 2 and 7 for most metals[9,10]. This approach is impractical since fission-neutrons neither simulate the primary recoil spectra nor the transmutation interactions anticipated in a fusion device.

In a limited number of applications[11,12], heavy- and self-ion bombardments have been used to simulate fast neutron damage in reactor materials. The limited depth of penetration precluded the use of such techniques to study the bulk damage of the target elements.

Prediction of the damage cascades has successfully been made using computers[13,112]. This approach is very useful in exploring the state of the induced damage, and in determining some lattice parameters[14]. The drawback of this approach, besides the high cost of computation time, is its dependence on theoretical modeling. This implies several approximations to what is expected to be observed by experiments.

Proton simulation, which is the subject of the present thesis, was introduced by Logan and his collaborators[15,16] to approximate the displacement effects in niobium when subjected to 14.0 MeV neutron bombardment. Their treatment of the problem showed that the primary recoils created by 14 MeV neutrons can closely be approximated by 14-16 MeV proton scattering. Experimental verification of such a hypothesis has been undertaken by Mitchell et al.[17] They used a high voltage electron microscope to investigate the cluster densities created in two copper samples separately irradiated at room temperature by 14 MeV neutrons and 16 MeV protons. Their micrographs, where visible clusters were examined, showed that proton bombardment produced similar defect clusters as did 14.0 MeV neutrons. Subsequent to this theoretical and experimental work, a number of researchers have used the proton simulation technique to study surface[18-21] and bulk[22] damage effects.

The aim of the present work is to test the validity, and to determine the limitations, of using high energy protons to simulate fusion-reactor damage effects. Scattering and radiation damage parameters are numerically evaluated for six elements of interest, namely Fe, Ni, Cu, Zr, Nb and Au. For this part of the study, neutrons at 14 MeV and protons with energies between 10 and 17 MeV are employed as incident particles. To justify the results of the theoretical part, electrical resistivity measurements are undertaken for Fe, Zr and Cu irradiated at 12 to 17.5 K with 10 to 16 MeV protons.

A general background on the primary and secondary collision events is presented in Chapter 2. Chapter 3 includes a presentation of several techniques normally used for the detection of simple defects and defect-clusters. It also contains a survey of the methods normally adopted to interpret the recovery schemes of simple and complex states of radiation damage. The theoretical treatment of the problem is found in Chapter 4 while Chapters 5 through 7 deal with the experimental method and results. Sample preparation, irradiation facilities and measurement resolution are presented in Chapter 5. The experimental results are displayed and discussed in

Chapter 6 (resistivity-dose measurements) and in Chapter 7 (anneal measurements). A summary of the theoretical and experimental results is included in Chapter 8. Conclusions are reported in Chapter 9.

CHAPTER 2

RADIATION DAMAGE

Radiation damage may be defined as the disorder induced in materials when exposed to reactor environment. Under such conditions, photons, slow-moving or energetic particles collide with the structural components and lose part of their energy in atomic displacement events. During these primary encounters, the target atoms may be dislodged from their normal lattice sites. Such displaced atoms will be termed primary knock-on atoms, PKA's. The damage may then propagate if a PKA has sufficient energy to cause more displacements.

Several models for the collision between the projectile and target atoms are discussed in section 2.1. The governing equations for these models are presented as well. Section 2.2 will include a detailed presentation of several models used to estimate the number of displaced atoms for each incident particle.

2.1 Primary Collision Events

In the energy range of interest (10-17 MeV), the interaction between an incident particle and a target nucleus may adequately be described by a binary collision model[23]. The mean-free path for neutrons or protons undergoing nuclear scattering in such cases is a few tens of centimeters. The scattering events are produced relatively uniformly within the bulk of the target. Neutrons interact directly with target nuclei without losing energy in penetrating the electron cloud surrounding them. On the contrary, coulomb interactions with electrons consume part of the incident protons energy before they interact with target nuclei. Thus, protons with energies higher than 14.0 MeV must be used if fusion reactor neutrons are to be simulated.

Two modes of collision take place in a projectile-nucleus encounter; these are elastic and non-elastic scattering. Each scattering mode will be described in detail in the following two subsections.

2.1.1 Elastic collisions

Elastic collisions are those events wherein the kinetic energy is conserved[24]. In a laboratory system of co-ordinates (LAB-system), an incident particle having energy E_0, velocity v_0 and mass m_1 will collide with a target atom of mass m_2 at rest. After collision, the projectile particle will be scattered at an angle θ to its incident direction with a velocity v. At the same time, the target nucleus will recoil with an energy E^r. Evaluation of E^r as a function of E_0, θ, m_1 and m_2 is mathematically complicated if one uses the LAB-system. Instead, a centre-of-mass system of coordinates (COM-system) may be introduced as displayed in Fig. 2.1. Here, the centre-of-mass for the projectile and target nucleus is assumed to be at rest, and both approach it with the velocities indicated

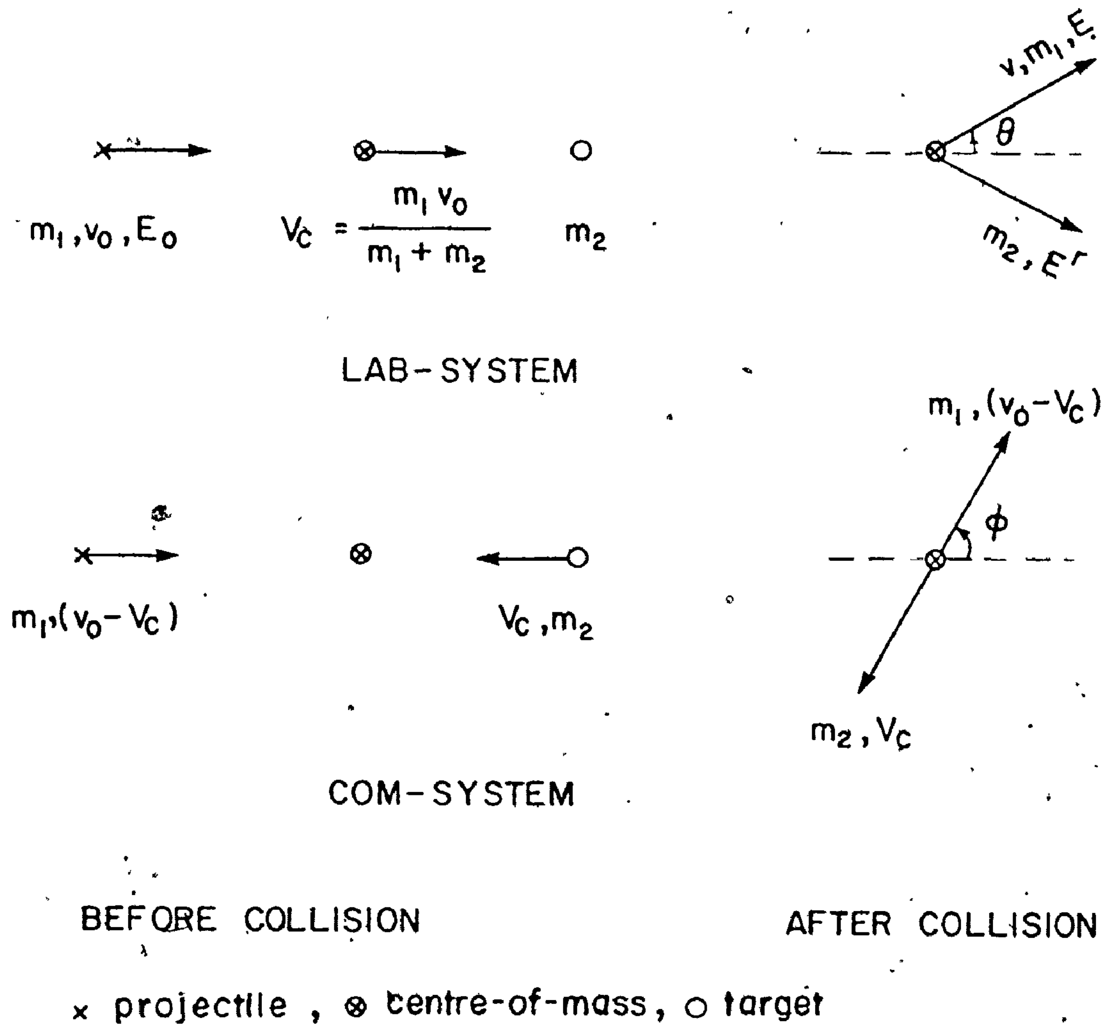

Fig. 2.1: Elastic scattering in LAB- and COM-systems.

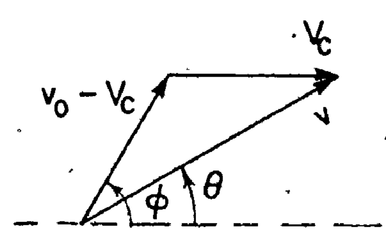

Fig. 2.2: Vector diagram for the projectile velocities after collision in LAB- and COM-systems.

in Fig. 2.1. After collision, the conservation laws of energy and momentum lead to the same magnitude of velocities of the colliding species. These velocities will only change their directions. The scattered particle will move at an angle ϕ, while the recoiled nucleus will move off at an angle $180+\phi$ with the incident direction.

After collision, the scattered-particle velocity v can be expressed as a function of ϕ by applying the trigonometric law of cosines to Fig. 2.2. This yields

$$v^2 = v_0^2(m_1^2 + m_2^2 + 2m_1m_2 \cos \phi)/(m_1 + m_2)^2 . \quad 2.1$$

The recoil-particle energy E^r after collision is then

$$E^r = E_0 - \frac{1}{2} m_1v^2 = 2m_1m_2E_0(1-\cos\phi)/(m_1+m_2)^2 . \quad 2.2$$

Eq. 2.2 may be rewritten as

$$E^r = \gamma E_0 \sin^2(\phi/2) , \quad 2.3$$

where

$$\gamma = 4m_1m_2/(m_1+m_2)^2 . \quad 2.4$$

The maximum energy transferred to a recoil nucleus, E^r_{max}, results from a head-on collision, i.e. $\phi = 180°$. In such a case, E^r_{max} may be expressed as

$$E^r_{max} = \gamma E_0 = 4m_1m_2E_0/(m_1+m_2)^2 . \quad 2.5$$

The elastic scattering process is not always isotropic. Reported data[25,115] show anisotropy for neutron incident energies greater than 2.0 MeV. Forward scattering is pronounced in the case of proton elastic encounters because of Rutherford scattering events[26]. Elastic collisions can be described by the differential elastic cross section $(DSCS)_{el} \equiv (d\sigma/d\Omega)_{el}$. Such a parameter gives the probability of finding a PKA in a range of scattering solid angles between Ω and $\Omega + \Delta\Omega$. Values for the $(DSCS)_{el}$ are often determined by experiments. However, due to practical limitations, the experimental data only covers a range of scattering angles between 15° and 165°[27]. To circumvent this difficulty, optical-model[27] parameters are often fitted to the experimental data, and then extrapolated to give estimates for $(DSCS)_{el}$ below 15° and above 165°. Information about neutron scattering is well covered for energies below 15 MeV[28]. The corresponding data for proton encounters are scarce[29] in the energy range of interest (10-17 MeV).

It is the practice to use a differential scattering cross section based on the recoil energy, namely $(d\sigma/dE^r)_{el}$, to evaluate the scattering and damage parameters[15]. It may be related to $(d\sigma/d\Omega)_{el}$ by differentiating Eq. 2.3 with respect to ϕ and by knowing that $d\Omega$ is equal to $2\pi \sin\phi d\phi$ and then substitute in the equation

$$(d\sigma/dE^r)_{el} = \left(\frac{d\sigma}{d\Omega}\right)_{el} \cdot \frac{d\Omega}{d\phi} \cdot \frac{d\phi}{dE^r} \quad . \qquad 2.6$$

The final form for $(d\sigma/dE^r)_{el}$ will be

$$(d\sigma/dE^r)_{el} = 4\pi \cdot (d\sigma/d\Omega)_{el}/\gamma E_0 \quad 2.7$$

Since $(d\sigma/d\Omega)_{el}$ is usually determined as a function of ϕ, from Eqs. 2.7 and 2.3, $(d\sigma/dE^r)_{el}$ can be displayed either as a function of ϕ or as a function of the PKA energy E^r. The latter presentation is more useful than the former since it gives the "PKA spectrum". In Chapter 4 we will use, in part, such an elastic PKA spectrum to generate a number of radiation damage and scattering parameters.

2.1.2 Non-elastic collisions

Non-elastic collisions include several modes of interaction such as inelastic, capture and transmutation. As in the case of elastic scattering, non-elastic events can also be described by the corresponding differential scattering cross sections, i.e. $(d\sigma/d\Omega)_{ne}$. Values for $(d\sigma/d\Omega)_{ne}$ can be estimated by theoretical approaches based on models for nuclear interactions[30,31]. For incident energies below 10 MeV an evaporation model can be applied[9,30]. A "pre-equilibrium" term must be added for projectile energies greater than 10 MeV[30,31].

An incident particle with energy E_0 will collide with the target nucleus which is at rest. The two particles will form a compound nucleus. Such a compound nucleus will move with a velocity v_c, in the LAB-system equal to $\frac{1}{2} v^r_{max}$ where $v^r_{max} = (2E^r_{max}/m_2)^{1/2}$.

The moving compound nucleus then ejects a particle of mass m_1 and energy E at an angle ϕ with the incident direction in the COM-system. The remaining nucleus will normally be left in an excited state and, in addition, will gain a kinetic energy E^r. It is probable that the residual nucleus will eject a particle(s) before reaching the equilibrium ground-state. This is the case wherein a pre-equilibrium emission takes place.

The PKA resulting from a non-elastic encounter may gain a velocity smaller or larger than v_c. This depends on the energy of the ejected particle[15]. The resulting kinetic energy of the recoil atom can be expressed as

$$E^r = \frac{1}{4} E^r_{max}[1-\xi-2\xi^{1/2}\cos\phi] \qquad 2.8$$

where $\xi = E/E_0$. The time between the formation of the composite and the ejection of the particle(s) is very small in comparison with the time required to travel between two lattice sites[16]. Consequently, it is possible to assume that both the collision event and the recoil emission take place at the same lattice site. At $\phi = 0°$, Eq. 2.8 gives the minimum transferred energy, for forward scattering, as

$$E^r_f = \frac{1}{4} E^r_{max}[1-\xi-2\xi^{1/2}] \ . \qquad 2.9$$

Maximum energy transfer occurs by non-elastic back scattering. In such a case, $\phi = 180°$ and Eq. 2.8 yields

$$E^r_b = \frac{1}{4} E^r_{max}[1-\xi+2\xi^{1/2}] \ . \qquad 2.10$$

For each value of the ejected-particle E, the probability of finding recoils with energies between E_f^r and E_b^r is the same, i.e. the collision event is isotropic[30]. Events other than inelastic, such as gamma, alpha or second particle emission may influence the isotropy of the scattering encounter. Also, pre-equilibrium emission is not perfectly isotropic. The effect of these on the recoil spectra is negligible[15].

To estimate values for $(d\sigma/dE^r)_{ne}$, a model described by Grimes and his coworkers[30,33] will be used. This model accounts for all neutron and proton non-elastic events that emit a proton or a neutron. It also accounts for the first proton or neutron in reactions like (n,nx) or (p,px). The effect of emitting a second particle or a heavier particle on the final result is insignificant[16,22] (see the Appendix).

The differential scatting cross section for non-elastic encounters, integrated over all the scattering angles, can be evaluated for each ejected-particle energy E from the equation,

$$(d\sigma/dE^r)_{ne} = (d\sigma/dE)_{ne} = E\,\alpha\,\exp(U/T_n) + E\beta U^n \qquad 2.11$$

where U is the residual energy and is equal to E_0-E, T_n is the nuclear temperature and n is a number determined by experiments. The first term on the right hand side of Eq. 2.11 is derived from the evaporation model. It describes the particle emission after the composite nucleus reaches its ground state. The last term presents a semi-empirical form for the pre-equilibrium emission contribution. The coefficients α and β are functions of m_1, E_0, T_n and a pre-equilibrium emission factor F. The analytical forms of α and β may respectively be written as[15]

$$\alpha = \frac{(1-F)\sigma_R}{T_n^2[\exp(\eta)-\eta-1]} \qquad 2.12$$

and

$$\beta = F\sigma_R(n+1)(n+2)/E_o^{n+2} \qquad 2.13$$

where $\eta = E_0/T_n$ and σ_R presents a reaction cross section. Values of n, F, T_n and σ_R are determined from experiments[30,33,34].

The non-elastic PKA spectra can be obtained by using Eq. 2.11 to yield values for $(d\sigma/dE^r)_{ne}$ which correspond to PKA energies between the two extreme values of Eqs. 2.9 and 2.10. Such calculations will be presented in Chapter 4.

2.2 Secondary Collision Events: Displacement Cascades

As has been mentioned in section 2.1, an incident energetic-particle will undergo only one nuclear collision with a target sample of dimensions used in the present work (see section 5.1). The result of this single scattering is a PKA. The PKA may be dislodged from its lattice site if it receives during scattering an energy greater than a certain threshold value E_d. If the energy received is less than E_d, the PKA will experience a thermal perturbation. A moving PKA with energy $E^r > E_d$ may collide with another nearby lattice atom. Several collision sequences may take place afterwards and the resulting damage state depends on the energy of the PKA as well as on the recoiling direction[13,14].

The simplest damage configuration which may result after irradiation is a Frenkel pair. This takes place whenever a PKA does not receive enough energy to cause more displacements. In such cases, the PKA will occupy one of the nearby interstitial sites. The vacant site left behind, now a vacancy, and the interstitial form a Frenkel pair. In some cases, the interstitial recombines with the vacancy even at very low temperatures[35]. If the interstitial escapes a "vacancy-recombination volume", it will form a stable Frenkel pair. Recombination in this case has to be thermally activated . A Frenkel pair may also be produced in a glancing collision between the energetic incident particle and the target nucleus. This case dominates the proton elastic scattering as will be seen in Chapter 4. The distance between the two point defects in a Frenkel pair depends on the recoiling direction. The motion of the recoiled atom may be "focused" along a line of close-packed atoms[36] providing that the angle of motion with respect to the close-packed direction is maintained below a certain value. The result is a distant vacancy-interstitial (V-I) pair. In a "dynamic crowdion"[36] mechanism, momentum and energy are transferred by replacement. In a channeling[37,38,39] mechanism, energy is lost to the electrons of the atoms that surround a "channel" within the target. These mechanisms for long-range movement also yield distant V-I pairs. It is worth mentioning here that any thermal disturbance is able to scatter the long-range energy transfer and then displacements may take place.

If the PKA moves with high energy after the primary collision, it will transfer enough energy to a secondary recoil (SKA). Both may move with energies high enough to generate a chain of SKA's. Such an effect is called a "damage cascade". A cascade is produced by one PKA. The displacement process will stop when the SKA's at the end of the cascade-branches reach energies below $2E_d$. A cascade created by a PKA of low energy may be contained in one region. More energetic PKA's produce cascades consisting of several distinct damage regions[40]. Such damage regions are called subcascades. The damage state of a subcascade is complex. Defect configurations ranging from point defects to dislocation loops may constitute the bulk of a subcascade[41]. The situation becomes more complicated if the energy deposition per atomic volume exceeds the melting energy kT_m of the target material. This takes place in what are known as "displacement spikes" or "thermal spikes". A displacement spike is a melted region resulting from an energy deposition in a very short length of track. It lasts for $\sim$ 100 atomic vibrations for a typical metal that melts at 1000 K[42]. Such a melted region may recrystallize in the same order as its undisturbed surroundings[43] or it may cool down leaving a vacancy-rich core surrounded by an interstitial-rich zone[36,44]. In the case of a multiple collision, wherein an energy less than E_d is received simultaneously by a few atoms, a fully disordered zone may result. Such an effect leads to a thermal spike[42,45].

A fraction of the PKA and SKA energy is consumed in electronic interaction. Ionization and excitation of the lattice atoms due to moving ions have been studied thoroughly in the past two decades[46]. An early model suggested the use of an energy $E_i \simeq A_2$ keV as an ionization threshold energy[47]. Above E_i, the moving atom will lose all its energy to electronic encounters. Below E_i, the moving ion will dissipate all its energy in displacement events. At the beginning of the 1960's, Lindhard and his collaborators[48] proposed a universal formalism for electronic losses. This will be referred to as LSS theory. In such a theory, the loss of energy to electrons per unit path-length is proportional to the velocity of the movion ion. Subsequent treatment of the problem led to a formula for the fraction of energy lost in electronic encounters. The rest of the ion energy may therefore be dissipated in producing displacements. The concept of the damage efficiency η_D is thus introduced[9]. This is the fraction of the primary recoil energy lost in creating atomic displacements. It is defined as

$$\eta_D = [1 + k_L g(\varepsilon)]^{-1} . \qquad 2.14$$

The function $g(\varepsilon)$ takes the form[9]

$$g(\varepsilon) = 3.4008(\varepsilon)^{1/6} + 0.40244(\varepsilon)^{3/4} + \varepsilon \qquad 2.15$$

where $\varepsilon = E^r/E_L$. The Lindhard parameters k_L and E_L are defined respectively as

$$k_L = 0.133745\ Z^{2/3}/A_2^{1/2} \qquad 2.16$$

and

$$E_L = 86.931\ Z^{7/3}\ \mathrm{eV} \qquad 2.17$$

where Z is the atomic number whose mass is A_2.

The number of displaced atoms in a cascade, N_d, is an important parameter in radiation damage study. Several models have been introduced to estimate N_d. Kinchin and Pease[49] proposed a model in which they defined two parameters: an energy threshold E_d, and an ionization cut-off energy E_i. They suggested that a primary recoil with an energy E^r less than E_d will cause no displacement. If $E_d < E^r < 2E_d$, one displacement will take place. For a PKA having an energy greater than $2E_d$, and less than E_i, it will produce a total number of displacements $N_d \approx E^r/2E_d$. If the PKA energy exceeds E_i, all the energy above E_i will be lost to electronic excitation and ionization. A modified model[50,51] has been introduced to account for replacement effects and to adopt the LSS model for electronic losses. The modified formula is

$$N_d = \frac{\kappa E_D^r}{2E_d}\ ,\ E_D^r > 2E_d/\kappa \qquad 2.18$$

where κ is the "displacement efficiency" and E_D^r is the part of the recoil energy which is dissipated in atomic displacement, i.e.

$$E_D^r = E^r \cdot \eta_D \; . \qquad 2.19$$

The value of κ has been found analytically[50] and through computer simulation[51] to be equal to 0.80. Eq. 2.18 usually overestimates the number of displaced atoms per PKA when compared with experimental observations[52]. As a result, a recombination model is proposed for cascade calculations in the binary collision approximation[51,53]. In such a model, permanent displacement of a lattice atom can only be achieved if the dislodged atom escapes a recombination volume, v_r, surrounding the vacancy left behind. According to this model, recombination of displaced atoms is possible even at very low temperatures[35]. One of the forms used to estimate N_d using this model is[51]

$$N_d = \frac{E_D^r}{\alpha(v_r) + \beta(v_r)E_D^r} \; , \qquad 2.20$$

The value of $\alpha(v_r)$ is approximately equal to $2E_d/\kappa$. The term $\beta(v_r)E_D^r$ represents the probability of recombination. It is a function of the recombination volume v_r, and is directly proportional to the recoil damage energy E_D^r. Therefore, for recoils moving with low energies Eqs. 2.18 and 2.20 yield comparable results. At high recoil energies, Eq. 2.20 gives more close results to the experimental estimates than Eq. 2.18 does[51]. For iron, the above displacement models have been used to give a "standard formula" in the form[54]

$$N_d = \zeta E_D^r \qquad 2.21$$

where $\zeta = 10\ keV^{-1}$. Eq. 2.21 has been used successfully to estimate the number of atomic displacements produced during both fission-neutron and ion irradiation of iron[55,56].

CHAPTER 3

DETECTION AND RECOVERY OF DEFECTS IN SOLIDS

In this chapter, resistivity change with defect concentration will be discussed in detail. Other detection techniques will briefly be presented for the completion of the subject. Mechanisms for defect recovery will then be presented.

3.1 Detection of Simple Defects

Each of the following techniques is related to a particular physical property of the irradiated target. The change in such a physical property can then be related to the structure and to the nature of the damage created in the test specimen.

3.1.1 Dilation and lattice parameter changes

An interstitial, or a vacancy, creates a local stress field around it. The surrounding atoms undergo a relaxation process in which they move away from or towards the point defect. The resulting lattice-parameter change, and the variation in the macroscopic length of the sample are correlated to the defect density induced during irradiation[57].

3.1.2 Internal friction

This technique is more selective, since only asymmetric defects can give rise to an internal friction peak. Internal friction deals with the energy absorbed due to the reorientation of point defects under mechanical vibration[58]. Analysis of the observed peaks may lead to the estimation of defect concentration and activation energies, and to the understanding of the damage state induced[59,60].

3.1.3 Magnetic properties

In ferromagnetic metals, magnetic properties are affected by clusters of the same size as the width of Bloch wall (5-200 nm)[58]. Point defects may also affect the motion of a Bloch wall leading to a magnetic aftereffect. In such a case a time decrease of the initial permeability is observed immediately after a demagnetization. Activation energy of migration and concentration of asymmetric defects can be determined[61] from such data.

3.1.4 Resistivity-change measurements

This approach will be discussed in detail since it is used throughout the experimental part of this thesis.

The measured resistivity (ρ_T) of a metal can be expressed, according to Matthiessen's rule, in terms of temperature-dependent (ρ_{iT}, ρ_{mT}) and temperature-independent (ρ_o) contributions. This takes the form

$$\rho_T = \rho_0 + \rho_{iT} + \rho_{mT} \quad (3.1)$$

The quantity ρ_o arises from the presence of impurities, defects and strain in the metal lattice. It is conventional to quote the ratio ρ_{RT}/ρ_o to provide an indication of the specimen's state of purity and perfection. Such a ratio is called the "resistivity ratio" (RR). The quantity ρ_{iT} is the intrinsic resistivity of metals. It is due to the interaction of the conduction electrons with phonons during their motion in the lattice. The parameter ρ_{mT} represents a magnetic disorder term. It is due to electron scattering from disordered spin arrangements in ferromagnetic metals. The magnetic disorder term ρ_{mT} is temperature dependent below the Curie temperature of the metal under consideration[62].

Deviation from Matthiessen's rule may be observed. It is attributed to the influence of pressure, magnetic fields and the size of the specimen[63]. Anisotropy of resistivity is a common feature in cold worked samples. However, experimental results of cold-worked strips of metals showed that this effect is so insignificant[64] that it may be neglected here.

It is essential to keep ρ_{RT}/ρ_o as high as possible in order to achieve high sensitivity in measuring the resistivity change due to defect generation, or due to defect annihilation. High purity samples have then to be used. Also, operational conditions are favorable under 20 K for most metals irradiated by high energy particles.

The effect of the change in defect concentration on the residual resistivity is given by[65]

$$\Delta\rho_o = \frac{m_e v_e A\ \Delta c}{n_e e^2} \qquad 3.2$$

where m_e and e are the electronic effective mass and charge respectively, v_e is the electron's velocity at the top of the Fermi distribution, A represents an effective scattering area, Δc is the atomic fraction of defects and n_e is the number of free electrons per atom. The increase in the residual resistivity is therefore proportional to the increase in defect concentration.

Theoretical calculations[64] show that the increase in resistivity due to an isolated vacancy and an interstitial are comparable. The resistivity due to a vacancy cluster has similarly been calculated[66]. The results showed that the di-vacancy contribution did not differ from that of two isolated vacancies.

It is an accepted practice to measure the resistivity change due to the creation, or the disappearance of a V-I pair (Frenkel pair), $\Delta\rho_{FP}$, in ohms/at.%. Electron irradiation experiments are usually used to determine $\Delta\rho_{FP}$.[67]

3.2 Recovery of Simple Defects

Recovery of a particular type of defect is assumed to occur by a single activated process with a constant activation energy. If the number of defects per unit volume is c, its annealing rate can then be written as[68]

$$dc/dt = -A_o F(c) e^{-E_m/kT} \qquad 3.3$$

where F(c) is any continuous function of c, E_m represents the defect migration energy, A_o is a factor which is temperature independent, T is the absolute annealing temperature and k is Boltzmann's constant. The exponential dependence of the defect mobility on the ratio E_m/kT is such that at very low temperature all such defects will be essentially immobile.

The order of the kinetics of the recovery process can be expressed by a chemical rate equation, i.e.

$$dc/dt = -A_o \; c^{\gamma} \; e^{-E_m/kT} \qquad 3.4$$

where γ is the order of the activated process. Eqs. 3.3 and 3.4 are expressing the same process with the function c^{γ} replacing F(c). Diffusion of defects to a fixed infinite sink corresponds to a first-order reaction, $\gamma=1$, while random annihilation of equal concentration of defects is described by a second order equation, $\gamma=2$.

Values for interstitial and vacancy migration energies can be determined theoretically[69] or they can be determined by experiments[70]. Typical values for E_m in most metals are $\sim$ 0.1 eV or less for interstitials and between 0.6 to 2.0 eV for vacancies. Migration energies for di-interstitials are greater than for a single interstitials, while di-vacancies migrate with energies less than those of single vacancies, but greater than those of di-interstitials[69,70]. Therefore, the early recovery stages of defects are likely to be governed by migration of interstitials.

Recovery of point defects may take place according to the following mechanisms[71]:

1) Annihilation of close Frenkel pairs: This process usually requires low thermal activation. Interstitials experience a few jumps before reaching their sinks. It is a first-order activated process.

2) Long-range migration: In such a process, interstitials may initially migrate to vacancy sites. It is a first-order reaction. More thermal energy is needed to complete the annihilation in this case than the corresponding energy required for the recovery of Frenkel-pairs.

3) Random migration: This reaction depends on the concentration of the annihilation sinks. Here, interstitials may migrate randomly to sinks such as dislocations, impurity atoms or surface imperfections. It is a first-order process.

4) Aggregation: Interstitial clustering and void formation are important modes of recovery since the large clusters produced during irradiation may attract simple defects[72]. This effect may be enhanced by the irradiation process itself[73-75].

The above mechanisms normally take place in the stage I recovery of most metals. At higher activation energies, i.e. higher annealing temperatures, other mechanisms are anticipated. These include release from impurities and other traps, vacancy migration and large cluster and void formation.

3.3 Defect Clusters

It is thermodynamically favourable for irradiation-induced defects to form clusters rather than simpler defect-configurations[41]. The cluster nuclei may grow by combining with other cluster nuclei, or by attracting simple defects. At a certain size, the growing aggregate becomes metastable and it may collapse to a disc-shaped defect, or more likely to a dislocation loop.

Direct observation of complex defects can be made by using an electron microscope. Yet, only clusters with diameters greater than 18°A can be resolved[123]. Such a difficulty may be overcome either by employing field-ion microscopy or by using 100 and 1000 kV electron microscopes[124]. The resolution in such techniques is of the same order as the atomic size. The interaction of clusters with dislocation lines and the macroscopic distortion that they cause in some crystals presents two other means for indirect observation of clusters.

For most metals, the resistivity of a simple defect is of the order of 10^{-21} μΩ cm. The resistivity of a dislocation line is between 2.0 and 20×10^{-13} μΩ/cm length depending on its direction within the lattice[62]. The resistivity of a vacancy-cluster has been calculated in terms of the resistivity increment per vacancy in the cluster. For aggregate nuclei of small sizes, it was found that their contribution to the resistivity change did not substantially differ from that of the same number of isolated vacancies[66]. As the size of the cluster increases, the contribution per vacancy decreases monotonically as displayed in Fig. 3.1.

Recovery of defect-clusters and dislocations requires a high degree of thermal activation. At high temperatures, dislocations may move towards other dislocations or crystal imperfections. In some cases, they intercept each other causing jogs. The result is immobile dislocations. Complete recovery of clusters and sessile dislocations takes place at temperatures close to the recrystallization temperature[41].

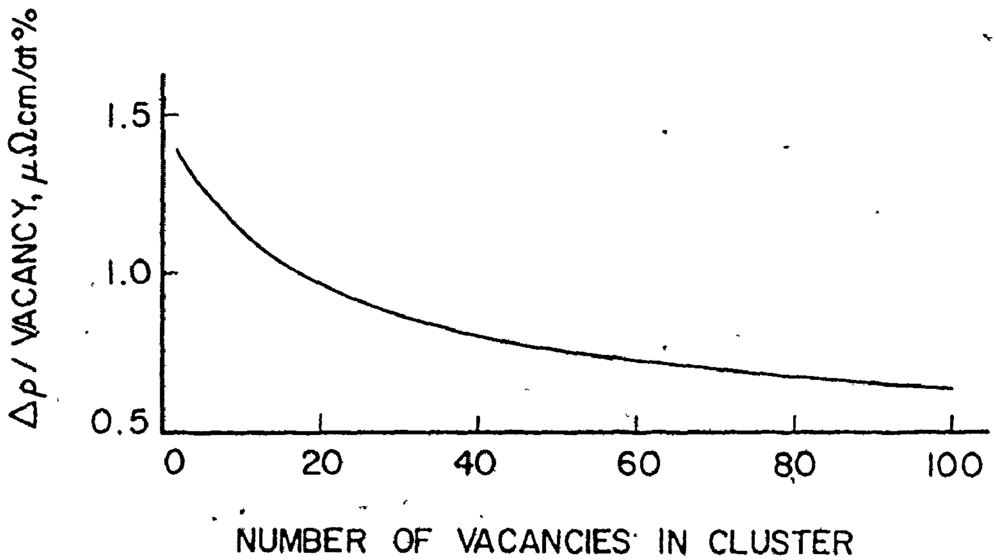

Fig. 3.1: Resistivity change per vacancy as a function of the number of vacancies in a cluster (Ref. 66).

CHAPTER 4

THEORETICAL TREATMENT OF THE PROBLEM: SCATTERING AND RADIATION DAMAGE PARAMETERS

The theoretical treatment of the problem involves three steps[76]: i) determination of the appropriate elastic and non-elastic data, ii) computation of the PKA spectra, and iii) integration of such spectra to determine the damage energies in barn-keV per incident particle.

4.1 Nuclear Data and Calculation Procedure

For the elastic scattering, we relied on previous data obtained by experiments[77-81] and by an optical model fitted to experimental observations[82-89]. Values for neutron scattering near 0°, where data is not available, are calculated using Wick's limit[90]. A summary of the elastic scattering data is presented in Table 4-1. The elastic recoil energy spectra are then calculated using Eqs. 2.3 and 2.7.

Non-elastic differential cross sections are determined using Eq. 2.11. The non-elastic recoil energy is computed from Eq. 2.8 within the two extreme-values of Eqs. 2.9 and 2.10. Values for η, F and T_n are taken from several sources for the targets under consideration[33,34,91-93]. Other values are inferred[94] by considering their dependence on E_o. Values for σ_R are obtained from experimental data for neutrons[88,91,92]

Table 4-1. Target elements studied and sources for elastic scattering data.

Element	Incident particle	E_o (MeV)	Ref.
Nat.*Fe	neutron	14.00	83
^{56}Fe	proton	10.93	77
Nat.Fe	proton	14.30	84
Nat.Fe	proton	17.00	78,84
Nat.Ni	neutron	14.00	85
	proton	9.87	79,86
	proton	14.30	84
	proton	17.00	78,84
Nat.Cu	neutron	14.50	87
	proton	9.75	79,86
	proton	17.00	78,84
Nat.Zr	neutron	14.00	88
^{92}Zr	proton	10.75	89
^{90}Zr	proton	12.70	80
^{90}Zr	proton	16.00	82
Nat.Nb	neutron	14.10	15
	proton	9.37	81
	proton	16.40	15
Nat.Au	neutron	14.00	123
	proton	9.84	79
	proton	17.00	78,84

*Nat. means natural isotopic abundance

and either from theoretical calculations[84,93] or from experimental data[80,82] for protons. The four parameters required for the non-elastic model are found in Table 4-2.

The total differential energy scattering cross sections are calculated by adding the corresponding elastic and non-elastic values at each PKA energy. The damage energy E_D can thus be calculated from the equation,

$$E_D = \int_{E^r_{min}}^{E^r_{max}} \sigma_D(E^r)\,dE^r \quad , \qquad 4.1$$

where E^r_{min} presents a lower limit for integration. The function $\sigma_D(E^r)$ is the damage cross section. It may be expressed as

$$\sigma_D(E^r) = \frac{d\sigma}{dE^r}\Big)_{total} \cdot E^r \cdot \eta_D \; . \qquad 4.2$$

If $\sigma_D(E^r)$ is plotted against E^r, a damage spectrum will result. Integration of such a spectrum, Eq. 4.1, yields the damage energy E_D.

4.2 Results of the Calculations

The calculations are carried out for six elements of interest: Fe, Ni, Cu, Zr, Nb and Au. The total number of PKA's produced per incident particle, namely $(d\sigma/dE^r)_{total}$, is presented against E^r in Figs. 4.1 to 4.6 for each element. As can be seen from such figures, the proton cross-sections are generally

Table 4-2: The four parameters required for inelastic calculations

Element	Reaction	E_o, MeV	n	F	T_n, MeV	σ_R, b	Ref.
Fe	(n,n')	14.00	2	0.15	1.1	1.450±0.02	33,33,33,92
	(p,n)	10.00	2	0.09	1.2	0.840±0.01	94,94,94,93
	(p,n)	14.00	2	0.11	1.2	0.982±0.006	33,33,33,84
	(p,n)	17.00	2	0.12	1.2	1.005±0.002	94,94,94,84
Ni	(n,n')	14.00	2	0.15	0.9	1.400±0.004	33,33,33,88
	(p,n)	10.00	2	0.10	1.0	0.850±0.01	94,94,94,93
	(p,n)	14.30	2	0.12	1.0	0.956±0.015	94,94,94,84
	(p,n)	17.00	2	0.14	1.0	0.979±0.004	94,94,94,84
Cu	(n,n')	14.00	2	0.16	0.9	1.440	33,33,33,91
	(p,n)	10.00	2	0.11	1.0	0.850±0.01	94,94,94,93
	(p,n)	17.00	2	0.15	1.0	1.008±0.005	94,94,94,84
Zr	(n,n')	14.00	2	0.15	0.71±0.04	1.349±0.01	94,33,34,91
	(p,n)	10.00	2	0.08	0.7	0.860±0.01	94,94,94,93
	(p,n)	12.70	2	0.09	0.7	0.964±0.001	94,94,94.80
	(p,n)	16.00	2	0.10	0.7	1.139±0.002	33,33,33,82
Nb	(n,n')	14.00	2	0.15	0.66±0.03	2.00	15,15,34,15
	(p,n)	10.00	2	0.08	0.68	0.931	94,94,94,94
	(p,n)	16.40	2	0.10	0.68	1.100	15,15,15,15
Au	(n,n')	14.00	3	0.08	0.64±0.1	2.420	94,94,123,91
	(p,n)	10.00	3	0.05	0.56	0.730±0.001	94,94,94,93
	(p,n)	17.00	3	0.07	0.56	0.986±0.002	94,94,94,84

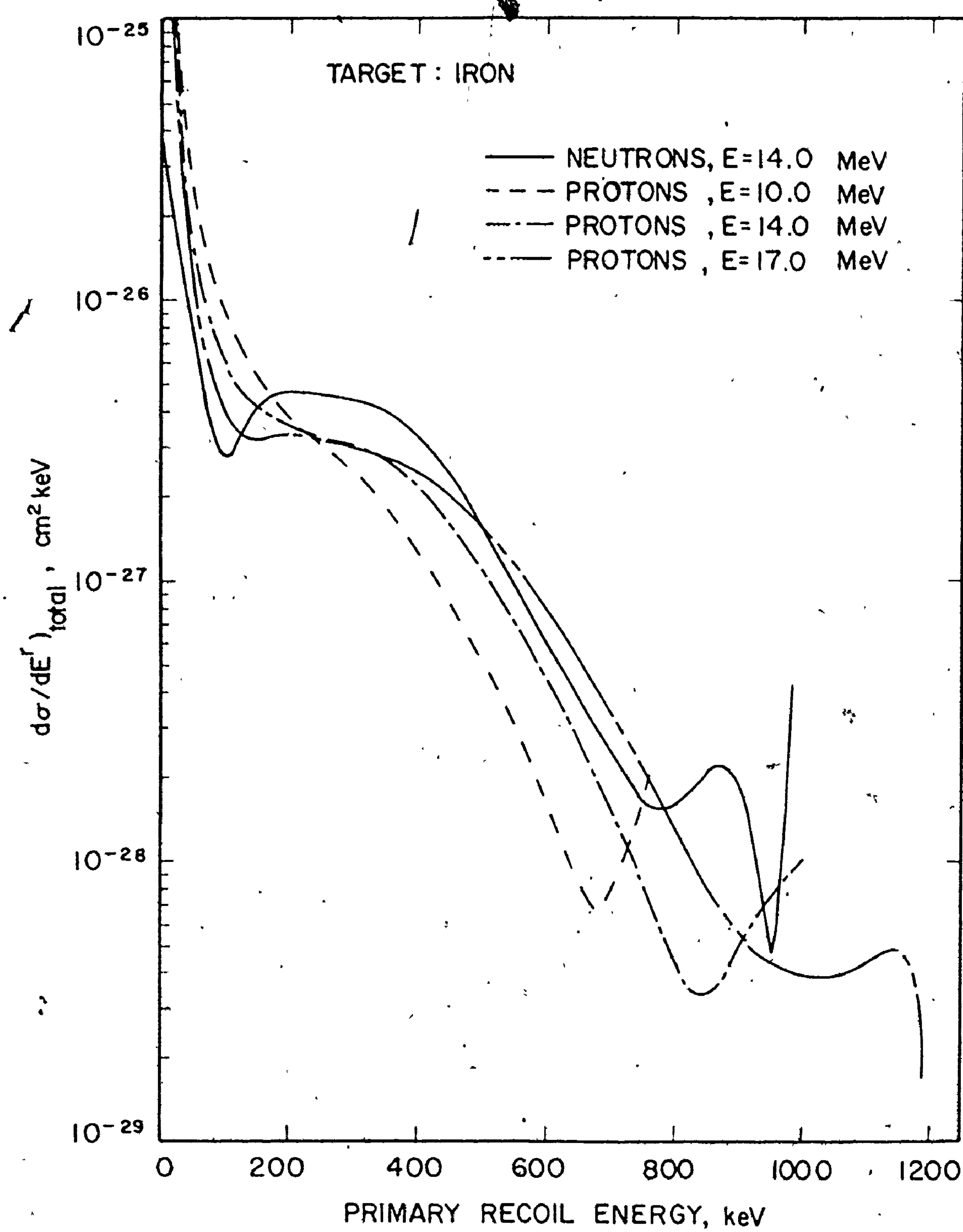

Fig. 4.1: Primary recoil spectra for Fe. Total differential scattering cross-sections, $d\sigma/dE^r)_{total}$, versus the PKA energy E^r.

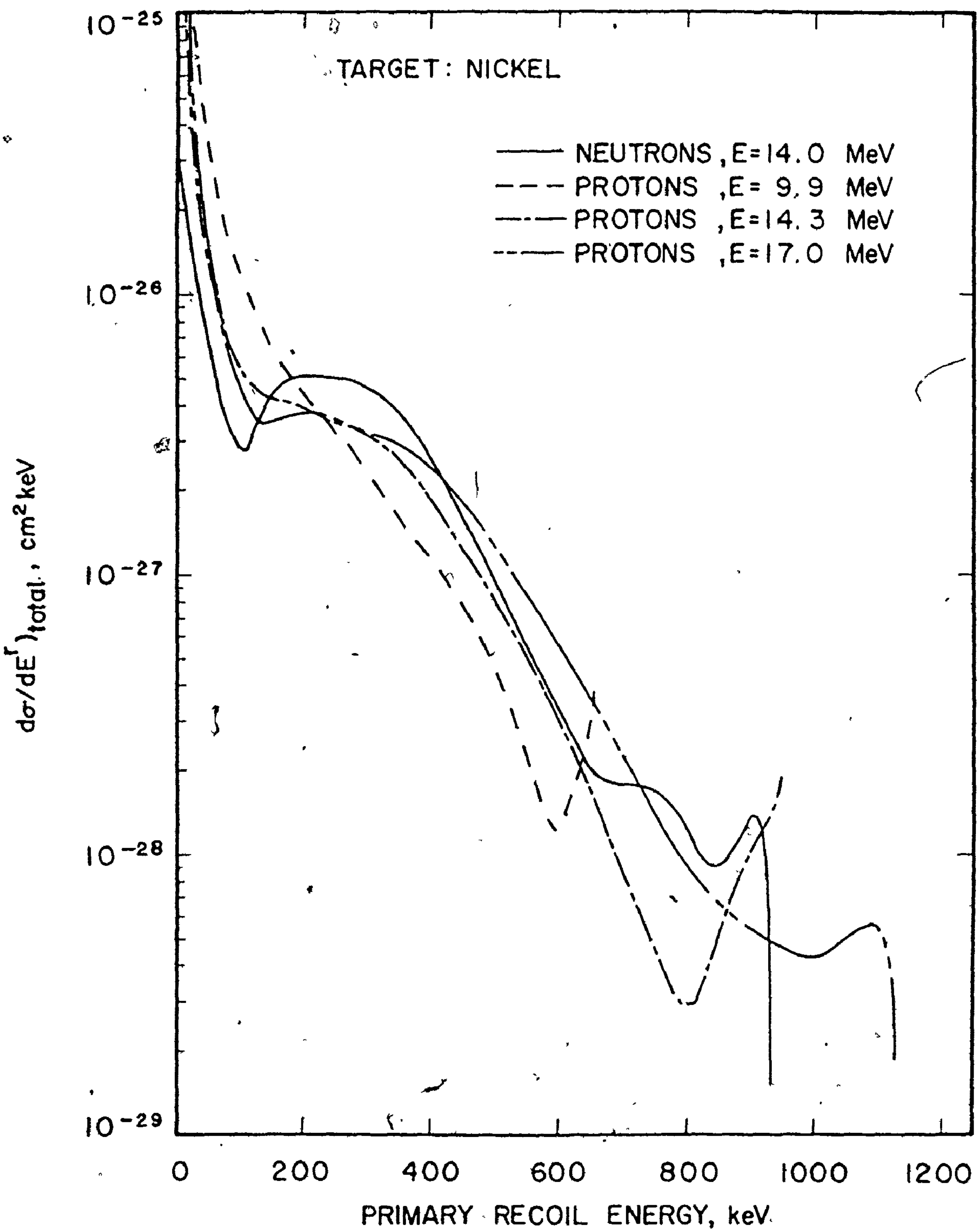

Fig. 4.2: Primary recoil spectra for Ni. Total differential scattering cross-sections, $d\sigma/dE^r)_{total}$, versus the PKA energy E^r.

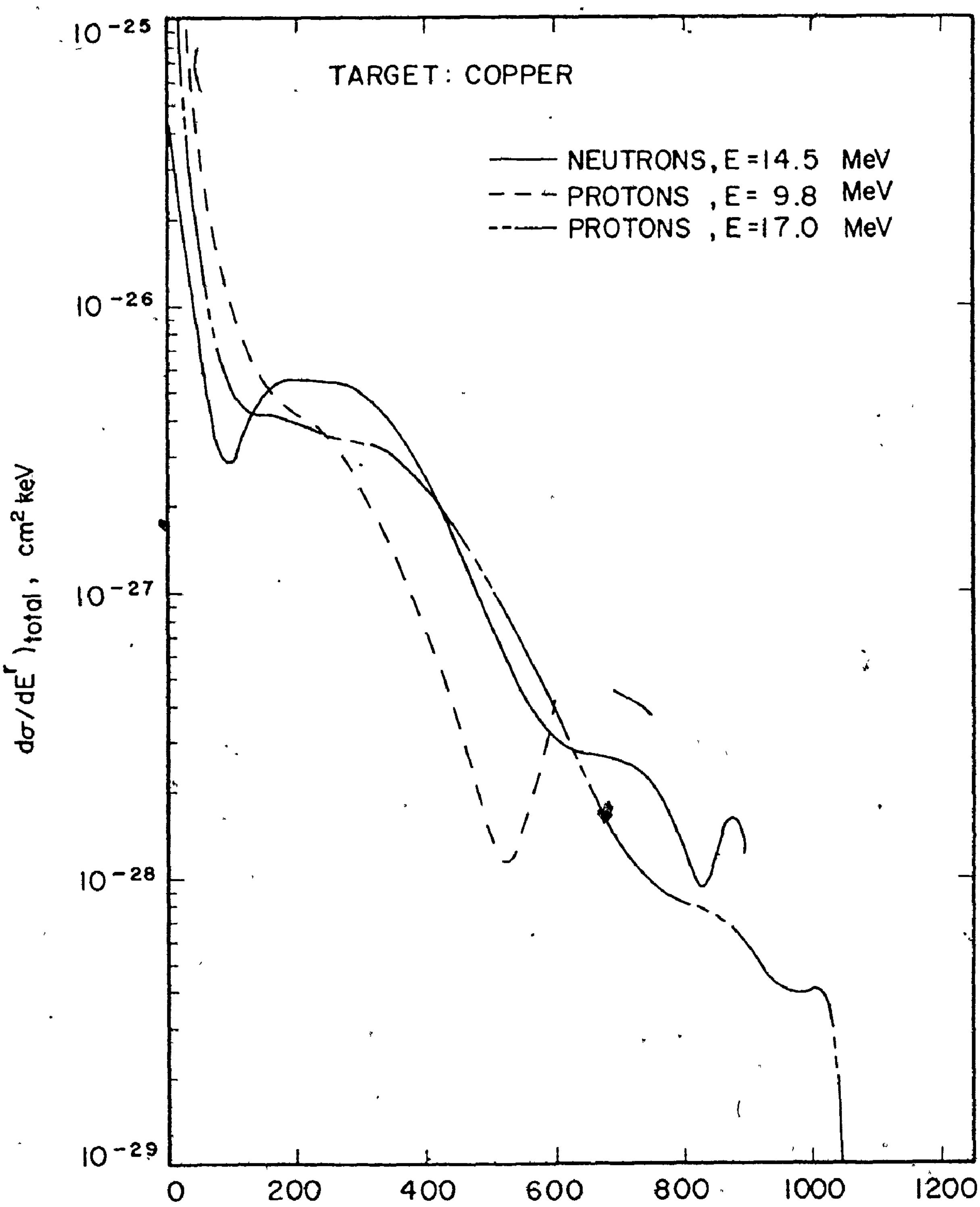

Fig. 4.3: Primary recoil spectra for Cu. Total differential scattering cross-sections, $d\sigma/dE^r)_{total}$, versus the PKA energy E^r.

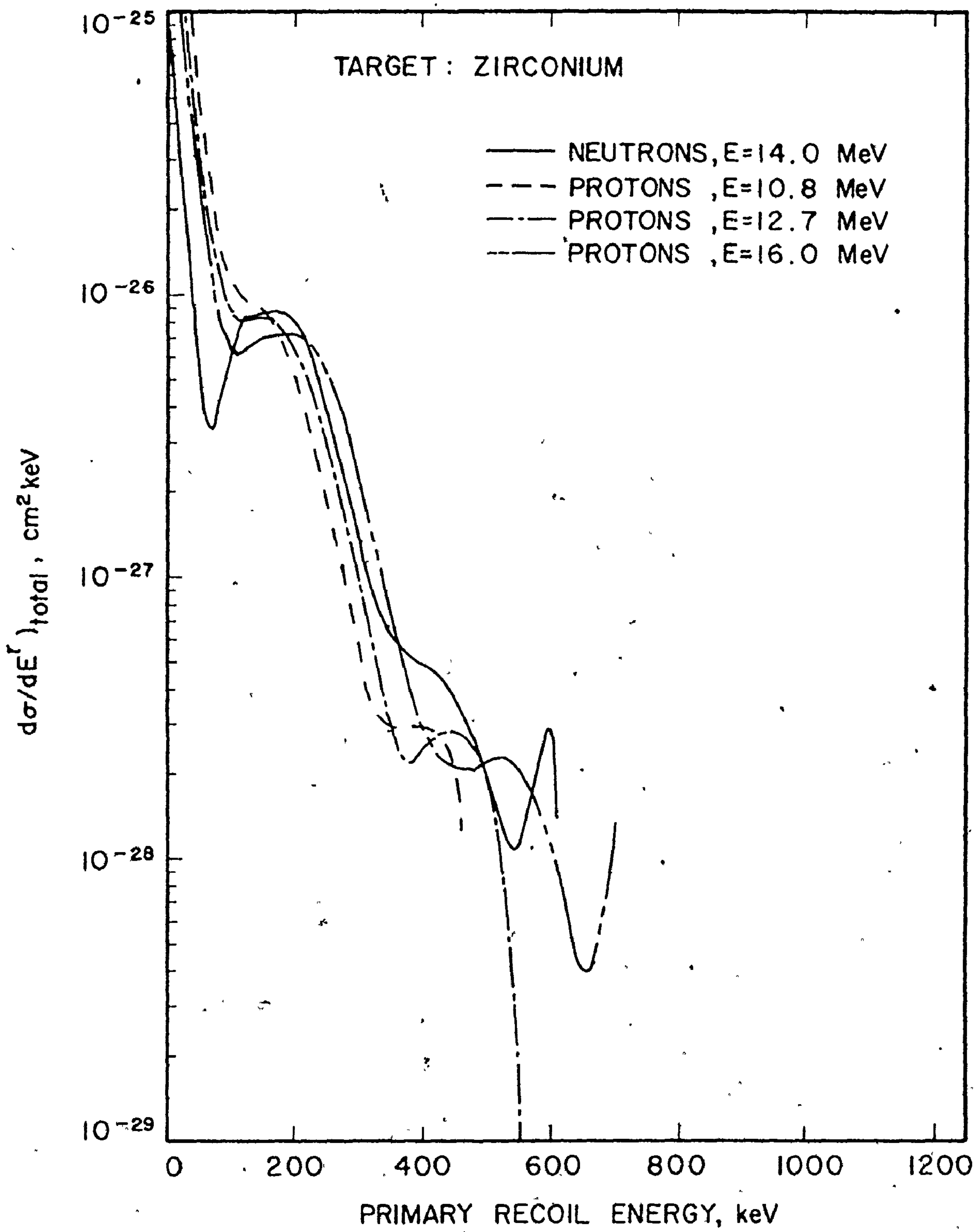

Fig. 4.4: Primary recoil spectra for Zr. Total differential scattering cross-section, $d\sigma/dE^r)_{total}$, versus the PKA energy E^r.

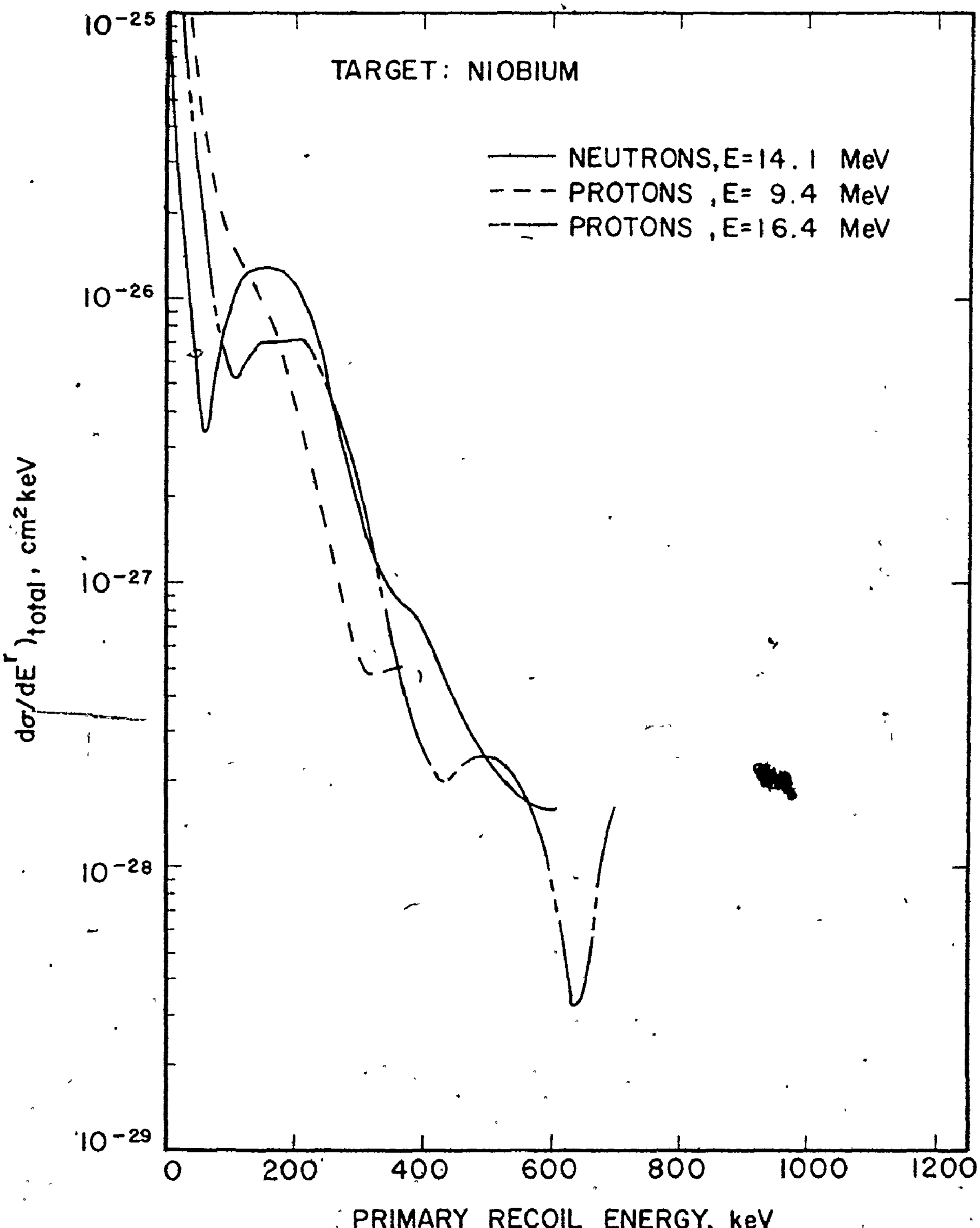

Fig. 4.5: Primary recoil spectra for Nb. Total differential scattering cross-section, $d\sigma/dE^r)_{total}$, versus the PKA energy E^r.

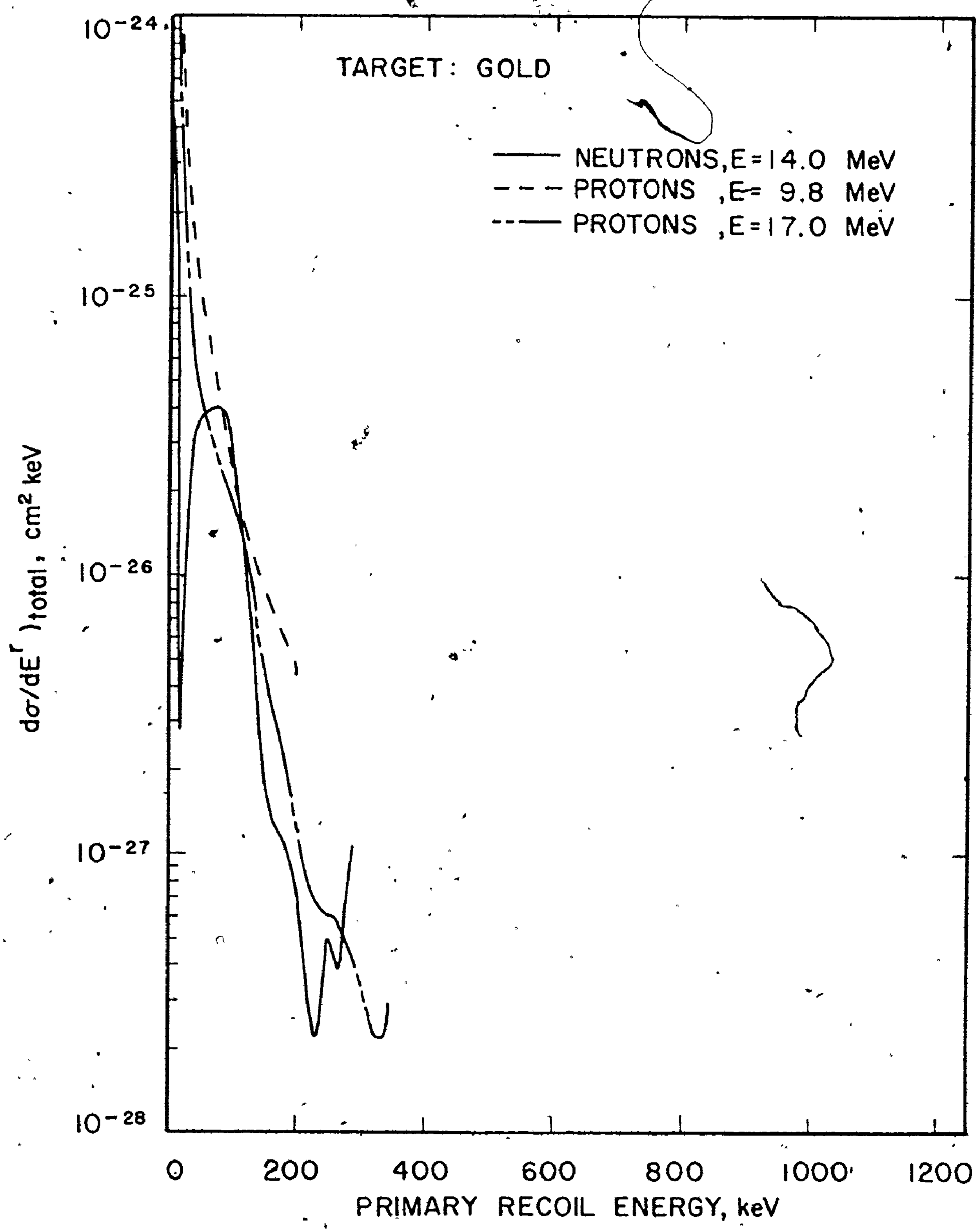

Fig. 4.6: Primary recoil spectra for Au. Total differential scattering cross-section, $d\sigma/dE^{r})_{total}$, versus the PKA energy E^{r}.

dominated by the small-angle Rutherford scattering. However, for the intermediate recoil energies, non-elastic events produce similar maxima near $E^r_{max}/4$ for neutrons and protons. A dissimilarity between the neutron and proton spectra for each element can be observed at high recoil energies. It should be noted that for Au a large difference between neutron and proton cross sections can be seen over the entire range of the primary recoil energies.

The damage energy spectra for the six metals under consideration are displayed respectively in Figs. 4.7 to 4.13. Such plots give the cross section values for creating atomic displacements with the corresponding PKA energy per incident particle. The damage energy E_D is then evaluated according to Eq. 4.1 for selected lower integration limits. Such results are presented in Tables 4-3 to 4-8. Good agreement was found with the earlier calculations of Logan[15] as seen in Table 4-9. The error is within the uncertainty limits of the data base.

4.3 Discussion on the Theoretical Results

As can be seen from Figs. 4.7 to 4.13 and from Tables 4-3 to 4-8, the proton scattering approximates that of the neutrons in both the magnitudes of the damage cross section and in the recoil distribution for energies greater than a few keV, with the exception of the case of gold. Also, the simulation appears

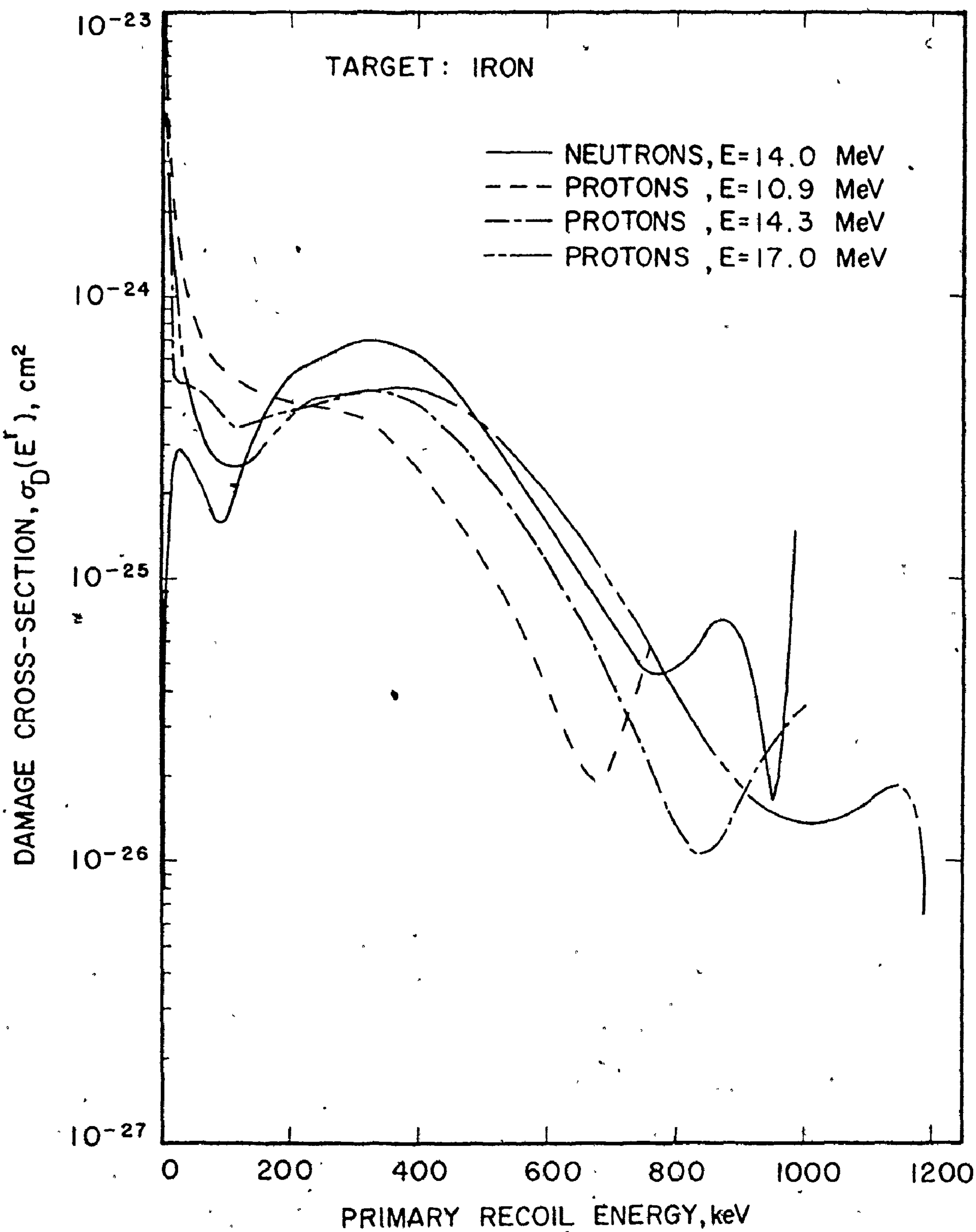

Fig. 4.7: Damage-energy spectra for Fe. Damage cross-section, $\sigma_D(E^r)$, versus the PKA energy E^r.

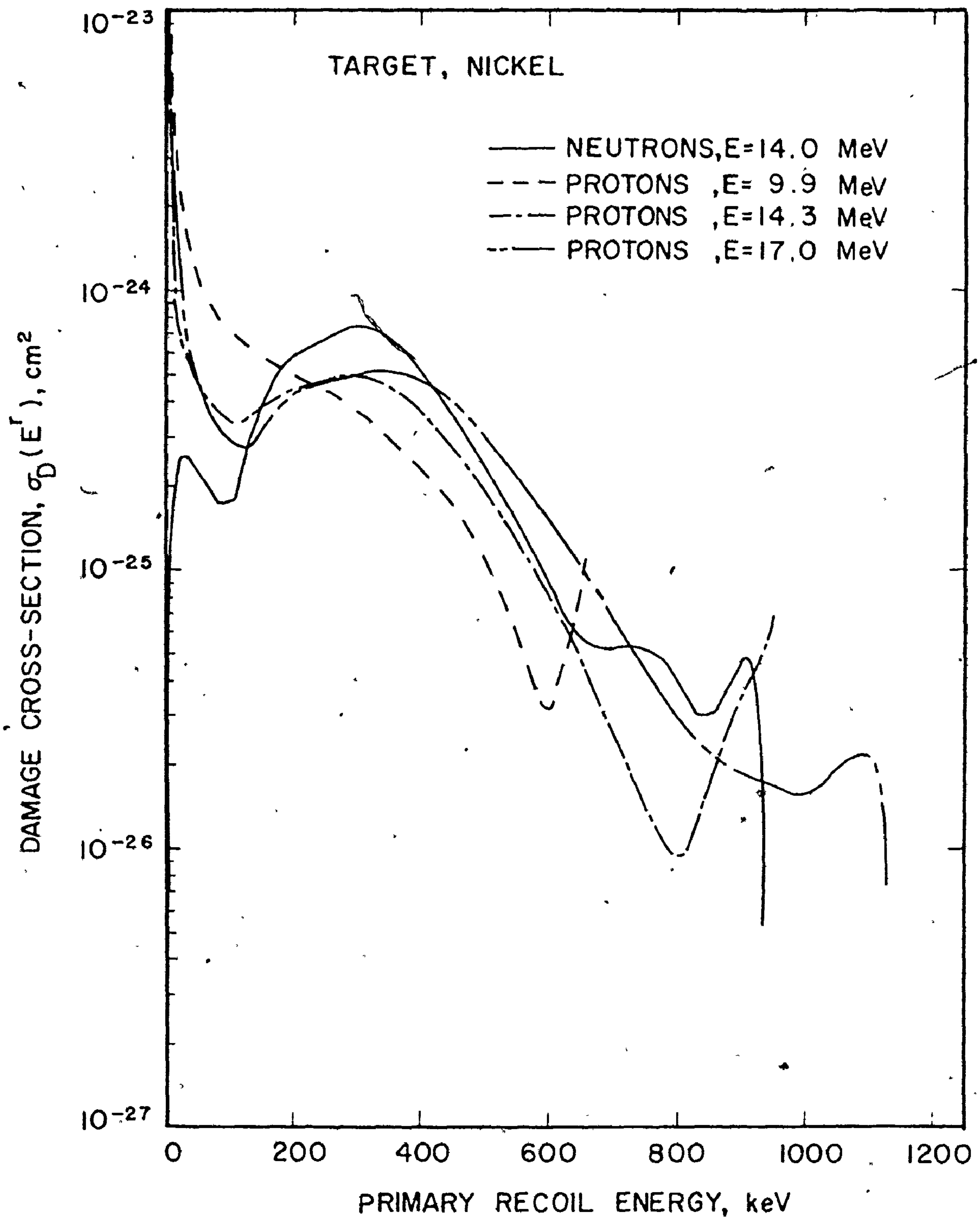

Fig. 4.8: Damage-energy spectra for Ni. Damage cross-section, $\sigma_D(E^r)$, versus the PKA energy E^r.

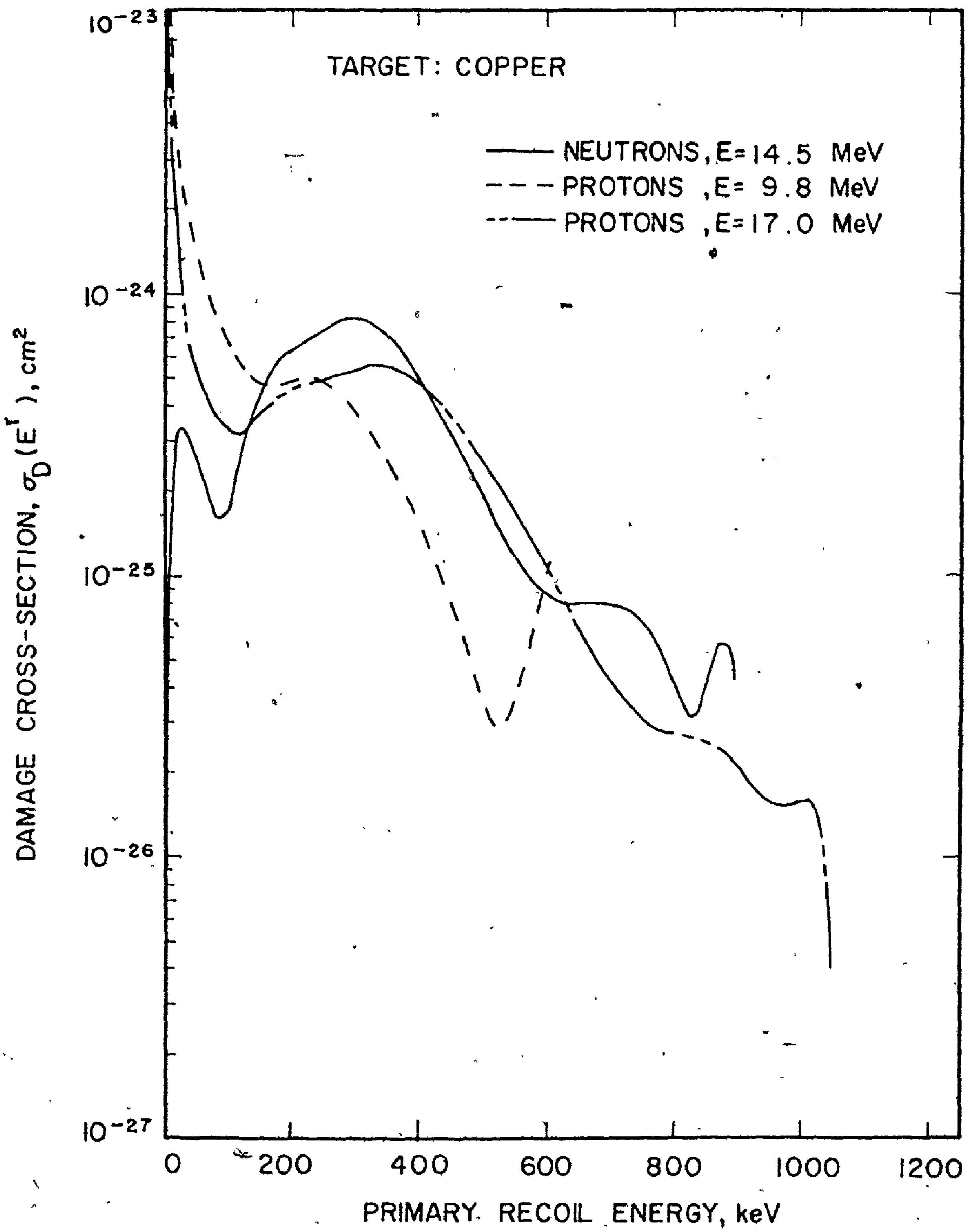

Fig. 4.9: Damage-energy spectra for Cu. Damage cross-section, $\sigma_D(E^r)$, versus the PKA energy E^r.

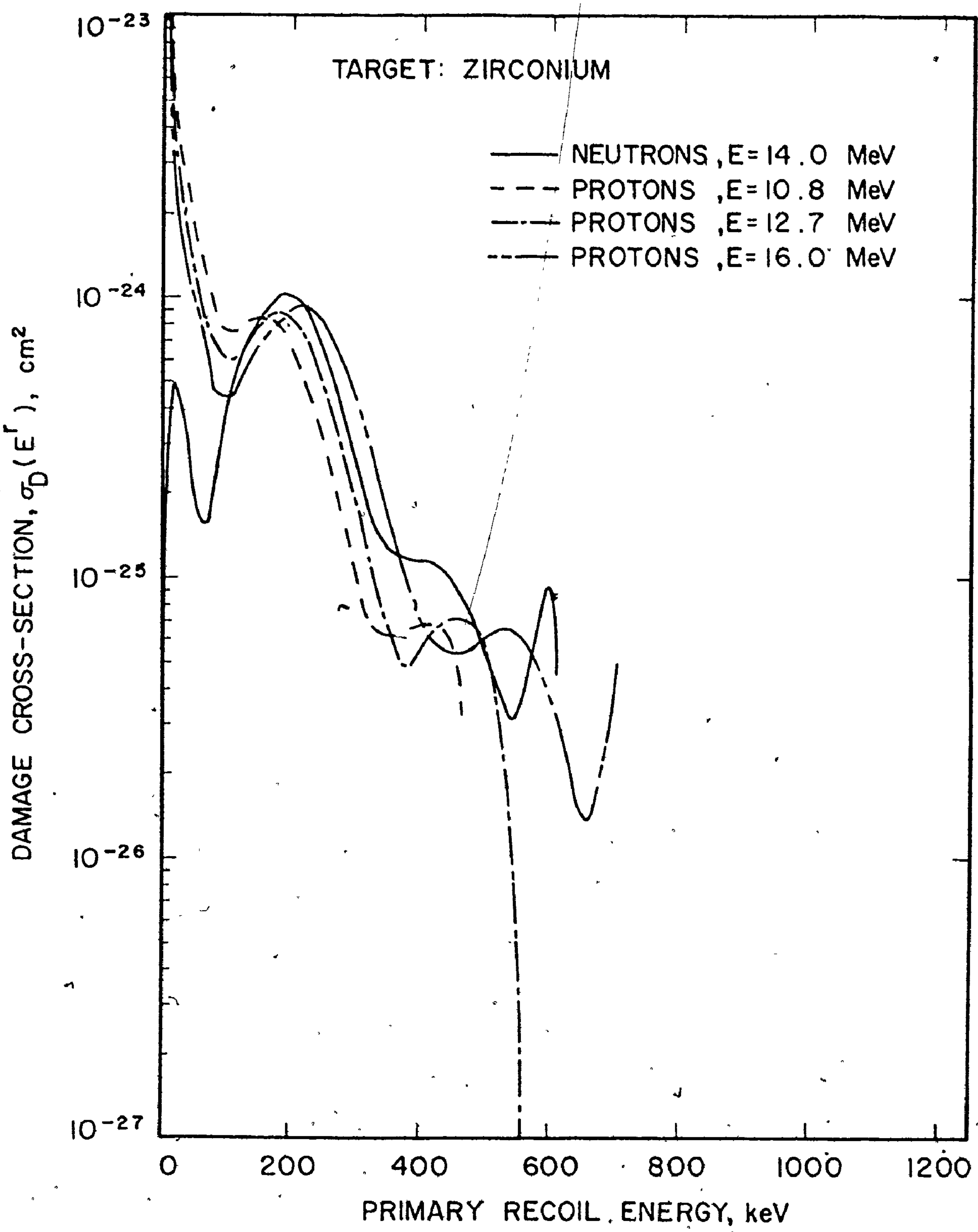

Fig. 4.10: Damage-energy spectra for Zr. Damage cross-section, $\sigma_D(E^r)$, versus the PKA energy E^r.

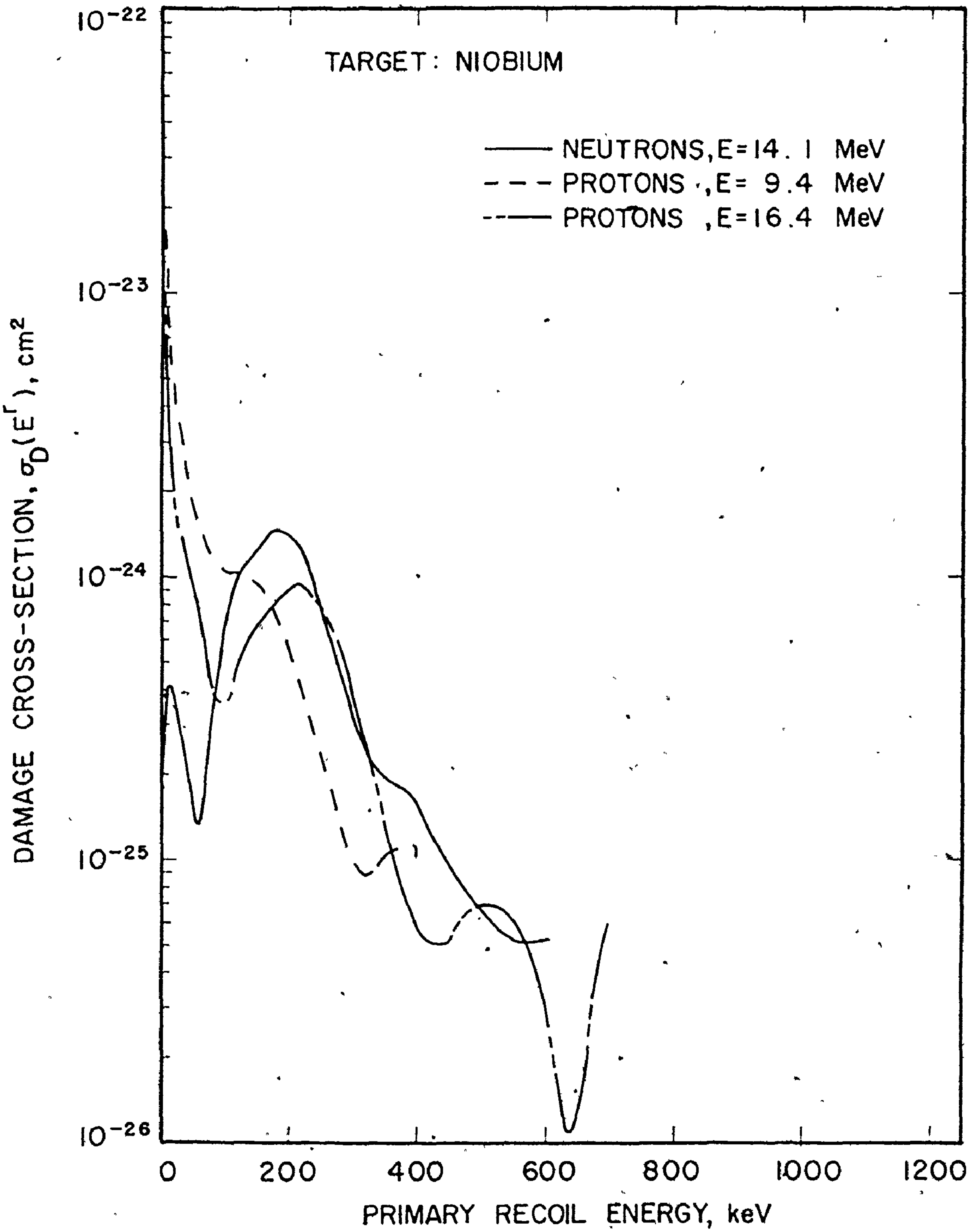

Fig. 4.11: Damage-energy spectra for Nb. Damage cross-section, $\sigma_D(E^r)$, versus the PKA energy E^r.

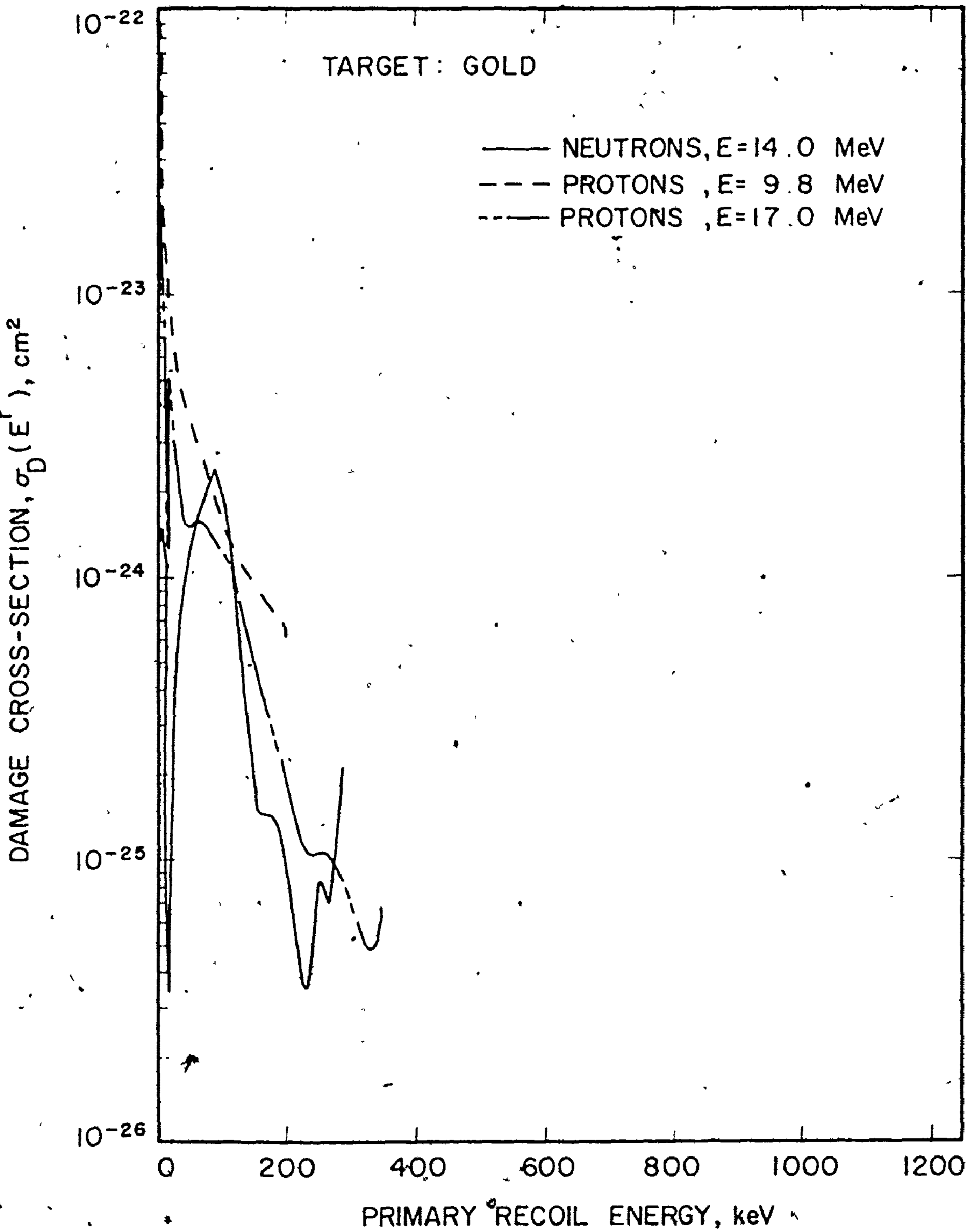

Fig. 4.12: Damage-energy spectra for Au. Damage cross-section, $\sigma_D(E^r)$, versus the PKA energy E^r.

Table 4-3: Damage energies, in barn-keV, integrated from E^r_{max} down to several lower limits of integration for Fe

Lower limit of integration (keV)	Neutrons	Protons		
E_o (MeV)	14.0	10.9	14.3	17.0
E^r_{max} (keV)	981	757	1000	1190
1000.	.0	.0	.0	2.9
800.	9.5	.0	3.8	7.1
600.	25.0	4.5	13.6	27.4
400.	96.2	29.5	62.7	95.5
200.	222.8	100.5	148.8	185.0
100.	257.7	147.1	185.2	213.5
50.	266.9	178.7	206.5	227.8
10.	277.4	243.6	238.0	266.8
5.	277.9	280.4	266.6	290.9
1.	278.5	375.0	338.9	351.7
.5	278.5	418.4	372.2	379.7
.1	278.5	523.3	452.8	447.4
.050	278.5	570.2	488.8	477.8
.035	278.5	594.5	507.5	493.5
.025	278.5	618.0	525.5	508.6
.010	278.5	682.0	574.6	549.9

Table 4-4: Damage energies, in barn-keV, integrated from E^r_{max} down to several lower limits of integration for Ni

Lower limit of integration (keV)	Neutrons	Protons		
	E_o 14.0	9.9	14.3	17.0 (MeV)
	E^r_{max} 930	655	949	1130 (keV)
1000.	.0	.0	.0	2.4
800	4.7	.0	4.2	6.3
600.	15.8	2.9	10.5	21.0
400.	65.8	25.6	49.5	81.3
200.	196.6	98.5	141.2	179.3
100.	234.6	156.3	179.1	211.5
50.	243.9	199.6	198.7	229.4
10.	253.3	293.3	232.0	275.1
5.	253.8	339.0	263.6	301.7
1.	254.2	454.1	343.1	368.5
.5	254.2	508.0	380.2	399.7
.1	254.2	634.0	467.2	472.9
.05	254.2	703.0	514.8	513.0
.035	254.2	734.4	536.2	531.2
.025	254.2	763.2	556.4	548.0
.010	254.2	839.3	608.9	592.1

Table 4-5: Damage energies, in barn-keV, integrated from E^r_{max} down to several lower limits of integration for Cu

Lower limit of integration (keV)	Neutrons	Protons	
E_o	14.5	9.8	17.0 (MeV)
E^r_{max}	892	599	1040 (keV)
1000	.0	.0	0.6
800.	4.0	.0	4.7
600.	18.3	.0	14.5
400.	62.7	13.0	67.5
200	202.3	85.1	168.8
100.	245.1	138.0	206.1
50.	254.1	182.1	226.0
10.	266.2	278.5	273.4
5.	266.8	325.0	300.0
1.	267.5	440.6	366.2
.5	267.5	494.7	397.2
.1	267.5	623.4	471.1
.05	267.5	691.8	510.3
.035	267.5	723.0	528.2
.025	267.5	752.6	545.1
.010	267.5	829.8	589.4

Table 4-6: Damage energy, in barn-keV, integrated from E^r_{max} down to several lower limits of integration for Zr

Lower limit of integration (keV)	Neutrons	Protons		
E_o	14.0	10.8	12.7	16.0 (MeV)
E^r_{max}	606	463	556	701 (kev)
1000.	0.	0.	0.	0.
800.	0.	0.	0.	0.
600.	.5	0.	0.	2.3
400.	14.6	3.9	8.0	13.7
200.	91.7	43.1	65.0	109.3
100.	171.4	121.3	140.8	175.7
50.	183.2	174.1	179.0	206.4
10.	198.0	312.4	284.4	282.2
5.	198.9	369.0	333.6	321.2
1.	199.6	511.2	457.2	419.3
.5	200.4	575.7	513.2	463.8
.1	200.4	730.0	647.3	570.2
.05	200.4	811.0	717.6	626.0
.035	200.4	849.2	750.8	652.4
.025	200.4	884.2	781.3	676.6
.010	200.4	976.7	861.6	740.3

Table 4-7: Damage energy, in barn-keV, integrated from E^{r}_{max} down to several lower limits of integration for Nb

Lower limit of integration (keV)	Neutrons	Protons	
E_o	14.1	9.4	16.4 (MeV)
E^{r}_{max}	599	398	696 (keV)
1000.	0.	0.	0.
800.	0.	0.	0.
600.	0.	0.	2.3
400.	15.3	0.	13.7
200.	116.9	37.0	103.6
100.	236.3	125.5	168.5
50.	251.6	191.0	196.1
10.	263.6	345.4	268.5
5.	264.4	413.4	307.3
1.	265.2	583.9	404.7
.5	266.0	664.6	450.8
.1	266.0	846.9	555.0
.05	266.0	943.4	610.1
.035	266.0	989.2	636.3
.025	266.0	1031.2	660.3
.010	266.0	1142.1	723.7

Table 4-8: Damage energy, in barn-keV, integrated from E^r_{max} down to several lower limits of integration for Au

Lower limit of integration (keV)	Neutrons E_o 14.0, E^r_{max} 284	Protons 9.8, 199	Protons 17.0 (MeV), 344 (keV)
1000.	0.	0.	0.
800.	0.	0.	0.
600.	0.	0.	0.
400.	0.	0.	0.
200.	6.3	0.	13.1
100.	56.3	100.0	74.4
50.	153.3	228.1	148.7
10.	177.8	521.7	270.1
5.	183.0	641.1	339.2
1.	187.2	935.4	509.5
.5	187.7	1070.0	587.4
.1	188.1	1386.6	770.7
.05	188.2	1552.2	866.6
.035	188.2	1631.1	912.2
.025	188.2	1712.1	959.1
.010	188.2	1895.6	1065.3

Table 4-9: Present calculations of the damage energy for Nb in comparison with Logan's[15] results

Lower limit of integration (keV)	Damage energy (barn-keV)						Comments and Remarks
	Neutrons		Protons				
	Logan's 14.1	Present 14.1	Logan's 14.1	Logan's 16.4	Present 9.37	Present 16.4 MeV	
593.6	0	0	0	2	0	2	For (n,n') we used T_n = 0.66 ±0.3 instead of 0.068 used by Logan
500.0	6	5	4	8	0	8	
100.0	222	236	141	165	126	169	
10.0	254	263	259	260	345	269	
1.0	258	264	414	393	584	405	
0.5	258	266	463	435	665	451	
0.036	258	266	655	600	989	636	
0.025	-	266	-	-	1031	660	
0.010	-	266	-	-	1142	724	

to be more accurate for protons with energies more than 14 MeV if 14 MeV neutrons are to be simulated. In the case of Au, only the general features of the collision events are reproduced. In addition, for Au, the large Rutherford scattering is a dominant portion of the damage energy. For the other five elements, namely Fe, Ni, Cu, Zr and Nb, the theoretical results show that the calculated proton induced damage-energy is partitioned approximately equally into damage processes yielding high-energy primary recoils ($\geq$ 10 keV) and low-energy primary recoils (< 10 keV). The corresponding data calculated for 14.0 MeV neutrons indicates that all the induced damage energy is in the form of high-energy PKA's ($\geq$ 10 keV).

The results presented in tables 4-3 to 4-8 are displayed graphically in Fig. 4.13. This shows the total damage energies for 14.0 MeV neutrons in comparison to the damage energies for protons evaluated for selected lower integration limits (E^r_{min}). It is of interest to note that the non-elastic contribution for 14 MeV neutrons is relatively independent of Z and is between the limits of 150-300 barn-keV. A similar trend is also seen for the proton non-elastic collision events which create PKA's with energies above 10 keV. However, when the Rutherford contribution is included for protons, a significant additional damage energy is found due to the low-energy primary recoils. This additional contribution follows a linear increase with increasing Z as is expected for Rutherford scat-

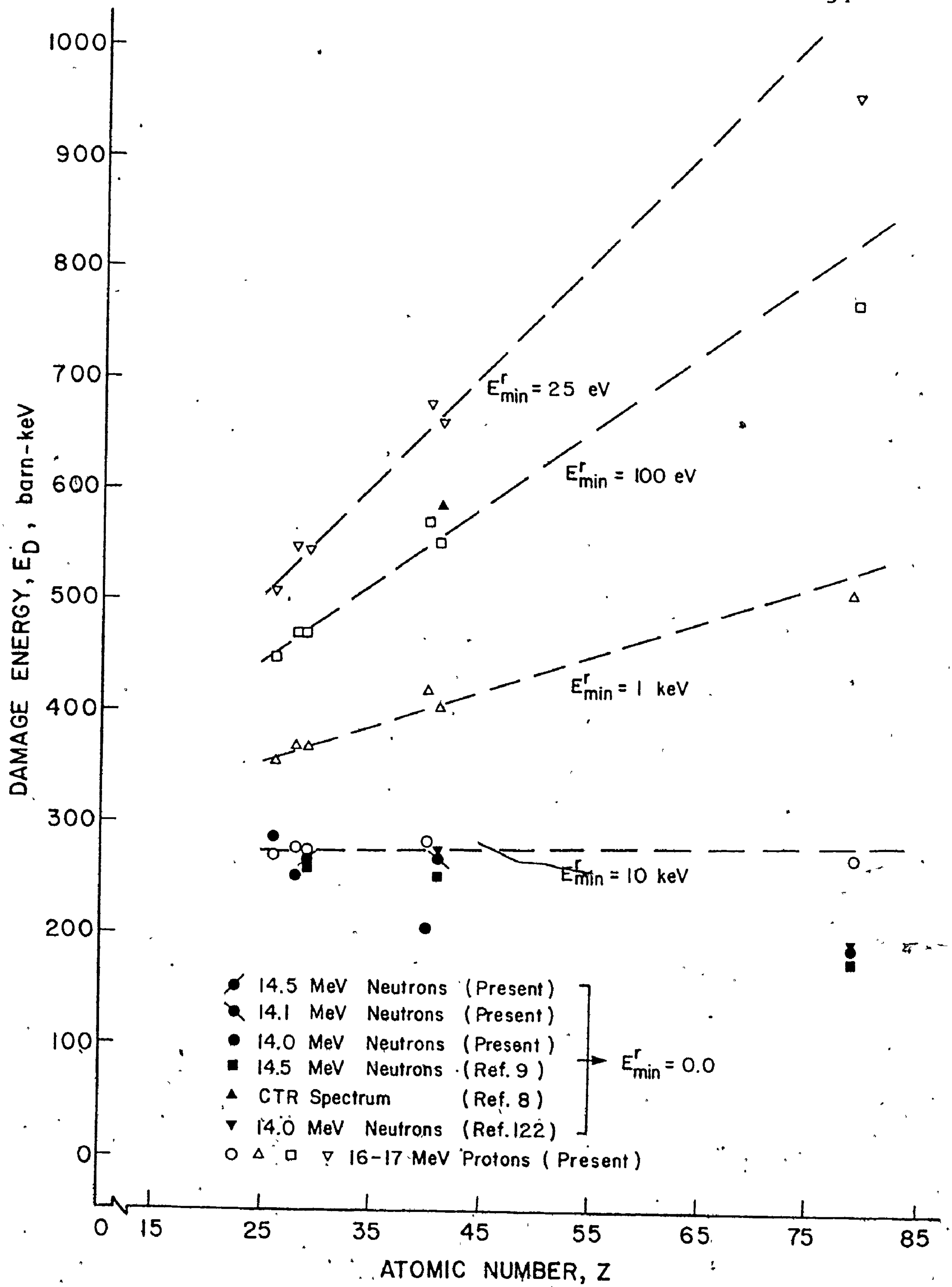
DAMAGE ENERGY, E_D, barn-keV
1000
900
800
700
600
500
400
300
200
100
0
ATOMIC NUMBER, Z
0
15
25
35
45
55
65
75
85
E^r_{min} = 25 eV
E^r_{min} = 100 eV
E^r_{min} = 1 keV
E^r_{min} = 10 keV
14.5 MeV Neutrons (Present)
14.1 MeV Neutrons (Present)
14.0 MeV Neutrons (Present)
14.5 MeV Neutrons (Ref. 9)
CTR Spectrum (Ref. 8)
14.0 MeV Neutrons (Ref. 122)
E^r_{min} = 0.0
16-17 MeV Protons (Present)

tering. When fusion-neutron data was used to calculate the induced damage energy in Nb[8], a value of 583 barn-keV resulted. Such a value is 54% higher than the corresponding estimate which is computed in the present work for a mono-energetic 14.5-MeV neutron data (Table 4-7). If such a CTR damage-energy value is plotted in Fig. 4.13, one finds out that 16-17 MeV protons approximate the induced damage in this case even if recoils of energies as low as 80 eV are included. This feature may be attributed to the fact that a fusion spectrum comprises neutrons with energies ranging between 10^{-4} MeV and 14 MeV[8]. In subsequent chapters, we will use these calculations when interpreting our experimental data. Because of the limited scope of the thesis, that is, that both experiment and theory are pursued, we have not considered the theoretical description in any more detail than is presented in this chapter.

CHAPTER 5

EXPERIMENTAL METHOD: SAMPLE PREPARATION AND EXPERIMENTAL FACILITIES

5.1 Sample Preparation and Mounting

The materials used in the irradiation experiments were cold-drawn wires."Marz-grade" α-iron and zirconium wires, 61 μm in diameter,were supplied by Materials Research Corporation. The high purity* 122 μm copper wire was supplied by R. R. Coltman, Jr. of Oak Ridge National Laboratory. The specimen wires were wound on 250 μm thick anodized aluminum sheets to form either a target or a reference sample. Each target and reference sample was separated by an anodized aluminum sheet to form a "specimen stack". Fig. 5.1 displays the different sheets used for each stack. It was possible to mount two specimen stacks for the same irradiation run. This is shown in Fig. 5.2. Heat-sinking compound was applied between all parts to provide good thermal contact. The iron and copper samples were soldered directly to two lead-stations positioned on the sides of the target-holder body. For zirconium, brass contacts were spot-welded to the sample terminals before being soldered to the lead-stations. The reference sample, mounted away from the beam, was soldered in series with the target. It was used to detect any variation in the base temperature.

---

* $R_{296}/R_{4.2K} = 1432$

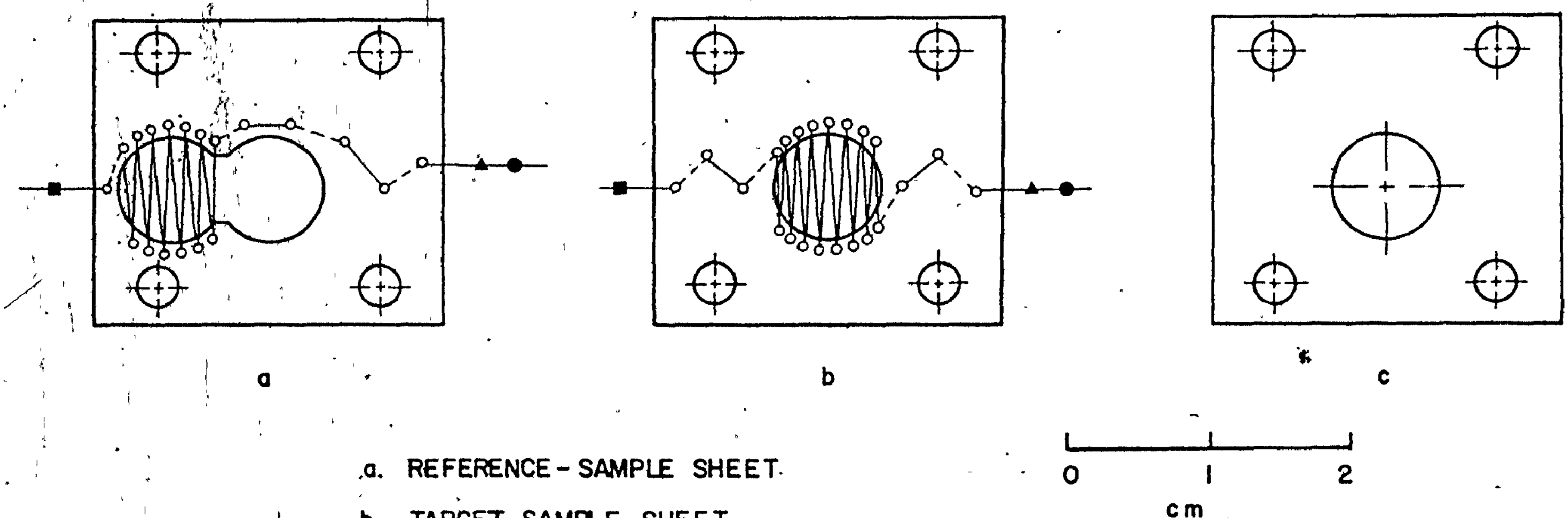

a. REFERENCE-SAMPLE SHEET

b. TARGET-SAMPLE SHEET

c. INSULATING SHEET

● CURRENT-LEAD POINT

▲ POTENTIAL-LEAD POINT

■ TARGET-REFERENCE TAP-POINT AND CENTRAL POTENTIAL LEAD-POINT

Fig. 5.1: Anodized aluminum specimen-sheets.

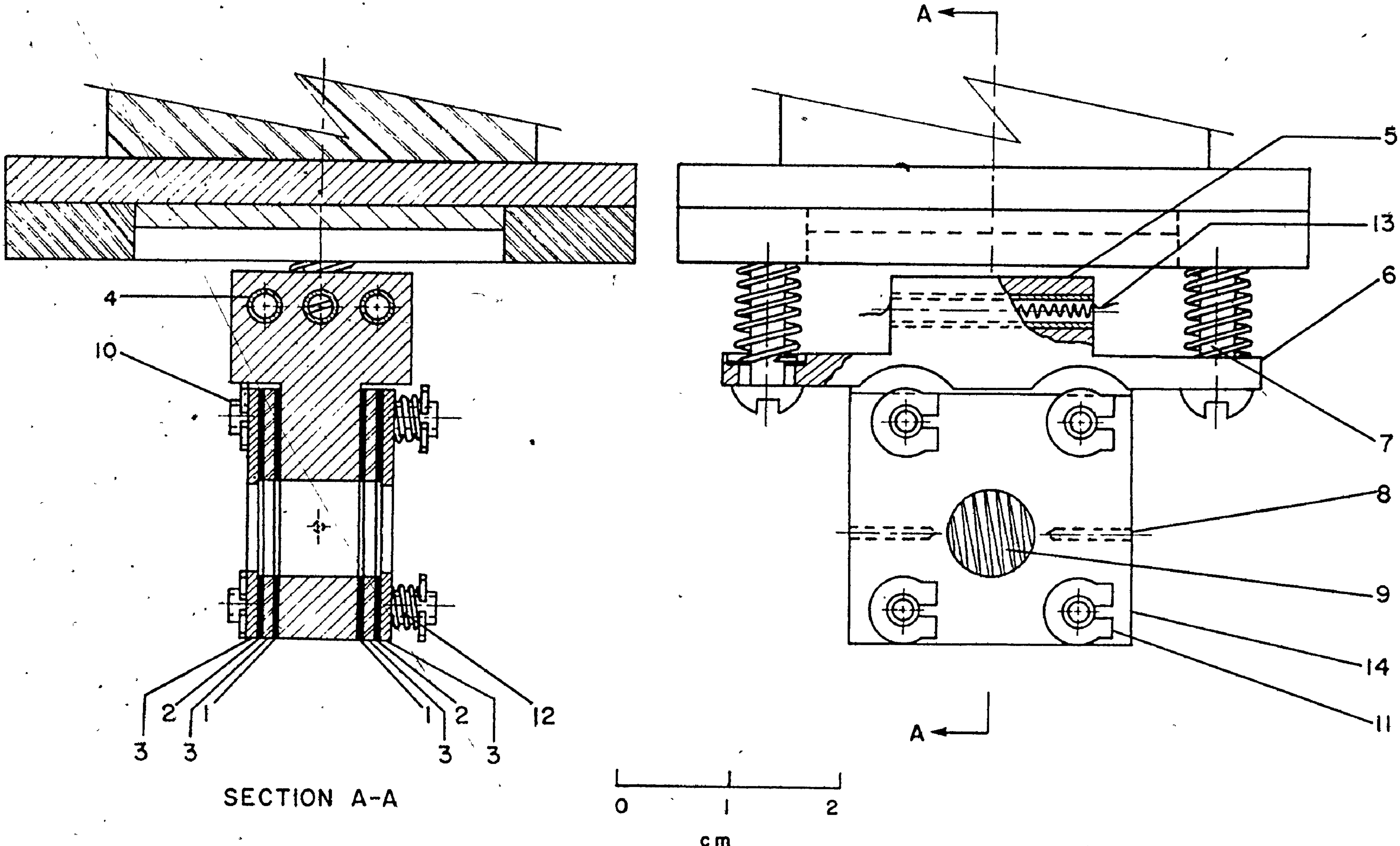

Fig. 5.2: Sample holder assembly.

Normally, one of the Fe specimen stacks was irradiated as-received. The other stack was wound on the sheets and then annealed at 350°C for 2 hrs in a vacuum of 10^{-7} Torr. Such annealing conditions reduce the dislocation density in the sample without changing the grain size[95]. The copper wires were wound as-received onto two specimen stacks. One of these stacks was annealed for 2 hrs at 600°C[96] in a vacuum of 10^{-7} Torr in the presence of an oxygen-gettering material. When these conditions were applied for Zr annealing, it was found that the Zr wires were significantly oxidized. This problem could not be avoided in the annealing facilities that we used. In choosing the samples dimensions and experimental conditions, deviations from Matthiessen's rule were kept as small as possible.

5.2 Closed Cycle Helium-Cooled Cryostat

It was essential to have a method for heating and quenching the samples, and to have a proper temperature-control system in order to perform an isochronal annealing process. The normal practice is to use liquid helium to cool the samples to ~ 4 K during irradiation[97]. Post-irradiation temperature cycling is obtained in such systems by regulating the pressure of gaseous helium or the flow of liquid helium around the samples. This technique is often inconvenient since it requires access to a continuous supply of liquid helium. With recent advances in the closed cycle helium-expansion refrigerator technology, low temperatures and moderate cooling capacities can now conveniently be obtained with a two stage cryocooler[98,99].

The cryostat system used in the present work comprises a two-stage helium cooled cryocooler, rated at 10 W at 20K, and the target assembly as shown in Fig. 5.3. The target temperature is controlled with a mechanical thermal contact switch linking the cryocooler cold head to the target holder and by three nichrome wire heaters. (For details see Fig. 5.2). The target can be cooled by closing (under pressure) the mechanical switch using an externally controlled mechanical linkage system. To increase the target temperature, the pressing force is removed. The target holder, mounted on two spring loaded stainless steel rods, is then pushed away from the cold head breaking the thermal contact. The target temperature can subsequently be increased by using the three nichrome wire heaters. With the mechanical contact closed, the minimum second-stage cold head and target temperatures are 10-13K and 13-17.5K respectively. This compares favourably with the unloaded cryocooler temperature of 8K.

The mechanical linkage system consists of a brass pushing bar, two stainless steel pushing rods, a semicircular lever, and a force transmitting mechanical feedthrough. Teflon is used at the mechanical joints to reduce heat conduction along the linkage. The mechanical linkage system is shown in Fig. 5.4. The mechanical feedthrough is externally attached

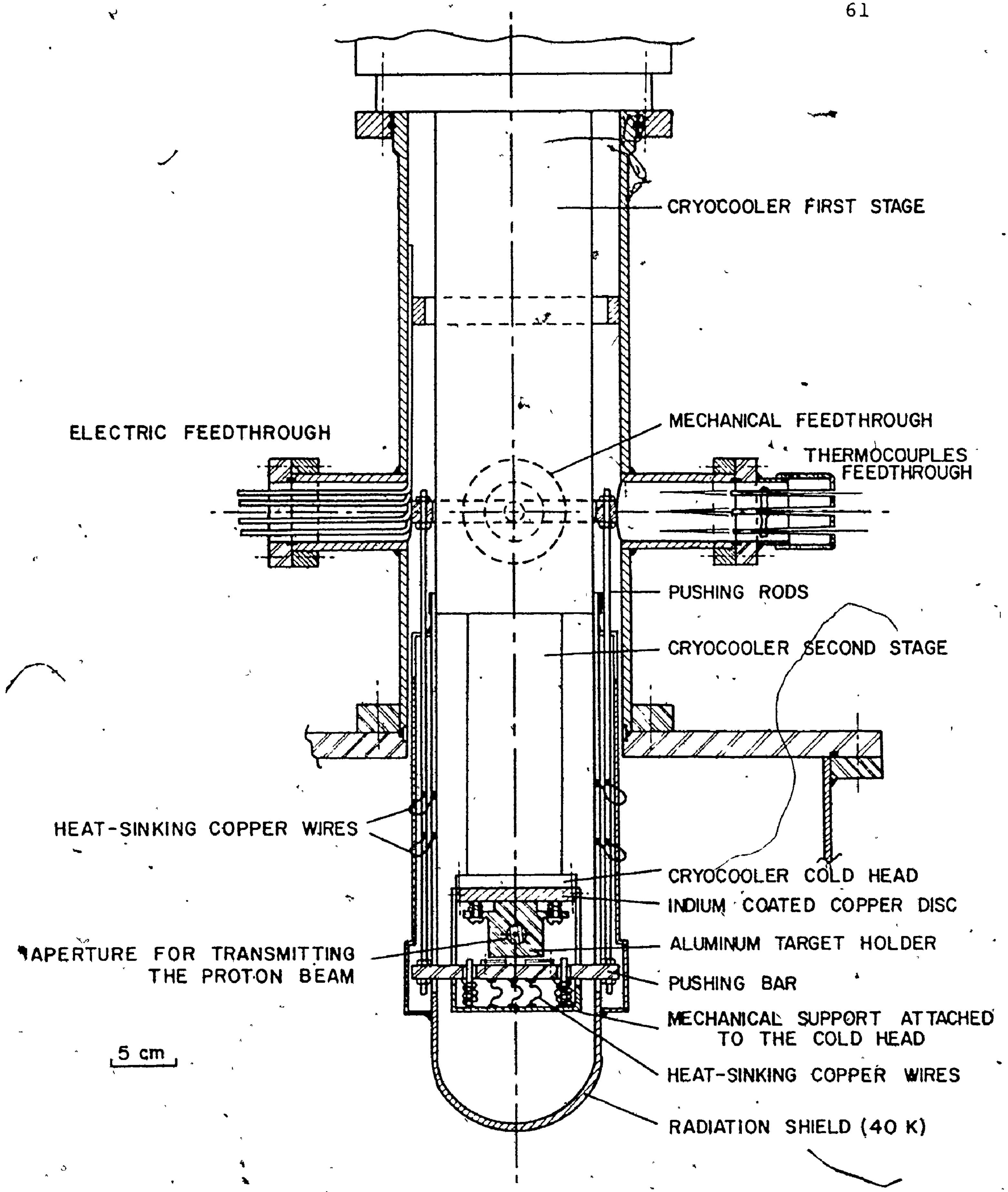

Fig. 5.3: Cryostat system.

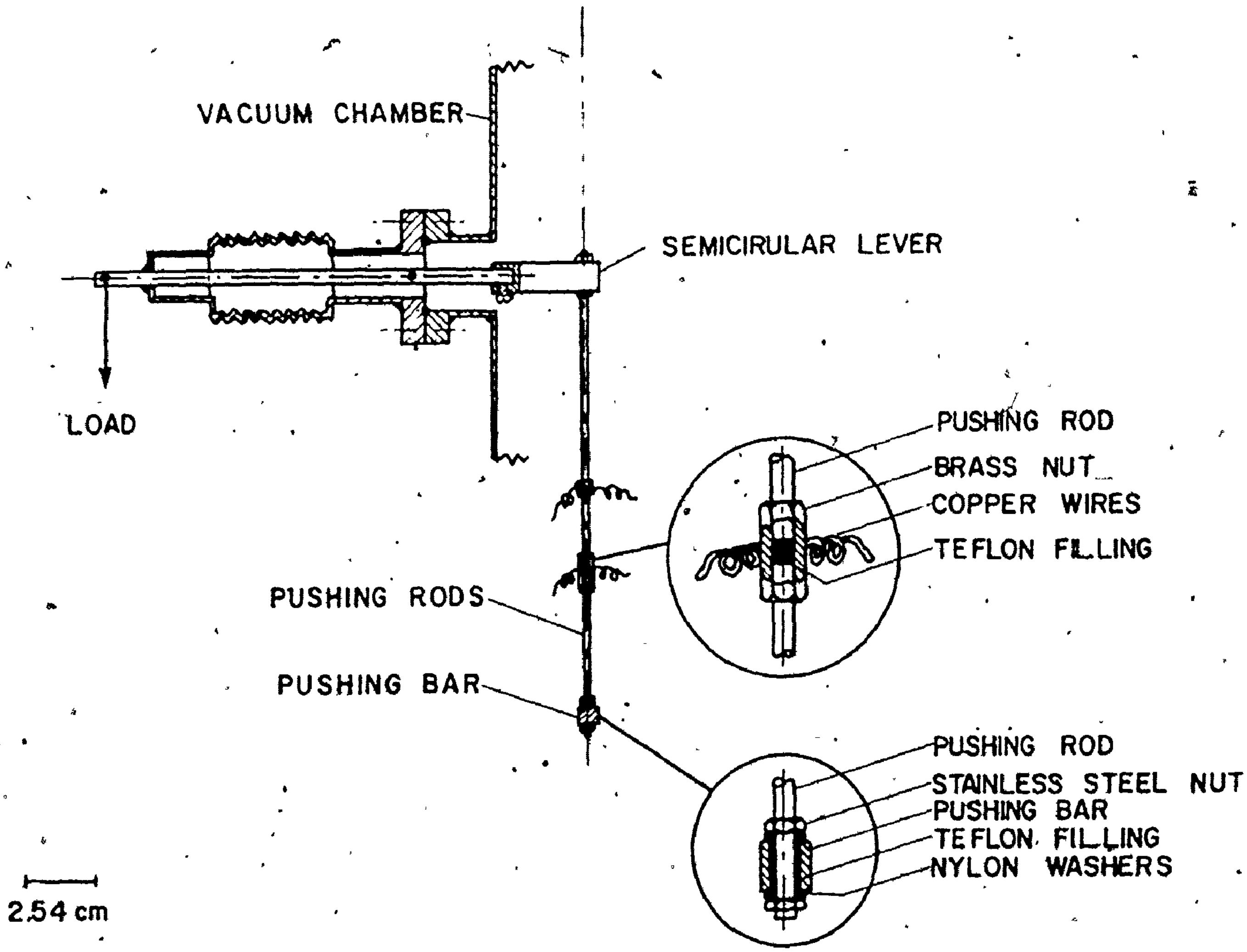

Fig. 5.4: Load-transmission linkage mechanism.

to a tension spring, a torque arm, a gear train, and a servo-motor assembly. The mechanical linkage system can be used to apply contact loads of up to 30 kg wt. to the thermal contact switch. Heat leakage from the mechanical linkage system is reduced by anchoring the pushing bar to the cold head and the pushing rods to the heat shield with heavy flexible copper wires. The pushing bar is insulated from the target holder by thick strips of mica. The heat shield is attached to the first stage of the cryocooler at 40K.

Aluminum was used for the sample holder assembly since it is light and exhibits good thermal properties at very low temperatures[100]. To provide electrical insulation between specimen stacks and the holder, all surfaces were anodized except for the thermal contact surface. The latter was mechanically polished to 1 μm and ultrasonically cleaned in an acetone bath. The other thermal contact surface was a polished copper disc, silver pasted and bolt tightened to the cryocooler cold head. A 0.5 mm thick indium contact layer was produced by fusing indium to the polished copper disc in an atmosphere of pure nitrogen gas. In preliminary tests, the performance of the contact was investigated under several closing loads in a vacuum of 2×10^{-8} Torr[101]. High conductance was achieved in such tests for relatively low closing loads.

Typical isochronal cycles are shown in Fig. 5.5 for annealing temperatures of 85K and 136K. The temperature was

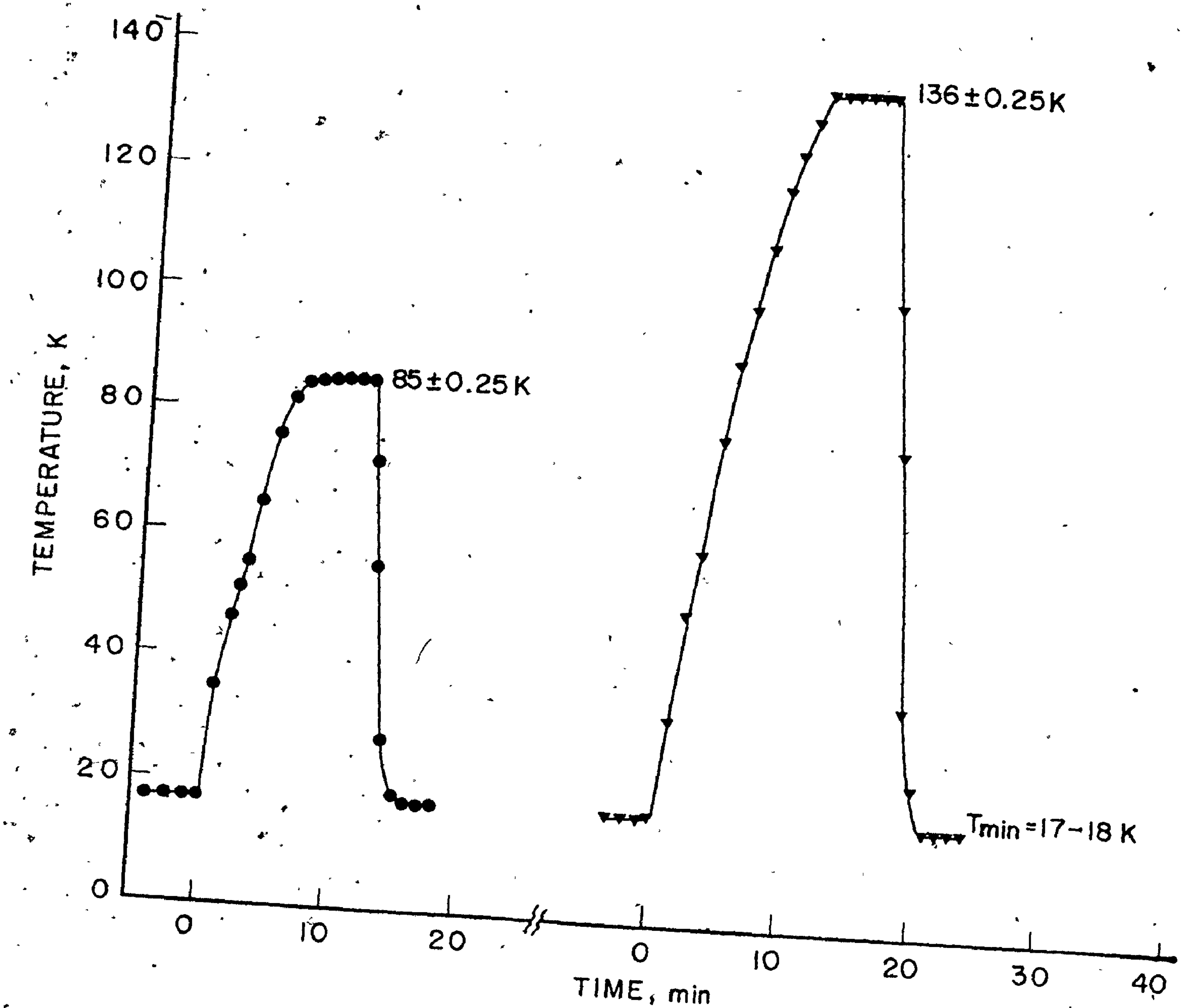

Fig. 5.5: Typical isochromal pulsers at 85 and 136 K.

kept constant to within ±0.25K at each annealing level. The heating current was continuously controlled to avoid over-shooting. Such an overshooting shifts the recovery peak away from its anticipated temperature by a few degrees[102].

5.3 Temperature and Resistivity Measurements

Copper wires of 127 μm in diameter were used as current and potential leads. A direct current was fed to the nichrome heating unit using 254 μm copper wires. The sample temperatures were measured by two 127 μm Chromel-Gold (0.078% Fe) thermocouples[103] calibrated against a referenced GaAs temperature sensor. Preliminary measurements with such thermocouples indicated a uniform temperature distribution within 1.0K over the sample holder assembly. The lead wires and the thermocouple leads were heat-anchored to the second stage of the cryorefrigerator to minimize heat leakage. The variable conductance of the thermal contact switch provides a good means for controlling the target temperature, particularly for annealing cycles below 50K. For higher temperatures, the heating unit was used to achieve the required annealing level. During the isochronal period, both the load on the thermal switch and the heating current were monitored manually.

The absolute resistance of the sample was measured using a potentiometric method. A constant current of 30.00±0.01 ma was used for Fe and Zr samples while a current of 500.0±0.3 ma was employed for the Cu run. The current is applied to reference and target samples connected in series in each stack. A 10.0 Ω standard resistance was mounted in series with the specimen stack to double-check the current value employed. This set-up yielded an error in the current readings between 3×10^{-2} and 6×10^{-2}% as detected with a digital voltmeter. The uncertainty in the voltmeter reading was less than ± 1.0 μV. The estimated uncertainty in the absolute resistance was, therefore, in the range of 4×10^{-8} to 2×10^{-6} ohm.

The change in the target resistance was corrected against base temperature variations by employing the formula

$$\Delta R_c = \Delta R + \Delta R_r \; (R_o/R_{or}) \qquad 5.1$$

where Δ indicates a difference between the measured value at any anneal step and the pre-irradiation value; R_c, R and R_o are the corrected, measured and pre-irradiation target resistances respectively. The quantities R_r and R_{or}, respectively, represent the measured and the pre-irradiation reference resistances. The irradiated length was measured by a microdensitometer from an x-ray photographic plate with an error of 2.5%. The irradiated wire diameter was measured to ±1.0 μm by an optical microscope.

5.4 Proton Source and Beam Alignment

The 9 MV terminal voltage McMaster Tandem Accelerator was used to generate a beam of 10 to 16 MeV protons. The cryostat, including the target assembly, was mounted on the beam line as shown schematically in Fig. 5.6. A set of ion pumps was employed to keep the vacuum of the line in the vicinity of 2×10^{-7} Torr. Before reaching the target assembly, the proton beam was shaped and manipulated by a set of magnetic steerers and two quadrupole magnetic lenses. Following this beam transport, the beam passed through a 4-segment aperture 0.5 cm in diameter. Therefore, this circular-shaped beam entered a 0.55 cm aperture placed in front of the target, irradiated the two target specimens, and was collected in a Faraday cup positioned at the end of the beam line. The total current-time product was determined from a current integrator on the Faraday cup. The area required for the dose evaluation was determined using the irradiated target before demounting. An x-ray photograph was used for this purpose in conjunction with a microdensitometer.

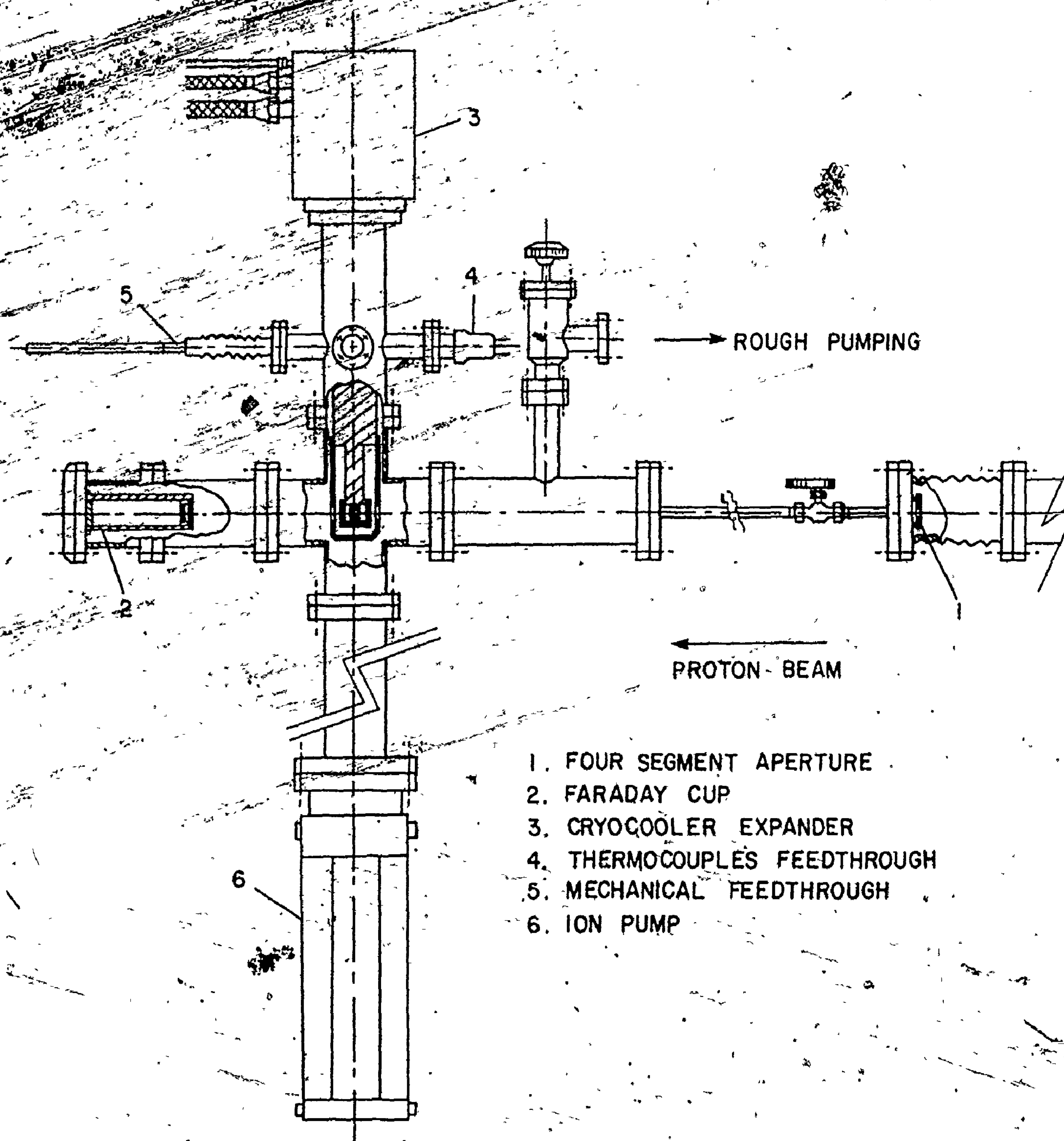

Fig. 5.6: Beam alignment and irradiation set-up.

CHAPTER 6

RESISTIVITY-DOSE MEASURMENTS

In this chapter, results for Fe, Zr and Cu irradiated with 10-16 MeV protons to several dose levels are presented. Table 6.1 summarizes the specimen parameters before and after irradiation for Fe, Zr and Cu.

6.1 Experimental Observations

6.1.1 Iron

The early runs (one to six) were carried out using a 16.0 MeV proton beam. The change in resistivity due to irradiation, $\Delta\rho_i$, with the bombarding dose was measured at several base temperatures and subsequently normalized to a base temperature of 17.5 K. For the as-received samples, the dose was varied from 3.8×10^{16} to 1.56×10^{17} p cm^{-2}, resulting in a resistivity change between 0.332 and 1.224 μΩ cm, respectively. In addition to the as-received specimens, run number two also included an annealed sample. After being irradiated by 1.56×10^{17} p cm^{-2}, the annealed sample featured a resistivity change of 0.884 μΩ cm. These early runs were undertaken to test the irradiation and isochronal facilities. It was found that the resistivity-dose results,

Table 6-1: Sample parameters before and after irradiation

Run #	Base Temp. K	R.R.*	E_o MeV	Max. Dose 10^{16} p cm^{-2}	$\Delta\rho_i$ $\mu\Omega$ cm
As-Received Fe					
1	14.1	not measured	16	7.3	0.624
2	12.8	16.40	16	15.6	1.224
3	16.8	19.80	16	7.4	0.618
3	16.8	20.25	16	7.4	0.613
6	17.0	19.95	16	3.7	0.332
9	17.5	20.11	16	3.5	0.309
11	17.5	20.64	10	3.5	0.375
12	17.5	21.28	14	3.4	0.324
13	17.5	20.46	10	8.7	0.776
Annealed Fe					
2	12.8	64.20†	16	15.6	0.884
9	17.5	109.29	16	3.5	0.250
11	17.5	92.82	10	3.5	0.325
12	17.5	117.23	14	3.4	0.270
13	17.5	119.55	10	8.7	0.700
As-Received Zr					
6	17.0	35.20	16	3.7	0.908
14	17.5	37.28	16	3.5	0.881
15	17.5	35.36	10	3.6	1.282
16	17.5	35.86	16	7.7	1.856
Annealed Cu					
17	17.5	546.75	16	2.0	1.853×10^{-2}

*Resistivity Ratio, $R_{296K}/R_{Base\ temperature\ (K)}$

†Annealed at 600°C for 2 hrs and then wound on the sample-sheet

which were taken with the mechanical heat switch closed, were reproducible. When isochronal cycling was attempted using an earlier design of the sample holder, repeatable results could not be obtained. Accordingly, some modifications were made to the sample holder assembly and two test runs (7 and 8) were performed to check on the adequacy of the new design for undertaking isochronal annealing. Finally, the design presented in Chapter 5 was devised and used successfully in the subsequent irradiation and resistivity recovery measurements. In runs number 9 through 12 the total dose was kept constant at approximately 3.5×10^{16} p cm^{-2} while the incident energy was varied from 10 to 16 MeV. The observed resistivity change was between 0.309 and 0.375 μΩ cm for the as-received samples, and between 0.250 and 0.325 μΩ cm for the annealed cases. Run number 13 was undertaken using an incident energy of 10 MeV with a dose of 8.8×10^{16} p cm^{-2}. This yielded $\Delta\rho_i$ of 0.776 and 0.700 μΩ cm for the as-received and annealed samples respectively.

The observed resistivity changes as a function of dose are displayed for as-received specimens in Fig. 6.1 and for annealed targets in Fig. 6.2. The solid curves represent a fourth-order polynomial fitted to the experimental points using a least-square approach. From Figs. 6.1 and 6.2, it can be observed that for doses below approximately 2.0×10^{16} p cm^{-2} the experi-

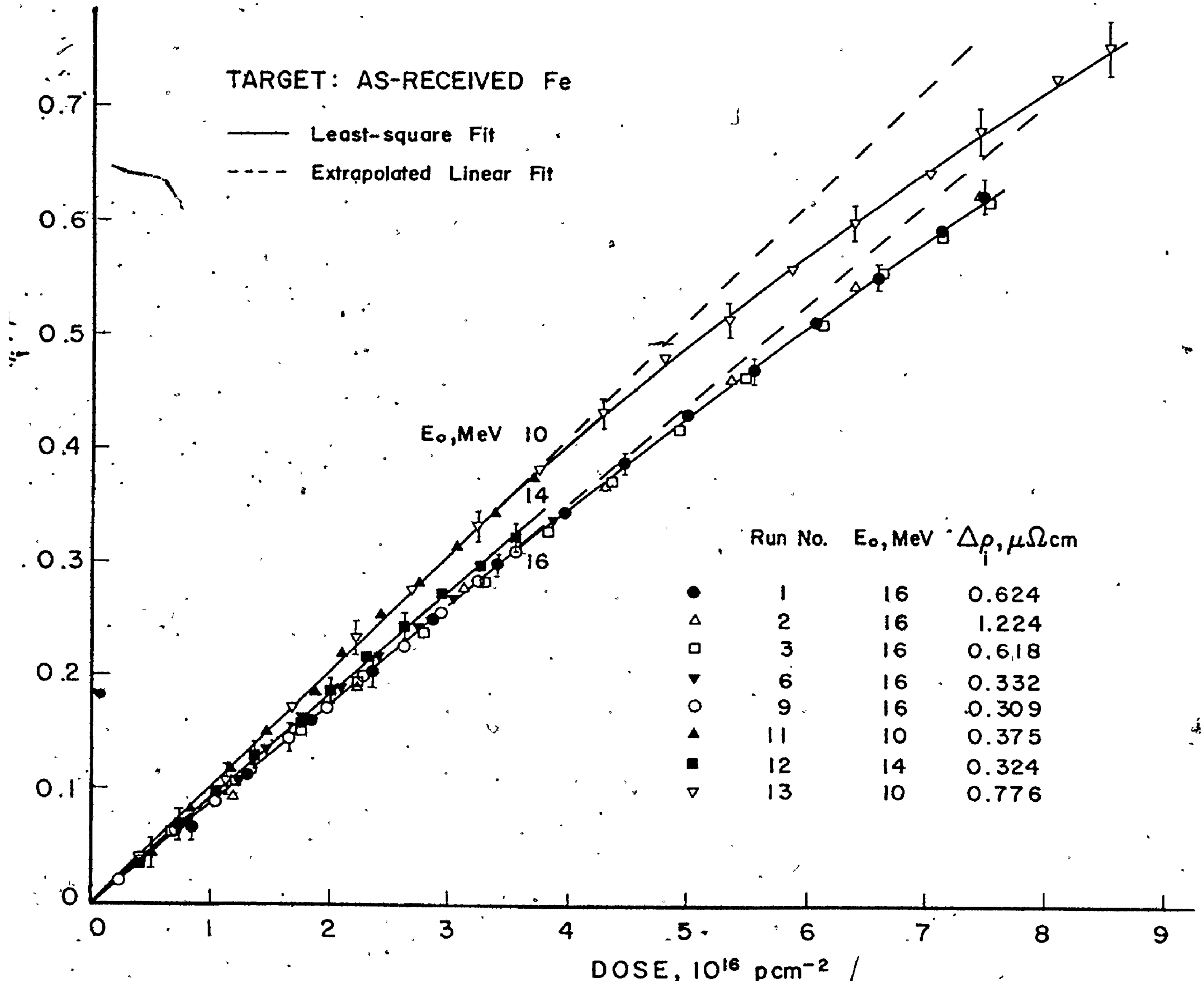

Fig. 6.1: Resistivity-dose schemes for as-received Fe.

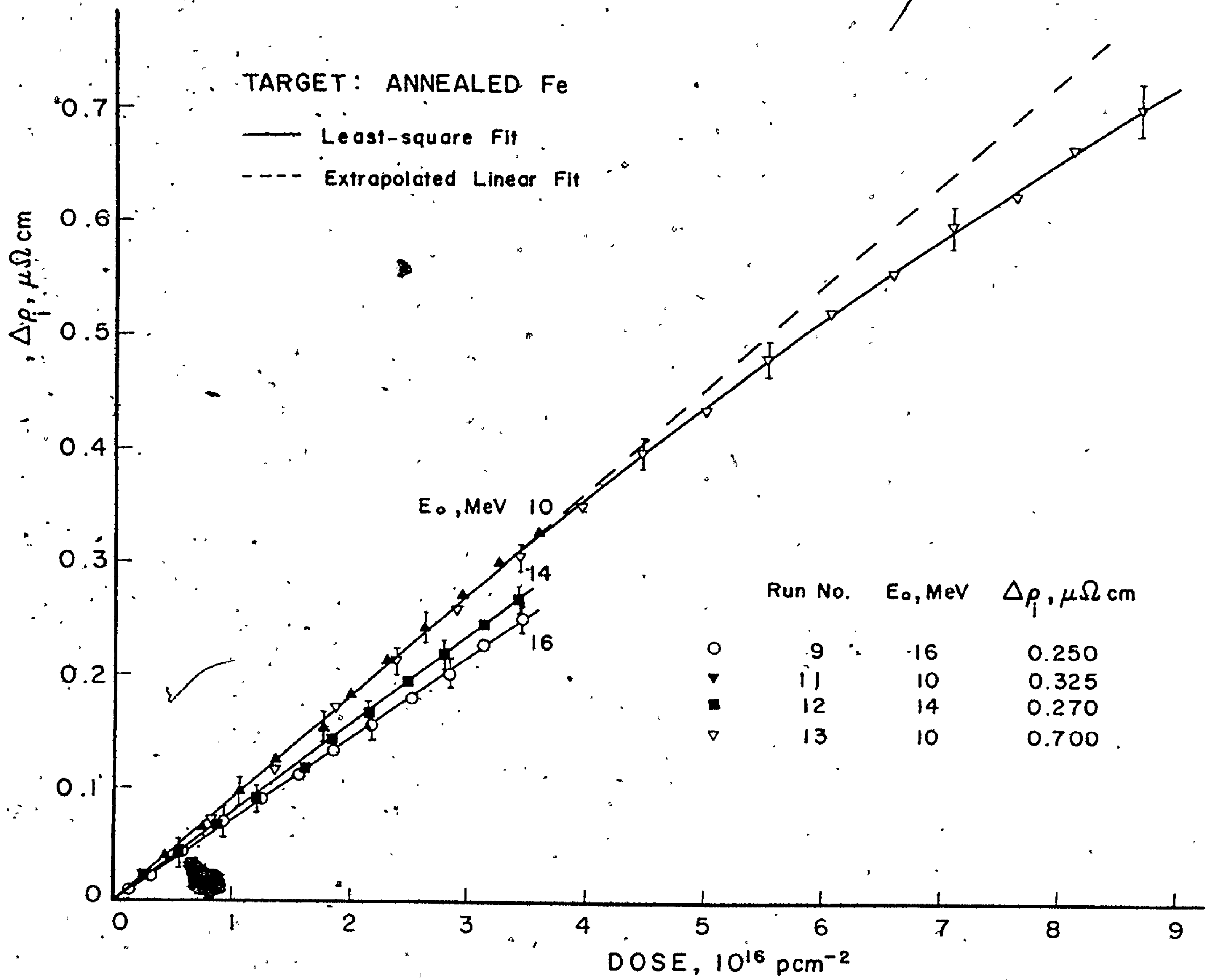

Fig. 6.2: Resistivity-dose schemes for annealed Fe.

mental data is substantially scattered around a linear least-square fit. This data-scattering is due to a statistical error of 2.0% on the average in the resistance measurements. Above a dose of 2×10^{16} p cm^{-2}, the error is less than 0.5%. The error bars represent the summation of this statistical error and an error of 2.5% due to the uncertainty associated with the measurements of the irradiated lengths.

6.1.2 Zirconium

As was stated in section 5.1, annealed Zr samples could not be obtained. Thus, only as-received specimens were employed. A beam of protons with an energy of 10 or 16 MeV was used. An integrated dose of approximately 3.6×10^{16} p cm^{-2} was reached in all the runs except the last in which a dose of 7.7×10^{16} p cm^{-2} was employed. The resulting resistivity change varied from 0.881 to 1.866 μΩ cm as summarized in Table 6-1.

The resistivity-dose curves are shown in Fig. 6.3. Both of the experimental data and the least-square fit are displayed. The scattering of the experimental data around the linear fit below a dose of 1.5×10^{16} p cm^{-2} is due to an error of 1.5% in reading the absolute resistance in the low-dose region. Addition of such an error to another error of 2.5%, resulting from irradiated-length measurements, yields the error bars shown in Fig. 6.3.

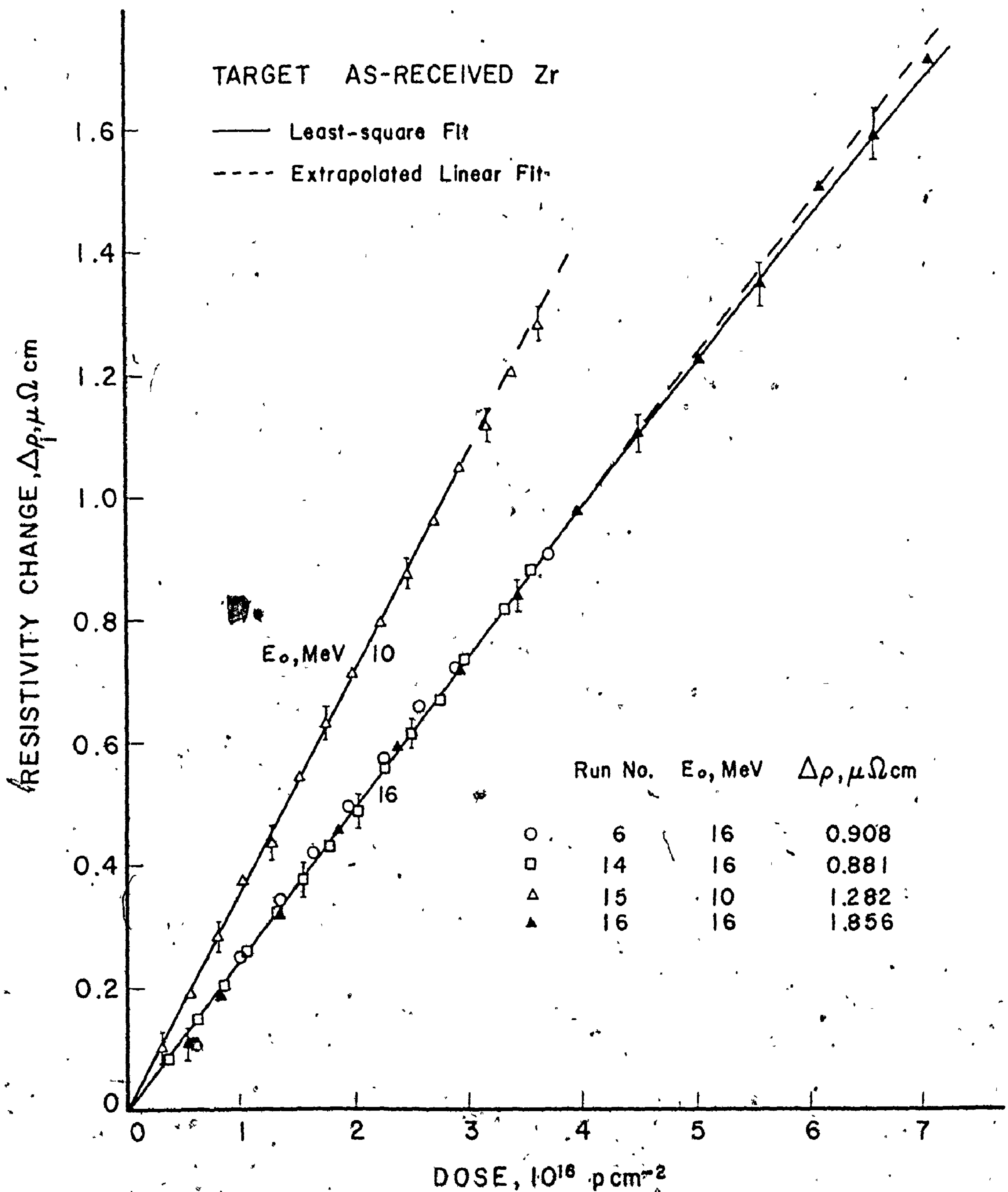
TARGET AS-RECEIVED Zr
Least-square Fit
Extrapolated Linear Fit
RESISTIVITY CHANGE, $\Delta\rho_i, \mu\Omega$ cm
DOSE, 10^{16} p cm^{-2}
E_o, MeV 10
16
Run No. E_o, MeV $\Delta\rho, \mu\Omega$cm
○ 6 16 0.908
□ 14 16 0.881
△ 15 10 1.282
▲ 16 16 1.856
0
0.2
0.4
0.6
0.8
1.0
1.2
1.4
1.6
0
1
2
3
4
5
6
7

6.1.3 Copper

An annealed sample was irradiated with a total dose of 2.0×10^{16} p cm^{-2}. This yielded a total resistivity change of 18.53 nΩ cm. The resistivity change as a function of dose is displayed in Fig. 6.4. An error of 2.5% exists in the measurements of the absolute resistance of the sample. The error bars shown in Fig. 6.4 include this error and an error of 2.5% in measuring the irradiated length.

In Fig. 6.4, the result of Roberto et al.[105] for d-Be neutron irradiation of a similar Cu sample at 4.2K is also displayed. Dworschak et al.[125] irradiated a Cu sample with a 10 MeV proton beam at 80K. At a dose level of 1×10^{17} p cm^{-2}, they observed a resistivity change of 74.0 nΩ cm. Since about 60% of the damage induced in Cu at 17.5K by a 16 MeV proton beam is recovered at 70K (see section 7.3), and since an excess of 63% in $d\Delta\rho_i/d\phi t$ is observed in the present work (for 16 MeV proton irradiated as-received Fe at 17.5K) over that observed previously[22] when a similar iron sample was irradiated by 16 MeV protons at 68K, the resistivity change observed at 80K by Dworschak et al. can be multiplied by 1.6 to determine the value that would have been observed at 17.5K. Such a modified result is displayed in Fig. 6.4.

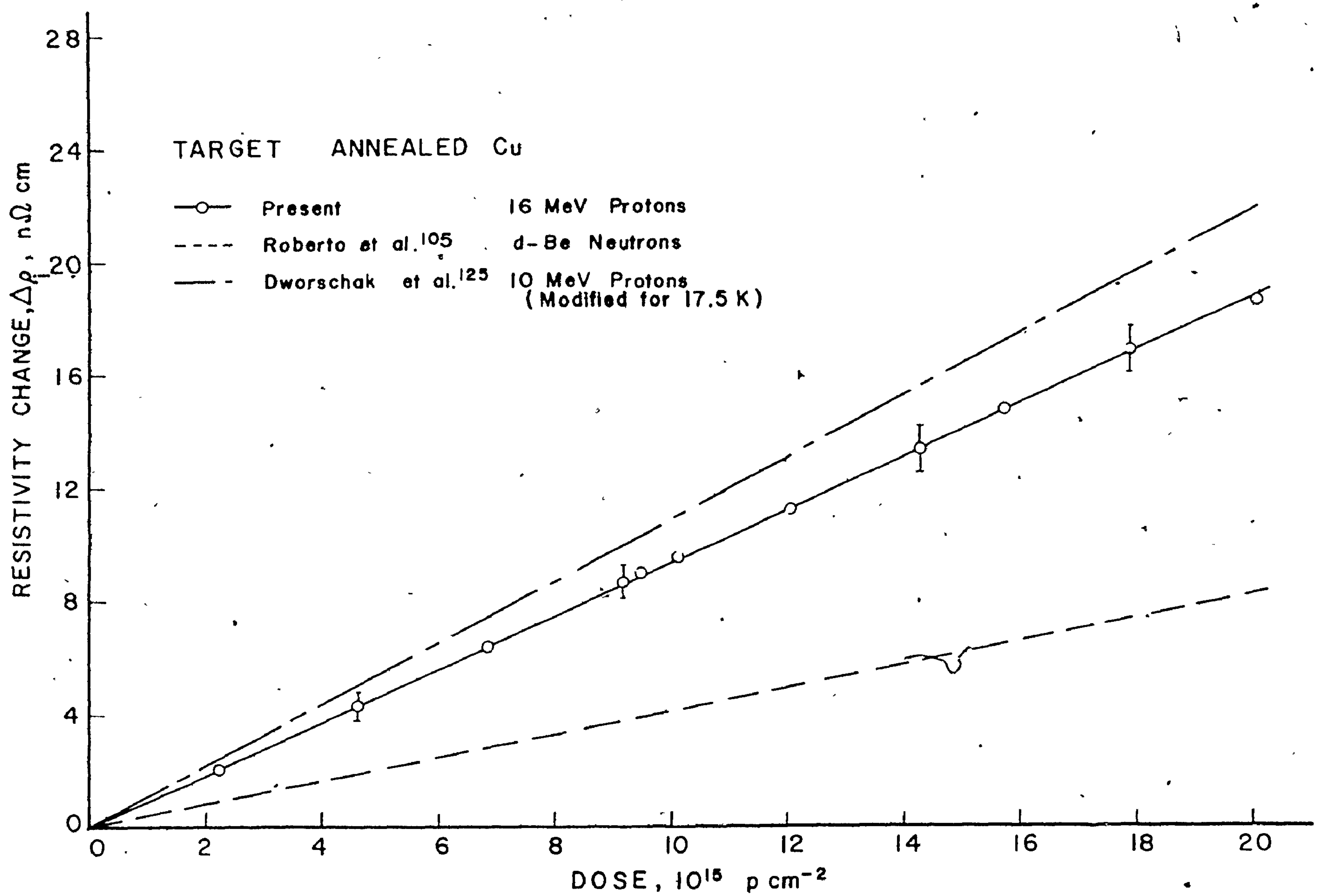

Fig. 6.4: Resistivity-dose schemes for annealed Cu.

6.2 Discussion

As can be seen from Figs. 6.1 to 6.4, for low doses $\Delta\rho_i$ varies linearly with the fluence. This is in agreement with results reported by Minier-Cassayre[106] for fast neutron-irradiation (> 1.0 MeV) at 20K of zone-refined annealed Fe, and with previous 16 MeV proton irradiation of as-received Fe undertaken at 68K[22]. A least-square fit of the form

$$\Delta\rho_i = a + b(\text{dose}) \tag{6.1}$$

was made for low doses ($\leq 4.0 \times 10^{16}$ p cm^{-2}). A boundary condition was imposed on the fitted line to yield a value of zero for the intercept a. Deviation from linearity was observed for fluences greater than 3.0×10^{16} to 4.0×10^{16} p cm^{-2} independent of either the sample pre-irradiated conditions or the value of the bombarding energy. Two general features were observed from the experimental data: i) The rate of resistivity change with dose is higher for the as-received samples than the annealed cases, and ii) the rate of resistivity change is highest for the lowest incident energy. In Eq. 6.1, the parameter b represents the resistivity-damage rate $d\Delta\rho_i/d\phi t$. Values for b are determined for each irradiation case and then used in the summary analysis presented in Chapter 8.

CHAPTER 7

ANNEAL MEASUREMENTS

7.1 Results for Iron

7.1.1 Experimental observations

Post-irradiation isochronal annealing was carried out for three stacks of as-received and annealed samples. Each stack was separately irradiated by 10, 14 or 16 MeV protons. The bombarding dose was kept constant at approximately 3.8×10^{16} p cm^{-2}. The isochronal annealing was carried out from 20 to 160K in steps 5K apart and 10 minutes in duration.

The percentage recovery data as a function of the anneal temperature is presented in Figs. 7.1 and 7.2 for as-received and annealed samples. The corresponding differential recovery schemes are shown in Figs. 7.3 and 7.4. Several substages in stage I recovery are observed. These substages are selected using notation published in the literature[67,95,106,108,114-117]. Table 7-1 summarizes the present recovery results. Some of the published work for electron and neutron irradiated iron are found in Table 7-2.

The recovery schemes of Figs. 7.1 and 7.2 show that as-received samples exhibit approximately 3% less recovery than the recovery observed in annealed specimens. This feature is observed independent of the value of the incident energy.

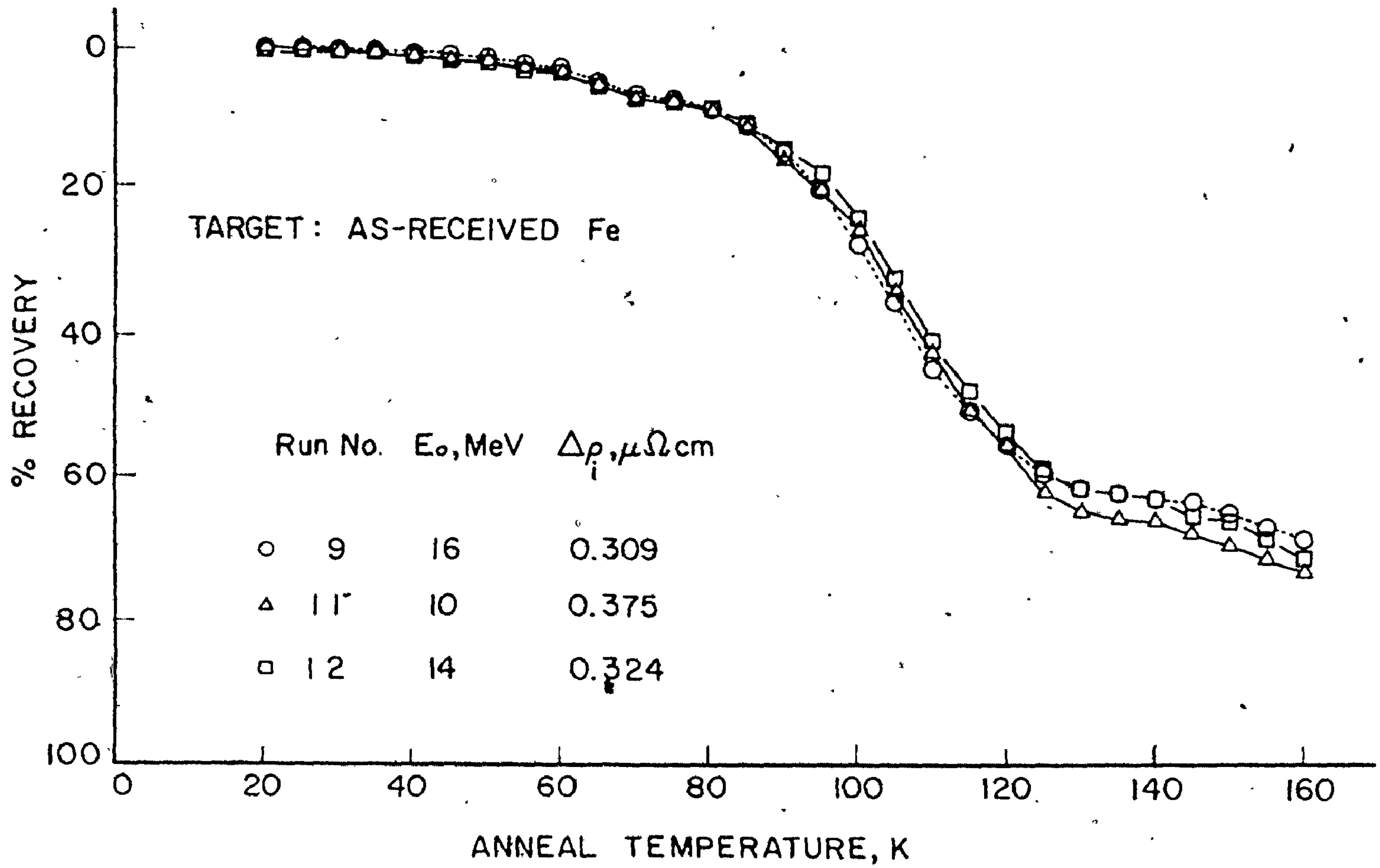

Fig. 7.1: Percent recovery change with annealing temperature for as-received Fe.

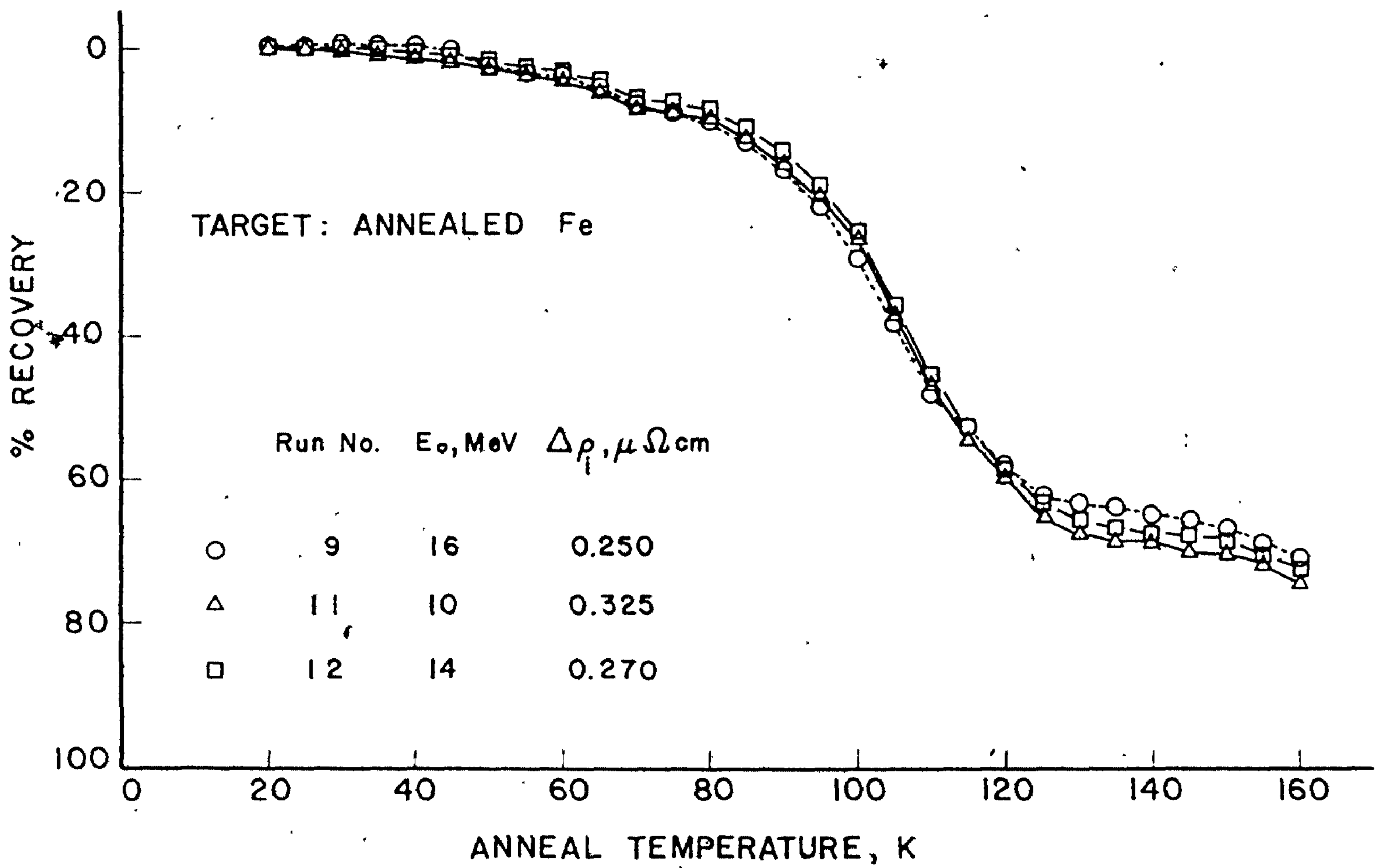

Fig. 7.2: Percent recovery change with annealing temperature for annealed Fe.

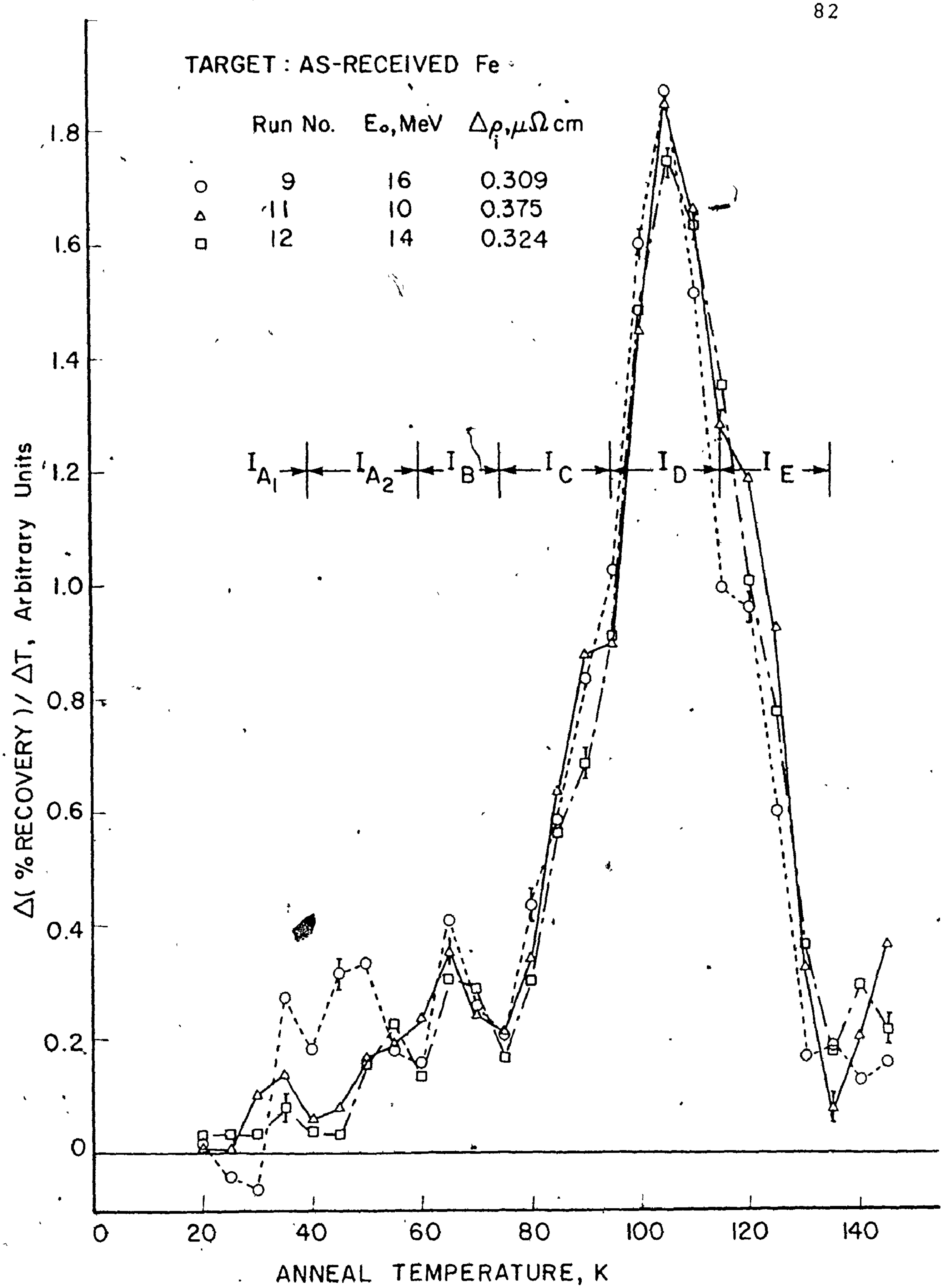
TARGET : AS-RECEIVED Fe
Run No. E₀,MeV Δρ_i,μΩ cm
9 16 0.309
11 10 0.375
12 14 0.324
I_A1 I_A2 I_B I_C I_D I_E
Δ(% RECOVERY)/ ΔT, Arbitrary Units
1.8
1.6
1.4
1.2
1.0
0.8
0.6
0.4
0.2
0
0
20
40
60
80
100
120
140
ANNEAL TEMPERATURE, K

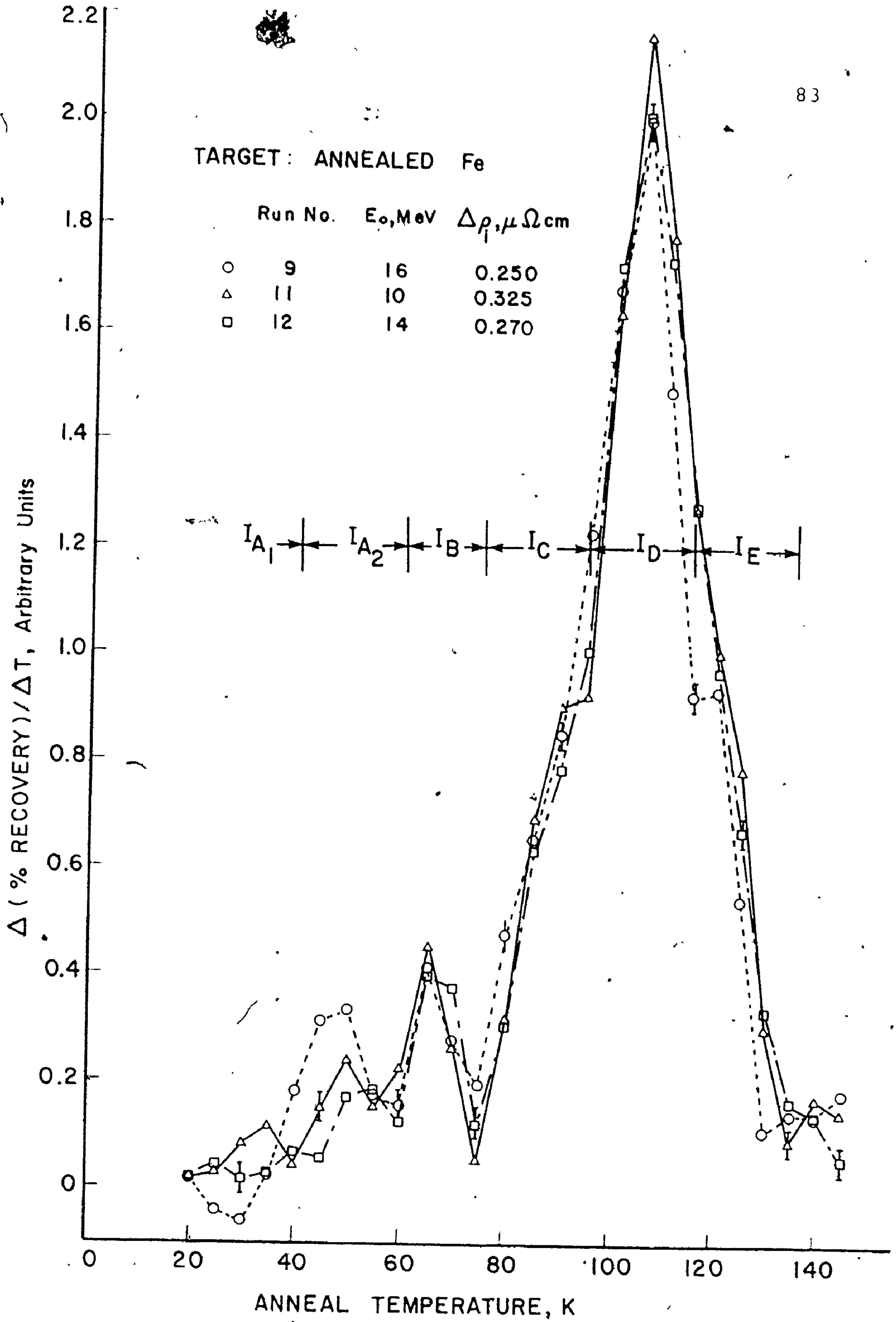
TARGET: ANNEALED Fe
Run No. E₀,MeV Δρ_I,μΩcm
○ 9 16 0.250
△ 11 10 0.325
□ 12 14 0.270
I_A1 I_A2 I_B I_C I_D I_E
Δ (% RECOVERY)/ΔT, Arbitrary Units
ANNEAL TEMPERATURE, K
0
0.2
0.4
0.6
0.8
1.0
1.2
1.4
1.6
1.8
2.0
2.2
20
40
60
80
100
120
140

Table 7-1 Summary of the present recovery results for as-received and annealed Fe

E_o, MeV		16				14				10			
Substage	Range, K	As-received T_s†, K	% Rec.	Annealed T_s, K	% Rec.	As-received T_s, K	% Rec.	Annealed T_s, K	% Rec.	As-received T_s, K	% Rec.	Annealed T_s, K	% Rec.
I_{A_1}	40 <	35	0.4	Not observed		35	1.2	40	1.0	35	1.0	35	1.3
I_{A_2}	40–60	50	2.5	50	4.2	55	2.6	53	2.3	50**	2.8	50	3.2
I_B	60–75	65	4.2	65	4.3	65	3.7	67	4.5	65	4.0	65	4.3
I_C	75–95	105 (I_C–I_D)	43.6	105 (I_C–I_D)	44.8	105 (I_C–I_E)	55.2	87*	11.4	90*	12.2	90*	12.2
I_D	95–115							105 (I_D–I_E)	47.2	105	30.6	105 (I_D–I_E)	47.6
I_E	115–135	120*	11.5	120*	10.6					120*	15.4		
Total % Recovery for Stage I			62.2		63.9		62.7		66.4		66.0		68.6

*Appeared as a shoulder to substage I_D

**Appeared as a shoulder to substage I_B

†T_s is the temperature at which a substage-peak is observed.

Table 7-2: Published data for electron and neutron irradiated Fe.

Reference nnealing range, K ncident Particle E_o, MeV		114 4.2-400 e^- 1.3		95 40-140 e^- 1.5		116 4.5-500 n^o >0.1		108 4.6-500 n^o >0.1		106 >20-500 n^o >1.0		Recovery mechanisms
tage	Substage	T_s, K	% Rec.	T_s, K	% Rec.	T_s, K	% Rec.	T_s, K	% Rec.	T_s, K	% Rec.	
	I_{A_1}	39	0.8	not observed								a
	I_{A_2}	51	3.2	51	3.5				3.0		2.0	a
	I_B	66	7.0	66	15.0	112	42.0					a
	I_C	87	20.5	87	18.5							a
I	I_D	100	47.0	99	34.0			110	34.0	103	39.0	b
	I_E	128	6.5	105-120	11.0							c
	Total		85.0		82.0		42.0		37.0		41.0	

Continued .../

Table 7-2 continued

tage	Substage	T_s,K	% Rec.	T_s,K	% Rec.	T_s,K	% Rec.	T_s,K	% Rec.	T_s,K	% Rec.	Mecha- nisms
II	II_A	165	9.0			168	33.0	140-330	38.0	137-207	17.0	d,e,or f
	II_B	223				250				207-273	17.0	e or g
III		340	2.0			320	15.0			273-323	2.5	h
IV						>417	5.0			323-473	18.5	g
V										>473		ı

) Annihilation of close Frenkel pairs.
) Long-range migration of interstitials to correlated vacancies.
) Random migration of interstitials to sinks.
Annihilation by crowdian motion[106].
Interstitial trapping by impurities[95,114,116].
Dissociation of interstitial clusters[108].
Migration of interstitial groups[106].
Migration of single vacancies, trapping of interstitial impurities.
Self diffusion.
T_s is the temperature at which a substage-peak is observed

7.1.2 Previous experiments

Clearly distinguishable substages have been observed in a number of electron irradiation studies of iron. In a 1.5 MeV electron irradiation experiment at 40K of ι-iron, Wells and Russell[95] observed five substages in stage I recovery. Three of these substages, labelled I_A, I_B and I_C, appeared at 51K, 66K and 87K with 3.5%, 15% and 18.5% recovery respectively. These peaks were attributed to annihilation of close V-I pairs. In addition, they observed a large substage, I_D, peaking at 99K and accounting for 34% of the total recovery. They assigned long range migration of interstitials to correlated sinks to I_D, with an activation energy of 0.23 eV. An I_E-substage appeared as a shoulder to I_D at a temperature range of 110K to 135K with 11% recovery. They attributed it to random migration of interstitials. They reported that the amount of recovery observed in substage I_E, as well as the total recovery found in stage I, were significantly reduced either by increasing the dislocation density or by reducing the grain size. They proposed interstitial trapping at dislocations as a possible mechanism for I_E recovery. In a separate study, Neely and Keefer[114] reported the presence of a low-temperature substage at 39K accounting for 0.8% of the total recovery after electron irradiation of as-received iron samples at 4.2K. Their substages I_C through I_E accounted for 74% of the total recovery observed. Also, a 21K substage was observed by Sao and Meshii[115] in iron irradiated with 1 MeV electrons.

In contrast to the electron bombardment studies, smearing of substages I_C through I_E is a common feature observed in fast-neutron irradiation experiments. Horak and Blewitt[116] reported a 34% recovery due to a dominant substage between 80K and 140K. Below 80K, they observed less than 5% recovery. A 3% recovery below 80K was observed by Nakagawa et al.[108] One peak centered at 110K was also found in their work and it accounted for 34% of the total recovery after a fission-reactor irradiation. In another study, two distinct peaks were observed at 95K and 110K by Takamura et al.[117] in a low-dose fast-neutron irradiated iron sample. Also, Minier-Cassayre[106] observed a large peak at 103K. Her sample was a zone-refined iron irradiated by fast neutrons. She attributed this peak to interstitial recovery by several mechanisms.

7.1.3 Discussion

In the present work, ~~les~~ less than 7.3% of the induced damage anneals out in two substages, I_{A_1} and I_{A_2}, observed below 60K. Another low-temperature substage, I_B, appears at 65K. It amounts to 7% of the total recovery. The percent-recovery observed below 75K is found to be independent of either the samples pre-irridiation condition or the incident proton energy. It is well established[95,114,115] that I_{A_1} through I_C substages are attributed to close V-I pairs. In some cases, interstitials need only two to three jumps to reach their annihilation sinks (the 65K substage)[118]. The present observations support that annihilation of close V-I pairs is a possible recovery mechanism for the early substages since the amount of recovery below 75K is insensitive to the dislocation density. A dominant substage, I_D, is observed at 105K in all the runs. It has low- and high-temperature shoulders forming substanges I_C and I_E respectively. The percentage recovery observed in $I_C + I_D + I_E$ is between 54.1% to 59.8% of the total recovery. This depends on both the sample pre-irradiation conditions and the value of the incident proton-energy. In the temperature range of 115 to 135K, a slightly higher percentage recovery is observed for annealed specimens over the recovery resulting from as-received targets. Recovery in the substage I_D is believed to be due to migration of interstitials to correlated vacancy sites[95,108]. A migrating interstitial in such a substage experiences a number of jumps before reaching a sink. As proposed by Minier-Cassayre[106] such interstitials may recover by recombining with vacancies or by aggregating with one or more interstitials to form cluster nuclei. This is probably the case in the present work since no difference is observed between the recovery schemes of the as-received and the annealed samples.

Examination of the shape and the percentage recovery of the dominant 105K peak with its low- and high-temperature shoulders leads to the following conclusions: i) the damage states created in iron are relatively similar for incident energies between 10 and 16 MeV, ii) the damage states are not sensitive to the dislocation density existing in the test samples, and iii) the damage state is similar to an intermediate state between those due to fast-neutron and electron irradiations.

7.2 Results for Zirconium

7.2.1 Experimental data

Isochronal annealing was carried out from 20K to 170K. The annealing steps were 5K apart and 10 minutes in duration. The percentage recovery as a function of the annealing temperature is displayed in Fig. 7.5. The differentials of these recovery schemes are shown in Fig. 7.6. The ranges assigned for the substages in stage I recovery are from electron irradiation studies[109,119] and from fast-neutron bombardments.[110,111] In the present work we find that such regions are as shown in Fig. 7.5.

Substage I_A is not resolved in the present study. Despite the experimental errors associated with the low-temperature substages, few peaks are observed in this region.

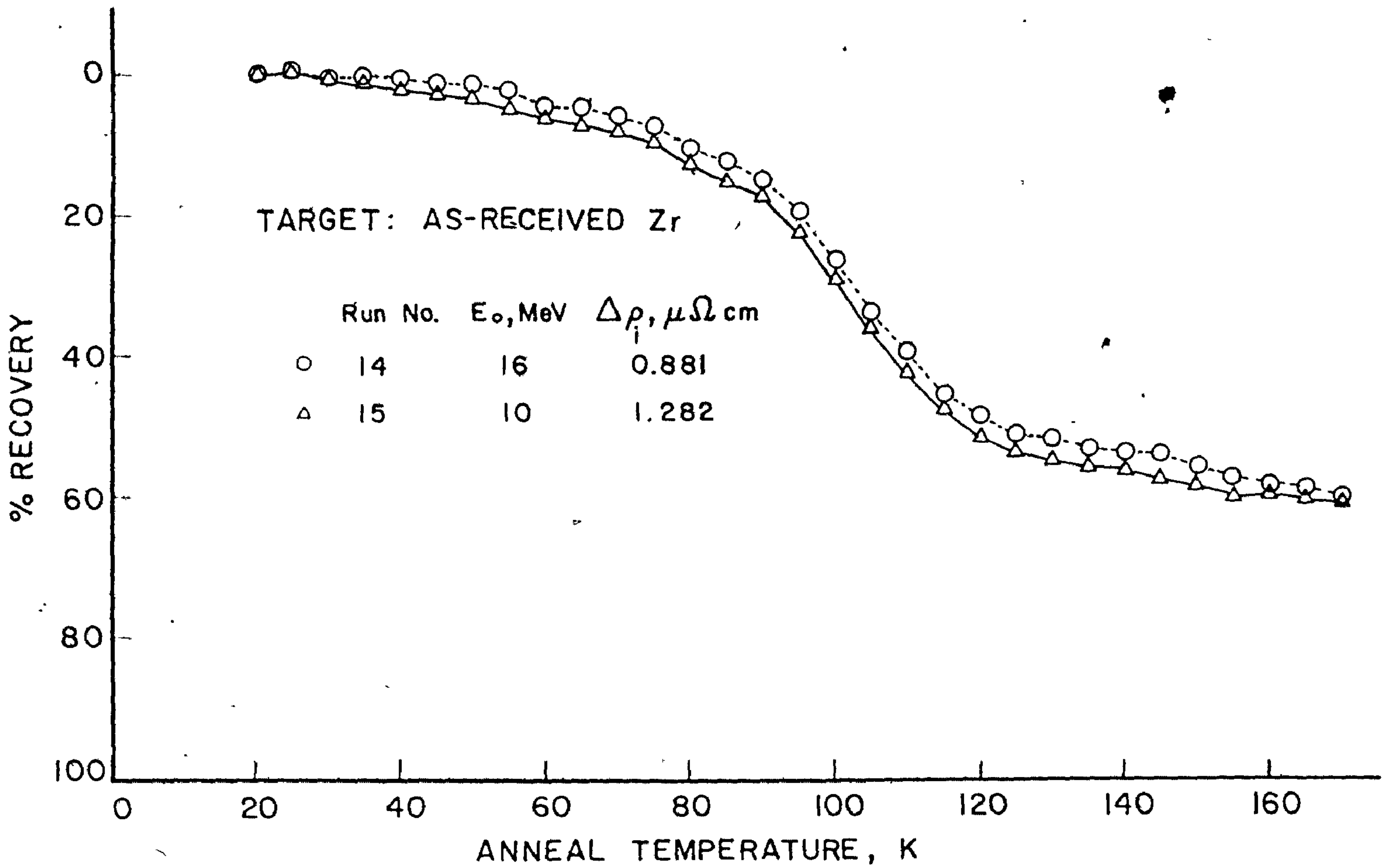

Fig. 7.5: Percent recovery change with annealing temperature for as-received Zr.

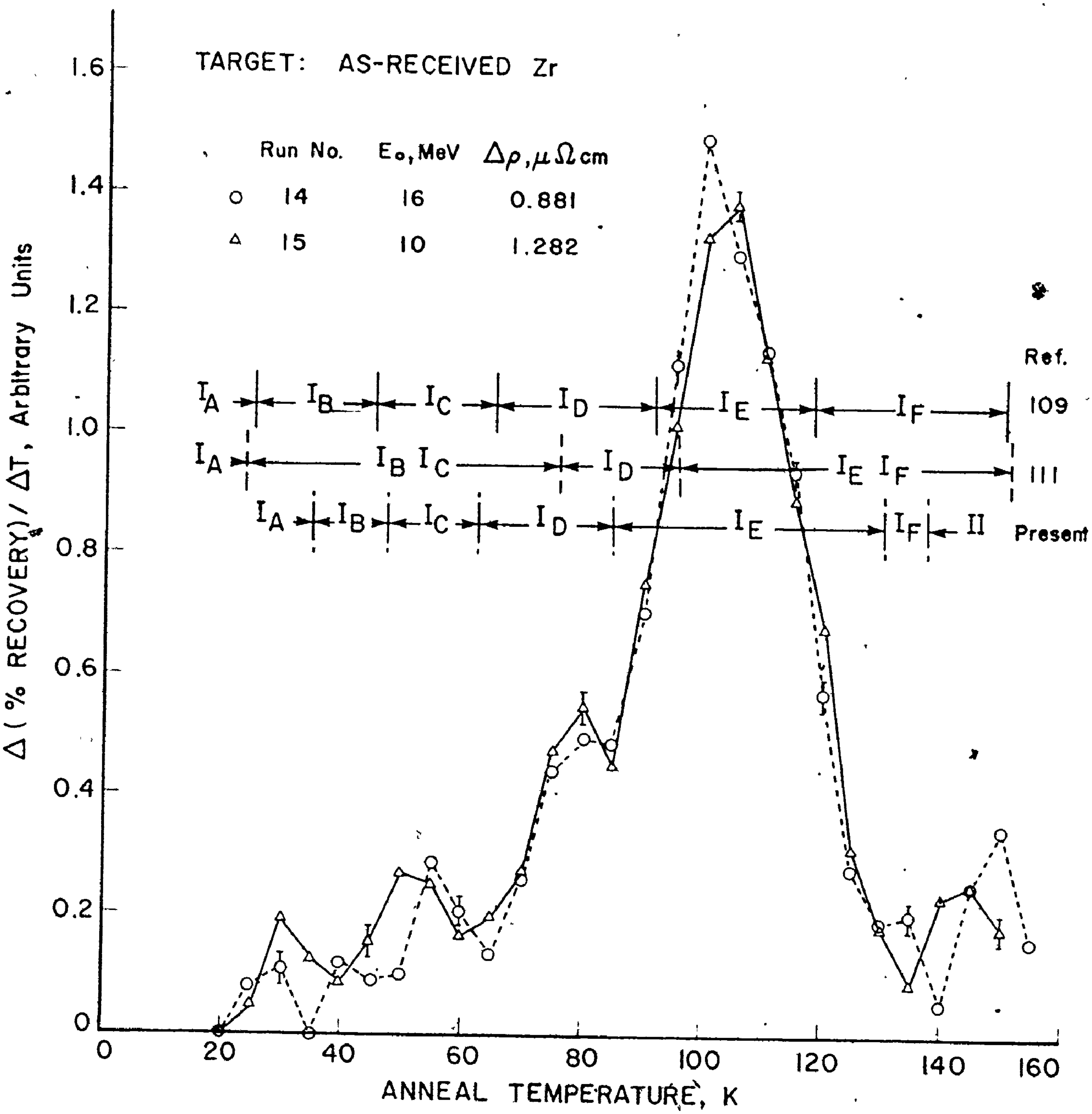

TARGET: AS-RECEIVED Zr
Run No. E₀,MeV $\Delta\rho, \mu\Omega$cm
○ 14 16 0.881
△ 15 10 1.282
Ref.
I_A I_B I_C I_D I_E I_F 109
I_A I_B I_C I_D I_E I_F 111
I_A I_B I_C I_D I_E I_F II Present
Δ (% RECOVERY) / ΔT, Arbitrary Units
ANNEAL TEMPERATURE, K
0
20
40
60
80
100
120
140
160
0
0.2
0.4
0.6
0.8
1.0
1.2
1.4
1.6

Fig. 7.6

For 16 MeV irradiation substages I_B and I_C are seen at 40K and 55K respectively. However, this is not the case for 10 MeV irradiation where these two substages overlap. Substage I_D appears as a low-temperature shoulder to I_E. It is more pronounced for lower energy irradiation. The dominant recovery substage I_E appears in the range of 85 to 130K. It is centered between 100 and 105K. For 10 MeV irradiation I_F is not observed and stage II starts at 135K. In the case of 16 MeV irradiation, I_F is observed as a high-temperature shoulder to I_E and this impedes the start of Stage II up to a temperature of 145K. The peaks observed above 140K are likely due to the deformation[111] of the wire samples during preparation and winding onto the sample-sheet. A summary of the present recovery data is included in Table 7-3 while Table 7-4 lists published work on electron and neutron irradiated Zr.

7.2.2 Discussion

In a 1.5 MeV electron irradiation study carried out near 8K by Neely[109], six substages in stage I recovery of Zr were observed. These were centered at 15, 35, 56, 81, 102.5 and 132.5K respectively from I_A to I_F. The corresponding percentage recoveries were 5, 4, 4.5, 12.5, 31.5 and 18%. Biget et al.[119] used a beam of 1.7 MeV electrons to irradiate a Zr sample. They could not resolve the two substages I_E and I_F. As for the other substages, they were observed at

Table 7-3: Summary of the present recovery results for as-received Zr

E_o, MeV		16		10	
Substage	Range, K	$T_s{}^*$, K	% Rec.	T_s, K	% Rec.
I_A	35 <	20-35	<0.5	20-35	<1.6
I_B	35-47.5	40	1.2	52	5.0
I_C	47.5-62.5	55	2.9		
I_D	62.5-85	80	7.8	80	8.7
I_E	85-130	102	39.8	103	39.9
I_F	130-137.5	135	1.6	not observed	
Total % recovery for Stage I			53.8		55.2

* T_s is the temperature at which a substage-peak is observed.

able 7-4 Published data for electron and neutron irradiated Zr

Reference Annealing range, K Incident Particle E_o, MeV		109 8-310 e^- 1.5		119 4.2-150 e^- 1.7		111 24-500 n^o >1.0		110 77-300 n^o >1.0		Recovery mechanisms
Stage	Substage	T_s^*, K	% Rec.	T_s, K	% Rec.	T_s, K	% Rec.	T_s, K	% Rec.	
I	I_A	15	5.0	15	8.0	not observed				a
	I_B	35	4.0	35	5.0	66	5.7	not observed		a
	I_C	56	4.5	56	5.5					a
	I_D	81	12.5	81	14.5	85	4.5			a or b
	I_E	102.5	31.5	102.5	44.5	116	28.2	120	30.0	c or d
	I_F	132.5	18.0	132.5						d or c
	Total		75.5		77.5		38.4		30.0	

Continued .../

Table 7-4 Continued

Stage	Substage	T_s,K	% Rec	T_s,K	T_s,K	% Rec.	T_s,K	% Rec.	Mechanisms
II		175	5.5		176	10.3	130-250		e or f
III		280	15.0		235	31.7	250-300		g or h

Annihilation of close Frenkel-pairs.
Long-range migration of interstitials to correlated vacancies.
Random migration of interstitials to vacancies[109,119].
Random migration of interstitials to form cluster nuclei with similar defects[110,111]
Mobility or dissociation of small aggregates of interstitials[111].
Release of interstitials from impurities[109,119,110].
Second type of interstitial moving[109,119,110].
Undecided[111].
T_s is the temperature at which a substage-peak is observed.

the same temperatures reported previously by Neely.

When Zr was bombarded at 24K with fast-neutrons, Vialaret et al.[111] could not observe substage I_A. Their I_B and I_C substages were smeared in one peak centered at 65K and amounted to 5.7% of the total recovery. Their I_D substage accounted for 4.5% of the total recovery and appeared at 85K. The higher-temperature substages I_E and I_F could not be resolved. They were smeared in a dominant peak at 116K and showed 28.2% recovery. Therefore, they reported only 38.4% recovery for stage I. This is lower than the 75.5% recovery reported by Neely[109] and the 77.5% recovery observed by Biget et al.[119], in their corresponding electron-irradiation experiments. This reduction in stage I recovery has been reported previously by Rosenbaum et al.[110] who observed 30% recovery in a single substage extending between 110 and 130K. They irradiated, however, their Zr sample at 77K..

In the present result, 10-MeV proton bombardment shows 3.2% more recovery than the recovery observed for the case of 16-MeV proton irradiation. It is mostly observed in substages I_B through I_D where close V-I pair annihilation is assumed as the mechanism for damage recovery.[109,119] The dominant I_E peak accounts for approximately 39.5% of the total recovery regardless of the bombarding energy.

The results of the present work suggest that the damage state produced by protons in Zr is similar to an intermediate state between those created by fast-neutron and electrom bombardments.

7.3 Results for Copper

7.3.1 Experimental data

Isochronal recovery was carried out for 5 minutes at each annealing level. The temperature spacing was 1.5K between 20 and 30K, 2K between 30 and 40K, 2.5K between 40 and 50K and 3K between 50 and 60K. This scheme was adopted previously by Roberto et al.[104]

The observed percentage recovery as a function of the annealing temperature is shown in Fig. 7.7. The corresponding differential recovery is displayed in Fig. 7.8. No measurements are recorded below 20K since the change in $\Delta\rho$ was too small to be resolved. Four substages are observed, I_B, I_C, I_D and I_E. The substage I_B is clearly observed at 27.5K and it accounts for 7.5% of the total recovery. The dominant peak appearing at 40K has low- and high-temperature shoulders forming the I_C and I_E substages respectively. The recovery scheme is in good agreement with published results for Cu irradiated by electrons[126] or by neutrons[104,121]. A summary of present and published data is presented in Table 7-5.

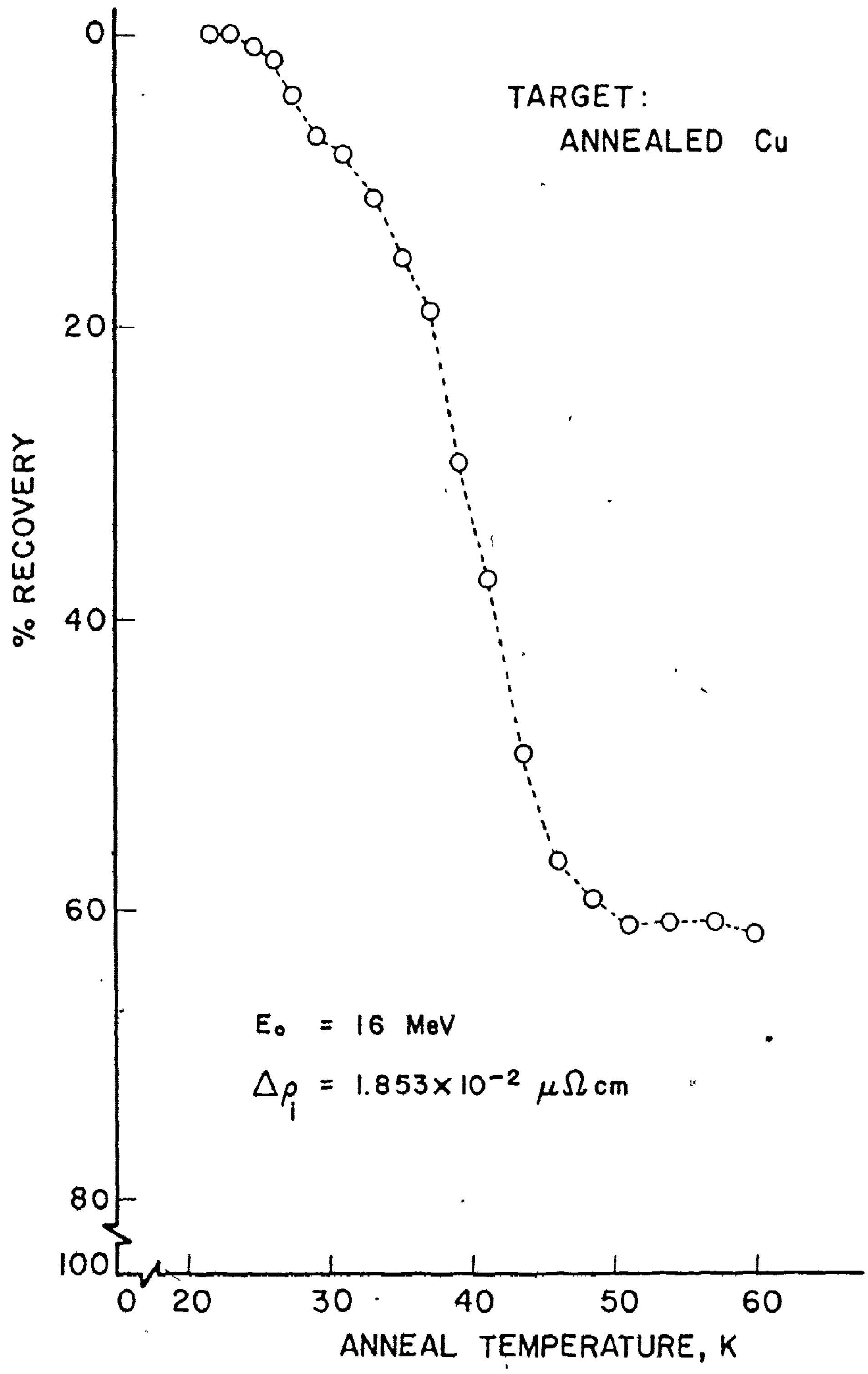

Fig. 7.7: Percent recovery change with annealing temperature for annealed Cu.

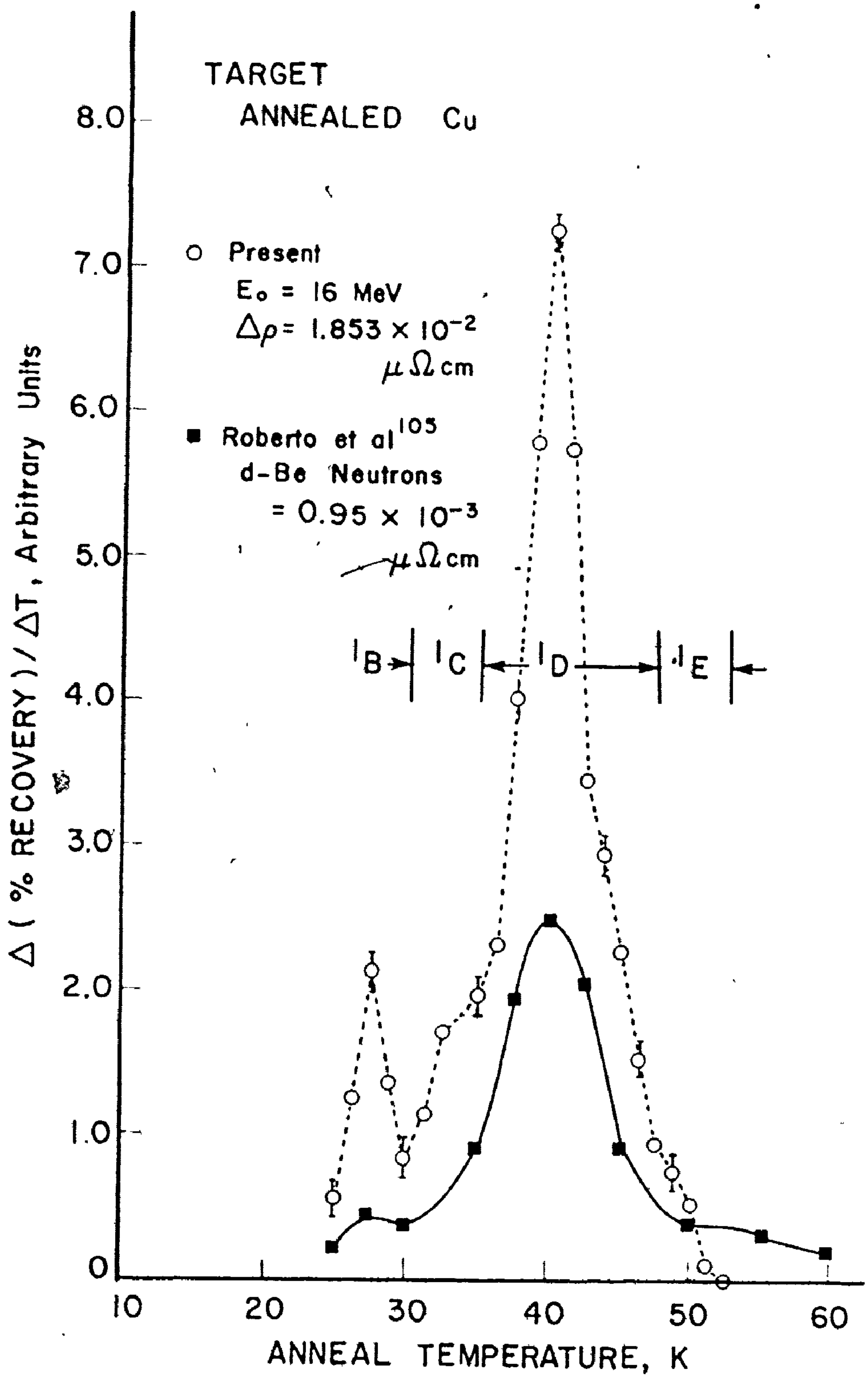

Fig. 7.8: Differential recovery schemes for annealed Cu.

Table 7-5: Present and published recovery data for Cu

Reference Annealing range K Incident Particle E_o, MeV		Present 17.5-70 p 16		126 4.2-70 e^- 1.4		116 4.6-500 n^o >1.0		104 8-400 n^o d-Be spectrum		Reco- very mecha- nisms
Stage	Substage	T_s^*,K	% Rec.	T_s,K	% Rec	T_s,K	% Rec	T_s,K	% Rec	
	I_A	not observed		14-24	2.5					a
	I_B	27.5	7.6	24-28.5	13.1					a
I	I_C	32.5	6.6	28.5-33	10.0	43	33.0	8-65	36.0	a
	I_D	40	43.8	33-48	48.8					b
	I_E	-	2.8	48-65	12.8					c
	Total		60.8		87.2		33.0		36.0	

Table 7-5 (continued)

Stage	Substage	T_s,K	% Rec.	T_s,K	% Rec.	T_s,K	% Rec.	T_s,K	% Rec.	T_s,K	% Rec.	Recovery Mechanisms
II								-	13.0			,d
III								147-300	38.0			-
IV								not observed				
V								490	9.0			

a) Annihilation of close Frenkel pairs.
b) Long range migration of interstitials to correlated vacancies.
c) Long-range dose-dependent interstitial migration.
d) Impurity dependent recovery.
* T_s is the temperature at which a substage-peak is observed.

7.3.2 Discussion

Roberto et al.[104] recently observed that irradiation of Cu by d-Be neutrons gives similar recovery schemes to those obtained after fast neutron irradiation[121]. They concluded that the damage state created in both cases is similar.

In the present result, we find that proton irradiation produces a damage state similar to that obtained by d-Be neutron irradiation[104]. However, more recovery is observed in the present work at substage I_B over the corresponding recovery reported in the d-Be irradiation case as can be seen from Fig. 7.8.

CHAPTER 8

SUMMARY ANALYSIS

This chapter contains a summary analysis of the data presented in Chapters 4, 6 and 7. A comparison between the experimental data of the resistivity damage rate and theoretical estimates based on the damage parameters is presented in section 8.1. The damage state created by 16 MeV protons is analysed in section 8.2 in terms of the corresponding damage states due to electron and fast-neutron bombardments. Finally, section 8.3 includes a discussion of the relation of the present proton recovery data to fusion-neutron spectra.

8.1 Comparison of the Experimental and Theoretical Data of the Resistivity-Damage Rate

Experimental values of the resistivity damage rate were determined from the plots which exhibit $\Delta\rho_i$ as a function of dose (Chapter 6). The slopes of the linear part of such plots give values for the corresponding $d\Delta\rho_i/d\phi t$.

The resistivity damage rates were also calculated using the theoretical data of Chapter 4. This was carried out using a modified Kinchin-Pease model and a vacancy-recombination model. In the modified Kinchin-Pease model, spontaneous recombination is not considered and only V-I pairs are dealt with. According to Eq. 2.18, the resistivity damage rate can be expressed as

$$d\Delta\rho_i/d\phi t = 10^{-25} \frac{\kappa\ E_D}{2\ E_d} \Delta\rho_{FP} , \qquad 8.1$$

where E_D is in barn-keV, E_d in eV and $\Delta\rho_{FP}$ in $\mu\Omega$ cm/at.%. The vacancy-recombination model, described in section 2.2, was also used to calculate values for $d\Delta\rho_i/d\phi t$. For this purpose, Eq. 2.20 was used to develop the form

$$d\Delta\rho_i/d\phi t = \Delta\rho_{FP} \cdot \int_{25\ eV}^{E^r_{max}} \frac{\sigma_D}{\alpha(v_r)+\beta(v_r)(E^r\cdot\eta_D)} dE^r . \qquad 8.2$$

To carry out such an integration, values for α and β were taken from the literature. Values for σ_D and E^r were obtained from the data of Chapter 4 while η_D was calculated using Eq. 2.14. The semi-empirical formula of Norgett et al.[54] which is developed only for iron, Eq. 2.21, was also modified to yield

$$d\Delta\rho_i/d\phi t = 10^{-27} E_D\ \Delta\rho_{FP} , \qquad 8.3$$

where E_D is in barn-keV and $\Delta\rho_{FP}$ in $\mu\Omega$ cm/at.%.

For the case of iron, values of E_D were interpolated from Table 4-3 for 10, 14 and 16 MeV protons. A value of 25 eV[67] was assigned for E_d while $\Delta\rho_{FP}$ was taken as 19 $\mu\Omega$cm/at.%[69]. Table 4-6 was used to obtain values of E_D for Zr.

Values for $E_d = 24$ eV[109] and $\Delta\rho_{FP} = 40$ μΩ cm/at.%[112] were assigned for calculations. For Cu, values of $\alpha = 58$ eV and $\beta = 1.3\times10^{-3}$ were taken from the work of Robinson and Torrens[52]. Fig. 4.9 was used to obtain values for σ_D and E^r. A value of $\Delta\rho_{FP} = 1.3$ μΩ cm/at.%[67] was taken. Table 4-5 was used to determine values for E_D.

The experimental $d\Delta\rho_i/d\phi t$ data was determined from Figs. 6.1 and 6.2 for Fe, from Fig. 6.3 for Zr and from Fig. 6.4 for Cu. The theoretical estimates of the resistivity damage rate were obtained from Eq. 8.1 and 8.3 for Fe and from Eq. 8.1 and 8.2 for Cu. For Zr, the vacancy recombination model could not be used since values for α and β could not be found in the literature. Hence, only Eq. 8.1 was used to estimate the theoretical value of $d\Delta\rho_i/d\phi t$ for Zr. The present experimental and theoretical values of the resistivity damage rate are summarized in Table 8-1 for Fe, Zr and Cu.

It is of interest to point out the close agreement shown in Table 8-1 between the experimental results and the theoretical estimates evaluated using the vacancy-recombination model for Fe and Cu. This agreement suggests that recombination of simple defects[107] is occurring for 10-16 MeV proton bombardments.

Another point of interest is shown in the damage-rate plots presented for Fe in Figs. 6.1 and 6.2. Comparison between these two plots shows that as-received tar-

Table 8-1: Resistivity damage rate, in $10^{-24}\ \Omega\ cm^3$/particle, as estimated from theoretical and experimental data for Fe, Zr and Cu.

Element	Energy MeV	Resistivity Damage Rate			
		Experiment		Theory	
		As-received	Annealed	MKP*	VR*
Fe	10	11.0±0.5	9.0±0.4	21.4	12.2
	14	9.0±0.4	8.0±0.4	17.8	1[illegible].1
	16	8.8±0.4	7.1±0.3	17.1	9.8
Zr	10	36±2.0	-	56.8	-
	16	25±1.0	-	45.3	-
Cu	16	-	0.95±0.05	1.36	1.06

* Modified Kinchin-Pease Model, Eq. 8.1

** Vacancy-recombination model, Eqs. 8.2 and 8.3.

gets exhibit higher resistivity damage rates than the corresponding rates observed for annealed cases. Similar results are reported for Fe by other researchers.[108,117,127] In the present study, this phenomenon may be related to the difference in dislocation density which exists in the as-received and annealed specimens (as indicated by the difference in the respective resistivity ratios; Table 6.1).

8.2 Analysis of the Damage State Using the Recovery Data

The experimental percentage recovery observed in the present work as a function of the anneal temperature is displayed in Fig. 8.1 for Fe, Zr and Cu irradiated by 16 MeV protons. Also shown are the respective results reported in the literature for electron[95,109,126] and fast-neutron (> 1.0 MeV)[111,116,117] irradiations.

Electron bombardment introduces isolated simple defects. As the electron energy increases, the probability for two or more point defects to form a cluster increases[109]. Fast-neutrons, on the other hand, produce more complex damage than electrons do. This is due to the fact that PKA's of energy as high as 60-70 keV are generated in fast-neutron irradiation. The cascades created due to such high-energy PKA's comprise simple defects in addition to defect-clusters. This leads to a suppression of stage I recovery in fast-neutron irradiation experiments.

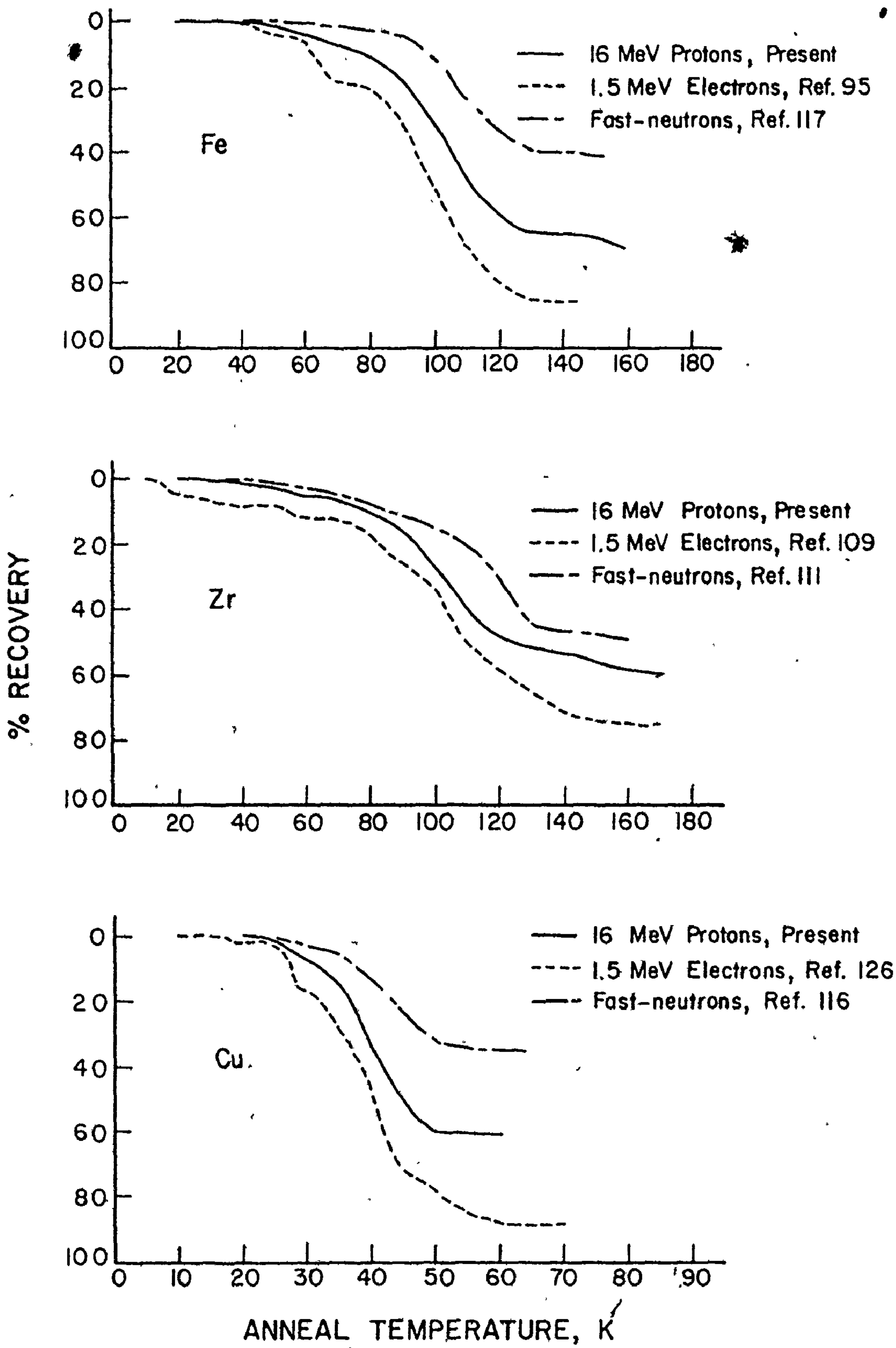

Fig. 8.1: Stage I recovery of Fe, Zr and Cu irradiated by electrons, neutrons and 16 MeV protons.

The presentation shown in Fig. 8.1 indicates that the percentage recovery due to 16 MeV protons is larger than the value due to fast-neutrons, but lower than the value produced by electrons. Therefore, it is possible to say that 16 MeV proton irradiation produces simple-defect structure similar to an intermediate state between the defect configurations created by electrons and fast-neutrons.

8.3 Relation of Proton Data to Fusion-Neutron Spectra

A d-Be spectrum contains neutrons of energy higher than 2 MeV, but broadly centered around 15 MeV[105]. In a fusion spectrum, there are 1.4 neutrons with energy < 0.1 MeV per neutron source in a total of 4.3 neutrons per neutron source[8]. Hence, a fusion spectrum contains 32% more low-energy neutrons than those observed in a d-Be spectrum. According to the damage production theory[52,128], it is possible to assume that a fusion spectrum may create simpler defect configurations than do d-Be neutrons.

Results on stage-I recovery of Cu[104] showed that the damage structure produced by the d-Be spectrum is similar to the damage structure created by fast-neutrons. Therefore, fusion neutrons are expected to produce a simpler defect-state than the one observed in fast-neutron irradiations. This means that, by referring to Fig. 8.1, a stage-I recovery scheme for fusion neutrons will probably lie between the recovery schemes due to electron and fast-neutron bombardments. An estimate for stage-I percent recovery due to a fusion-neutron irradiation can be estimated as follows: The difference between the percent recovery due to electron and fast-neutron irradiations is to be multiplied by 32% (the extra low-energy neutrons observed in fusion spectra over d-Be spectra). The resulting percentage is added to the fast neutron percent recovery. This procedure yields values of 54%, 58% and 52% as anticipated stage-I recovery due to a hypothetical fusion-neutron irradiation of Fe, Zr and Cu respectively. Such inferred values compare favourably with the 60 to 65% recovery observed in stage I due to 16 MeV proton irradiation of the same metals.

CHAPTER 9

CONCLUSIONS

The theoretical and experimental results and the data analysis presented in this thesis lead to the following conclusions:

1. Damage-energy data for protons are higher by a factor of two when compared with the corresponding data for monoenergetic 14 MeV or 15 MeV neutrons.
2. 16 MeV protons approximate the damage induced in metals due to fusion reactor spectra.
3. The present data indicate that the vacancy-recombination model is a good approximation to estimate the number of displaced atoms in proton irradiation.
4. The damage state induced by protons in metals is similar to a combination of the damage states due to electrons and fast-neutrons. However, the generation of V-I pairs spontaneously with defect-clusters causes a fraction of those V-I pairs to recombine during irradiation.
5. The state of the sample imperfection influences the damage state induced by proton irradiation.

APPENDIX

ACCURACY OF THE ANALYTICAL RESULTS OF CHAPTER 4

It is essential to point out that the model of Grimes et al.[30], which has been used to calculate the non-elastic differential cross-sections in Chapter 4, accounts for all proton or neutron induced non-elastic events that emit a proton or a neutron. That is, for neutrons it accounts for (n,n'), (n,p) and the first neutron from (n,2n) reactions. Consequently, the error in the calculations presented in Chapter 4 is due to the emission of a second particle or the emission of a heavier particle such as in the case of (n,α) reaction. Such effects are insignificant as can be seen from Table A-1 and Fig. 4.13. In Table A-1, a comparison is shown between the present results for neutron interactions and the results of other researchers who either have directly employed the ENDF/B[9,122] or who have developed an analytical expression based on the ENDF/B contents[32,129]. All of these researchers, except REf. 9, have included every interaction which may contribute to the value of the non-elastic cross-section. Also, a graphical comparison between published 14-15 MeV neutron data and the present results is displayed in Fig. 4.13. The agreement in Table A-1 and Fig. 4.13 is within 1% to 5% depending on the target material.

Table A-1: A comparison between published 14-15 MeV neutron damage-energy data and the present results

Element	Damage energy eV-cm^2 ($\times 10^{20}$)				
Fe	-	-	-	-	27.85
Ni	-	-	-	-	25.42
Cu	25.2	27.2	30.1	26.6	26.75
Zr	-	-	-	-	20.04
Nb	24.7	27.4	26.2	25.8	26.60
Au	18.2	19.4	21.2	-	18.82
Ref.	9	122	129	32	Present
E_0,MeV	14.0	14.0	15.0	14.0	14-14.5

REFERENCES

1) F. L. Vook, H.K. Birnbaum, T.H. Blewitt, W.L. Brown, J.W. Corbett, J.H. Crawford, Jr., A.N. Goland, G.L. Kulcinski, M.T. Robinson, D.N. Seidman, F.W. Young, Jr., J. Bardeen, R.W. Balluffi, J.S. Koehler and G.H. Vineyard, "Report to the American Physical Society by the Study Group on Physics Problems Relating to Energy Technologies: Radiation Effects on Materials", Rev. Modern Phys. 47, Suppl. 3, Winter (1975).

2) "Fusion Reactor Design Problems", IAEA, Vienna, Nucl. Fusion, Special Suppl. (1974).

3) "Radiation Effects and Tritium Technology for Fusion Reactors", Proc. Int. Conf., Gatlinburg, U.S. ERDA, CONF-750989, (1975).

4) "Surface Effects in Controlled Fusion Devices", Int. Conf., San Francisco, J. Nucl. Mater. 63 (1976).

5) A.P. Fraas, Nucl. Technol. 22 (1974) 10.

6) G.L. Kulcinski, in Ref. 2, pp. 479-491.

7) G.M. McCracken, in Ref. 2, pp. 471-478.

8) C.M. Logan, J.D. Anderson and Z.A. Munir, Nucl. Technol. 22 (1974) 36.

9) M.T. Robinson, Proc. Brit. Nucl. Energy Soc. Conf. Nucl. Fusion Reactors, Abingdon, p. 364 (1970).

10) J.L. Brimhall, L.A. Charlot and H.E. Kissinger, Radiat. Eff. 28 (1976) 115.

11) A.D. Marwick, J. Nucl. Mater. 55 (1975) 259.

12) R.S. Nelson, D.J. Mazey and J.A. Hudson, J. Nucl. Mater. 37 (1970) 1.

13) J.R. Beeler, Jr., "The Role of Computer Experiments in Materials Research", Adv. Mater. Res. 4 (1974) 295.

14) C. Erginsoy, G.H. Vineyard and E. Englert, Phys. Rev. 133 (1964) A595.

15) C.M. Logan, Lawrence Livermore Lab., Report No. UCRL-51224 (1972).

16) C.M. Logan, J.D. Anderson and A.K. Mukherjee, J. Nucl. Mater. 48 (1973) 223.

17) J.B. Mitchell, C.M. Logan and C.J. Echer, J. Nucl. Mater. 48 (1973) 139.

18) C.M. Logan, J.D. Anderson and L.F. Hansen, J. Vac. Sci. Technol. 12 (1975) 536.

19) J.E. Robinson and D.A. Thompson, Phys. Rev. Letters 33 (1974) 1569.

20) R.W. Ollerhead, F.M. Mann, D.W. Kneff, Z.E. Switkowski and T.A. Tombrello, Phys. Rev. Letters 36 (1976) 439.

21) J.P. Biersack, E. Santner, R. Neubert and J. Ney, J. Nucl. Mater. 63 (1976) 443.

22) D.A. Thompson, J.E. Robinson, R.S. Walker, A.M. Omar and A.B. Campbell, in Ref. 3, Vol. 1, pp. 382-394.

23) M.W. Thompson, "Defects and Radiation Damage in Metals", Cambridge Univ. Press, Chapter 4 (1969).

24) See for example; I. Kaplan, "Nuclear Physics", Addison-Wesley, p. 565 (1964).

25) M. D. Goldberg, V. M. May and J. R. Stern, "Angular Distribution in Neutron Induced Reactions", BNL-400, Brookhaven National Lab. (1962).

26) See for example; R. D. Evans, "The Atomic Nucleus", McGraw-Hill, Chapter 22 (1967).

27) F. Vosniakos, Physics Cyclotron Lab., Manitoba University, private communication, 1977.

28) ENDF/B (Evaluated Nuclear Data File), Brookhaven National Laboratory, Upton, New York.

29) S. Pearlstein, "Starter Evaluated Charged Particle Data Library", Brookhaven National Lab., private communication, 1975.

30) S. M. Grimes, J. D. Anderson, B. A. Pohl, J. W. McClure and C. Wong, Phys. Rev. C4 (1971) 607.

31) C. Y. Fu and F. G. Perey, J. Nucl. Mater. 61 (1976) 153.

32) J. B. Roberto and M. T. Robinson, J. Nucl. Mater. 61 (1976) 149.

33) S. M. Grimes, Livermore Lab., private communication (1976).

34) A. B. Anufrienko, B. V. Devkin, G. V. kotel'nikova, Yu S. Kulabukhov, G. N. Lovchikova, O. A. Sal'nikov, I. A. Timokhin, V. R. Trubnikov and N. I. Fetisov, J. Nucl. Phys. (U.S.S.R.) 2 (1965) 826.

35) H. Wollenberger, in "Vacancies and Interstitials in Metals" North-Holland, Edited by A. Seeger et al. (1970).

36) A. Seeger, in "Radiation Damage in Solids", IAEA, Vienna, p. 101 (1962).

37) M. T. Robinson, D. K. Holmes and P.S. Oen, Bull. Am. Phys. Soc. 7 (1962) 171.

38) M. T. Robinson and O. S. Oen, Appl. Phys. Letters 2 (1963) 30.

39) O. S. Oen and M. T. Robinson, Appl. Phys. Letters 2 (1963) 83.

40) J. R. Beeler, Jr. and M. F. Beeler, U.S. ERDA, CONF-751006 (1975).

41) M. W. Thompson, Ref. 23, Chapter 7.

42) F. Seitz and J. Koehler, Solid State Phys. 2 (1956) 305.

43) J. A. Brinkman, J. Appl. Phys. 25 (1954) 961.

44) J. B. Gibson, A. N. Goland, M. Milgram and G. H. Vineyard, Phys. Rev. 120 (1960) 1229.

45) G. H. Vineyard, Radiat. Eff. 29 (1976) 245.

46) See for example; P. Sigmund, in "Radiation Damage Processes in Materials", Edited by C.H.S. Dupuy, pp. 3-118 (1975).

47) G. J. Dienes and G. H. Vineyard, "Radiation Effects in Solids". Interscience, p. 8 (1957).

48) J. Lindhard, V. Nielsen, M. Scharff and P.V. Thomsen, Mat. Fys. Medd. Dan. Vid. Selsk. 33 (1963) No. 10.

49) G. H. Kinchin and R. S. Pease, Rep. Prog. Phys. 18 (1955) 1.

50) P. Sigmund, Appl. Phys. Letters 14 (1969) 114.

51) M. T. Robinson and I. M. Torrens, Phys. Rev. B9 (1974) 5024.

52) M. T. Robinson, U.S. ERDA, CONF-751006 (1975).

53) J. R. Beeler, Jr., Phys. REv. 150 (1966) 470.

54) M. J. Norgett, M. T. Robinson and I. M. Torrens, Nucl. Eng. and Des. 33 (1975) 50.

55) E. W. Etherington, J. I. Bramman, R. S. Nelson and M. J. Norgett, Nucl. Eng. and Des. 33 (1975) 82.

56) R. S. Nelson, in Ref. 46, pp. 477-502.

57) R. C. Birtcher and T. H. Blewitt, in Proc. Int. Conf. "Properties of Atomic Defects in Metals", Argonne National Lab. (1976), to be published.

58) D. Dautreppe, in "Studies in Radiation Effects in Solids", Edited by G. J. Dienes, Gordon and Breach, Vol. 3, p. 153 (1969).

59) V. Hivert, R. Pichon, H. Bilger, P. Bichon, J. Verdone, D. Dautreppe and P. Moser, J. Phys. Chem. Solids 31 (1970) 1843.

60) K. Chountas, K. Papathanassopoulos, P. Andronikos and N. Kontoleon, Radiat. Eff. 24 (1975) 13.

61) P. Moser and D. Dautreppe, in "Radiation Damage in Solids", IAEA, Vienna, Vol. 1, pp. 209-307 (1962).

62) G. T. Meaden, "Electrical Resistance of Metals", Plenum Press, 1965.

63) J. Bass, "Deviation from Matthiessen's Rule", Adv. in Phys. 21 (1972) 431.

64) T. Broom, "Lattice Defects and the Electrical Resistivity of Metals", Adv. Phys. 3 (1954) 26.

65) A. C. Damask and G. J. Dienes, "Point Defects in Metals" [illegible]

66) M. Asdente and J. Friedel, J. Phys. Chem. Solids 11 (1959) 115.

67) P. G. Lucasson and R. M. Walker, Phys. Rev. 127 (1962) 485.

68) A. C. Damask and G. J. Dienes, Ref. 65, p. 146.

69) R. A. Johnson, Phys. Rev. 134 (1964) A1329.

70) B. T. Kelly, "Irradiation Damage in Solids", Pergamon Press (1966) pp 180-182; also A. C. Damask and G. J. Dienes, Ref. 65, pp. 145-143.

71) See for example; "Vacancies and Interstitials in Metals" Edited by A. Seeger et al., North-Holland (1970).

72) P. G. Shewmon, "Transformation in Metals", McGraw-Hill, p. 301 (1969).

73) I. V. Altovskii, Radiat. Eff. 17 (1973) 275.

74) R. Sizmann and U. Däunrt, in "Radiation Damage in Solids", IAEA, Vienna, Vol. 1, p 351 (1962).

75) S. I. Maydet and K. C. Russell, J. Nucl. Mater. 64 (1977) 101.

76) A. M. Omar, J. E. Robinson and D. A. Thompson, J. Nucl. Mater. 64 (1977) 121.

77) J. Benveniste, A. C. Mitchell and C. B. Fulmer, Phys. Rev. 133 (1964) B317.

78) I. E. Dayton and G. Schrank, Phys. Rev. 101 (1956) 1358.

79) N. M. Hintz, Phys. Rev. 106 (1957) 1201.

80) J. K. Dickens, E. Eichler and G. R. Satchler, Phys. Rev. 168 (1968) 1355.

81) G. W. Greenless, L. G. Kuo and M. Petravic, Proc. Roy. Soc. A242 (1957) 206.

82) W. Makofske, G. W. Greenless, H. S. Liers and G. J. Pyle, Phys. Rev. C5 (1972) 780.

83) D. Wilmore and P. E. Hodgson, Nucl. Phys. 55 (1964) 673.

84) F. G. Perey, Phys. Rev. 131 (1963) 745.

85) R. W. Bauer, J. D. Anderson and L. J. Christensen, Nucl. Phys. 48 (1963) 152.

86) A. E. Glassgold, W. B. Cheston, M. L. Stein, S. B. Schuldt and G. W. Erickson, Phys. REv. 106 (1957) 1207.

87) F. G. Perey and B. Buck, Nucl. Phys. 32 (1962) 353.

88) R. L. Clarke and W. G. Cross, Nucl. Phys. A95 (1967) 320.

89) R. G. Clarkson and W. R. Coker, Phys. Rev. C2 (1970) 1108.

90) G. C. Wick, Phys. Rev. 75 (1949) 1459.

91) BNL-325, Vols. II-B and II-E (1962).

92) D. D. Phillips, R. W. Davis and E. R. Graves, Phys. Rev. 88 (1952) 600.

93) R. D. Albert and L. F. Hansen, Phys. Rev. 123 (1961) 1749.

94) Inferred values based on information given in Refs. 33 and 34.

95) J. M. Wells and K. C. Russell, Radiat. Eff. 37 (1976) 157.

96) R. R. Coltman, Jr., Oak Ridge National Laboratory, private communication, 1977.

97) P. Lucasson, A. Lucasson and G. Lelogeals, Cryogenics 6 (1966) 169.

98) P. P. Pronko, W. R. Hardy and J. Shewchun, Radiat. Eff. 10 (1971) 79,

99) J. Bøttinger, J. A. Davis, J. Lori and J. L. Whitton, Nucl. Instr. and Methods 109 (1973) 579.

100) Handbook of Chemistry and Physics, CRC Press, 56th Edition, 1976.

101) M. Shimotomai, A. M. Omar and J. E. Robinson, Cryogenics 17 (1977) 47.

102) M. G. Miller, B. W. Koehn and R. L. Chaplin, Radiat. Eff. 30 (1978) 73.

103) L. L. Sparks and R. L. Powell, J. Res. of NBS 76A (1972) 263.

104) J. B. Roberto, C. E. Klabunde, J. M. Williams and R. R. Coltman, Jr., J. Nucl. Mater., to be published.

105) J. B. Roberto, C. E. Klabunde, J. M. Williams, R. R. Coltman, Jr., M. J. Saltmarsh and C. B. Fulmer, Appl. Phys. Letters 30 (1977) 509.

106) C. Minier-Cassayre, Report No. ORNL-tr-668 (1965).

107) R. S. Averback and K. L. Merkle, Phys. Rev. B16 (1977) 3860.

108) M. Nakagawa, K. Böing, P. Rosner and G. Vogl, Phys. Letters 56A (1976) 481.

109) H. H. Neely, Radiat. Eff. 3 (1970) 189.

110) M. Rosenbaum, E. A. Bisogni and T. H. Blewitt, J. Nucl. Mater. 48 (1973) 201.

111) P. Vialaret, F. Moreau, A. Bessis, C. Dimitrov and O. Dimitrov, J. Nucl. Mater. 55 (1975) 83.

112) M. Biget, R. Rizk and P. Vajda, Solid State Comm. 16 (1975) 949.

113) G. R. Piercy, J. Nucl. Mater. 29 (1969) 267.

114) H. H. Neely and D. W. Keefer, Phys. Stat. Sol. 24 (1967) 217.

115) A. Sato and M. Meshii, Phys. Stat. Sol. A22 (1974) 253.

116) J. A. Horak and T. H. Blewitt, Nucl. Technol. 27 (1975) 416.

117) S. Takamura, H. Maeta and S. Okuda, J. Phys. Soc. Japan 26 (1969) 1125.

118) C. Minier-Cassayre and M. D. Dautreppe, Académie des Sciences, 256 (1963) 2368.

119) M. Biget, F. Maury, P. Vajda, A. Lucasson and P. Lucasson, Radiat. Eff. 7 (1971) 223.

120) J. B. Roberto, J. Narayan and M. J. Saltmarch, in Ref. 3, Vol. II, p. 159 (1975).

121) R. R. Coltman, C. E. Klabunde and J. K. Redman, Phys. Rev. 156 (1967) 715.

122) D. M. Parkin and A. N. Goland, Radiat. Eff. 28 (1976) 31.

123) R. L. Lyles and K. L. Merkle, in Ref. 3, Vol. I, p. 191 (1975).

124) J. C. H. Spence, "Single Atom Contrast", in Developments in Electron Microscopy and Analysis, Edited by J. A. Venables, Academic Press (1976).

125) F. Dworschak, K. Herschbach and J. S. Koehler, Phys. Rev. 133 (1964) A293.

126) J. W. Corbett, R. B. Smith and R. M. Walker, Phys. Rev. 114 (1959) 1452; Phys. Rev. 114 (1959) 1460.

127) J. A. Horak and T. H. Blewitt, Phys. Stat. Sol. (a) 9 (1972) 721.

128) J. R. Beeler, Jr., M. F. Beeler and C. V. Parks, in Ref. 3, Vol. I, p. 362 (1975).

129) J. B. Roberto, M. T. Robinson and C. Y. Fu, Int. Conf. Surface Effects Controlled Fusion Devices, San Francisco (1975).